BOOSTING RAY SEARCH PROCEDURE OF HARD-LABEL ATTACKS WITH TRANSFER-BASED PRIORS

Chen Ma [1,2] **Xinjie Xu** [1] **Shuyu Cheng** [3] **Qi Xuan** [1,2]
[1] Institute of Cyberspace Security, Zhejiang University of Technology, Hangzhou 310023, China
[2] Binjiang Institute of Artificial Intelligence, ZJUT, Hangzhou 310056, China
[3] JQ Investments, Shanghai 200122, China
{machen,xuanqi}@zjut.edu.cn, xxj1018@foxmail.com, csy530216@126.com

ABSTRACT

One of the most practical and challenging types of black-box adversarial attacks is the hard-label attack, where only the top-1 predicted label is available. One effective approach is to search for the optimal ray direction from the benign image that minimizes the ℓ_p norm distance to the adversarial region. The unique advantage of this approach is that it transforms the hard-label attack into a continuous optimization problem. The objective function value is the ray's radius, which can be obtained via binary search at a high query cost. Existing methods use a "sign trick" in gradient estimation to reduce the number of queries. In this paper, we theoretically analyze the quality of this gradient estimation and propose a novel prior-guided approach to improve ray search efficiency both theoretically and empirically. Specifically, we utilize the transfer-based priors from surrogate models, and our gradient estimators appropriately integrate them by approximating the projection of the true gradient onto the subspace spanned by these priors and random directions, in a query-efficient manner. We theoretically derive the expected cosine similarities between the obtained gradient estimators and the true gradient, and demonstrate the improvement achieved by incorporating priors. Extensive experiments on the ImageNet and CIFAR-10 datasets show that our approach significantly outperforms 11 state-of-the-art methods in terms of query efficiency.

1 INTRODUCTION

Adversarial attacks represent a major security threat to deep neural networks (DNNs), where subtle, imperceptible perturbations are crafted to cause misclassifications. To assess DNN robustness and uncover vulnerabilities, the research community has developed various adversarial attack strategies. As a result, adversarial attacks and defenses have become a focal point in AI security research.

Based on the available information about the target model, adversarial attacks can be broadly classified into white-box and black-box attacks. White-box attacks, such as those proposed by Madry et al. (2018); Moosavi-Dezfooli et al. (2016), rely on the target model's gradients with respect to the input, making them less practical in real-world applications. Black-box attacks, by contrast, are often more feasible, as they do not require knowledge of model parameters or gradients. As a subset of black-box attacks, transfer-based attacks generate adversarial examples using white-box models with the aim of generalizing to other models. While transfer-based attacks do not involve querying the target model, their success rate is inconsistent. Alternatively, query-based black-box attacks iteratively interact with the target model to achieve higher success rates. These attacks can be categorized into two subtypes: score-based and decision-based (also known as hard-label) attacks. Score-based attacks (Ma et al., 2021a) utilize the model's output logits to guide the attack, whereas hard-label attacks rely solely on top-1 predicted labels, making them particularly practical when only label information is accessible. In this work, we focus on the problem of reducing query complexity in hard-label attacks.

The difficulty of hard-label attacks is that the labels can only be flipped near the classification decision boundary, and thus the objective function is discontinuous. As a result, the attack requires solving a high-dimensional combinatorial optimization problem, which is challenging. Common approaches (Chen et al., 2020; Brendel et al., 2018) start with a sample containing large adversarial perturbations

and iteratively reduce the distortion by moving along the decision boundary towards a benign image. However, these methods lack convergence guarantees. To reformulate the problem as a continuous optimization task, ray-search methods have been introduced. Typical approaches such as OPT (Cheng et al., 2019), Sign-OPT (Cheng et al., 2020), and RayS (Chen & Gu, 2020) aim to minimize an objective function $g(\theta)$, which is defined as the shortest ℓ_p norm distance along the ray direction θ from the benign image to the adversarial region. This function value can be evaluated using a binary search method. Leveraging the smooth and continuous nature of decision boundaries, $g(\theta)$ is locally continuous, making it amenable to zeroth-order (ZO) optimization with a gradient estimator. OPT employs a random gradient-free (RGF) estimator, but it incurs high query cost due to the binary search in finite differences. Sign-OPT reduces the query complexity by using the sign of the directional derivative in gradient estimation, but it significantly sacrifices gradient accuracy.

To solve this problem and improve query efficiency, we employ the same objective function $g(\theta)$ and propose incorporating the transfer-based priors into gradient estimation. An ideal prior is the gradient of $g(\theta)$ from a surrogate model, but it cannot be easily obtained since $g(\theta)$ is non-differentiable due to the binary search. Instead, we propose a surrogate loss, whose gradient is proportional to that of $g(\theta)$, to obtain the prior. Once the transfer-based priors are obtained, we must design better gradient estimators that effectively integrate these priors. This is particularly challenging under the hard-label restriction, as accurately determining the value of $g(\theta)$ is costly. As a result, previous prior-guided methods for score-based attacks such as PRGF (Cheng et al., 2021; Dong et al., 2022) are not suitable in this context. Thus, we need to explore how to improve the gradient estimator with additional priors while minimizing queries. To achieve this, we propose two algorithms: Prior-Sign-OPT and Prior-OPT. They estimate the gradient in a query-efficient manner by approximating the projection of the true gradient onto a subspace spanned by priors and randomly sampled vectors. We provide a thorough theoretical analysis to validate their effectiveness and offer theoretical comparisons between Sign-OPT and our approach. In particular, Prior-OPT achieves a better approximation of the subspace projection with only slightly more queries, and can adaptively adjust the weight of each prior based on its quality, striking a balance between gradient accuracy and query efficiency. While several methods (Brunner et al., 2019; Shi et al., 2023) attempt to combine transfer- and decision-based attacks, they lack theoretical guarantees and often perform poorly. Crucially, in the hard-label setting, these approaches fail to effectively address the challenge of appropriately weighing the prior when it deviates significantly from the true gradient. Our approach resolves this issue and naturally scales to priors from multiple surrogate models, demonstrating further improvement in attack performance.

To summarize, our main contributions are as follows.

1. **Novelty in hard-label attacks.** We address the problem of introducing the transfer-based priors into hard-label attacks by employing the subspace projection approximation, which significantly improves the accuracy of gradient estimation with slightly more queries. Our approach not only strikes a balance between gradient estimation and query efficiency, but also elegantly integrates priors from multiple surrogate models to further improve performance.
2. **Novelty in theoretical analysis.** We analyze the quality of our gradient estimators and that of the orthogonal variant of Sign-OPT, enabling theoretical comparisons. To our knowledge, this is the first work to derive the expected cosine similarities between estimators of the Sign-OPT family and the true gradient, theoretically guaranteeing performance improvement.
3. **Extensive experiments.** Extensive experiments conducted on the ImageNet and CIFAR-10 datasets show that our approach outperforms 11 state-of-the-art methods significantly.

2 Related Work

Hard-label attacks can be categorized into boundary-search and ray-search approaches.

The boundary-search approaches start from a large perturbation or an image of the target class and then reduce distortions by iteratively moving along the decision boundary towards the original image. Boundary Attack (BA) (Brendel et al., 2018) is an early representative method, and its query efficiency is relatively low. HopSkipJumpAttack (HSJA) (Chen et al., 2020) estimates the gradient at the decision boundary to update the sample and then finds the next boundary point by moving it towards the benign image. Tangent Attack (TA) and Generalized Tangent Attack (G-TA) (Ma et al., 2021b) find an optimal tangent point on a virtual hemisphere or semi-ellipsoid to efficiently generate

the adversarial example. CGBA (Reza et al., 2023) conducts a boundary search along a semicircular path on a restricted 2D plane to find the boundary point. To avoid gradient estimation, SurFree (Maho et al., 2021) and Triangle Attack (Wang et al., 2022) find the adversarial example in a DCT subspace to improve query efficiency. Evolutionary (Dong et al., 2019) adopts the (1+1)-CMA-ES, a simple yet effective variant of Covariance Matrix Adaptation Evolution Strategy, to efficiently generate adversarial examples. Adaptive History-driven Attack (AHA) (Li et al., 2021) gathers data of previous queries as the prior for current sampling, which improves the random walk optimization.

The ray-search approaches aim to find an optimal direction θ that reaches the nearest adversarial region. As mentioned in Section 1, it is challenging to address both the high query complexity issue of OPT and the low estimation accuracy issue of Sign-OPT. RayS (Chen & Gu, 2020) avoids gradient estimation and employs a hierarchical search step to efficiently find the optimal direction. However, RayS only supports untargeted ℓ_∞-norm attacks. Since the query efficiency of previous ray-search approaches has not surpassed that of boundary-search methods, they have attracted less research interest and remain insufficiently studied. We note that the mechanisms of OPT and Sign-OPT remain poorly understood, and their inefficiency stems from the limited precision in gradient estimation.

Several methods attempt to combine transfer- and decision-based attacks, but the critical issue, namely how to weigh the prior when it deviates significantly from the true gradient, has not been well addressed. For example, Biased Boundary Attack (BBA) (Brunner et al., 2019), Customized Iteration and Sampling Attack (CISA) (Shi et al., 2023) and Small-Query Black-Box Attack (SQBA) (Park et al., 2024) set the prior's coefficient empirically rather than through theoretical analysis. In contrast, our approach dynamically calculates optimal coefficients, improving gradient estimation accuracy.

3 The Proposed Approach

3.1 The Goal of Hard-label Attacks

Given a k-class classifier $f : \mathbb{R}^d \to \mathbb{R}^k$ and a benign image $\mathbf{x} \in [0,1]^d$ which is correctly classified by f, the adversary aims to find an adversarial example $\mathbf{x}_{\text{adv}}$ with the minimum perturbation such that $f(\mathbf{x}_{\text{adv}})$ outputs an incorrect prediction. Formally, we formulate the attack goal as:

$$\min_{\mathbf{x}_{\text{adv}}} d(\mathbf{x}_{\text{adv}}, \mathbf{x}) \quad \text{s.t.} \quad \Phi(\mathbf{x}_{\text{adv}}) = 1, \tag{1}$$

where $d(\mathbf{x}_{\text{adv}}, \mathbf{x}) \coloneqq \|\mathbf{x}_{\text{adv}} - \mathbf{x}\|_p$ is the ℓ_p norm distortion, and $\Phi(\cdot)$ is a success indicator function:

$$\Phi(\mathbf{x}_{\text{adv}}) \coloneqq \begin{cases} 1 & \text{if } \hat{y} = y_{\text{adv}} \text{ in the targeted attack,} \\ & \quad \text{or } \hat{y} \neq y \text{ in the untargeted attack,} \\ 0 & \text{otherwise,} \end{cases} \tag{2}$$

where $\hat{y} = \arg\max_{i \in \{1,\ldots,k\}} f(\mathbf{x}_{\text{adv}})_i$ is the top-1 predicted label of f, $y \in \mathbb{R}$ is the true label of $\mathbf{x}$, and $y_{\text{adv}} \in \mathbb{R}$ is a target class label. In this study, we follow Cheng et al. (2019; 2020) to reformulate the problem (1) as the problem of finding the ray direction of the shortest distance from $\mathbf{x}$ to the adversarial region:

$$\min_{\theta \in \mathbb{R}^d \setminus \{\mathbf{0}\}} g(\theta) \quad \text{where} \quad g(\theta) \coloneqq \inf\Big\{\lambda : \lambda > 0, \Phi\big(\mathbf{x} + \lambda \frac{\theta}{\|\theta\|}\big) = 1\Big\}. \tag{3}$$

Note that $g(\theta) = +\infty$ when the set is empty, since $\inf \emptyset = +\infty$ by convention. Finally, the adversarial example is $\mathbf{x}^* = \mathbf{x} + g(\theta^*)\frac{\theta^*}{\|\theta^*\|}$, and θ^* is the optimal solution of problem (3).

3.2 The Optimization of Searching Ray Directions

The previous works (Cheng et al., 2019; 2020) attempt to optimize the problem (3) by using ZO methods. However, the restriction of hard-label access results in a high query cost of the gradient estimation, because obtaining a single value of $g(\theta)$ requires performing a binary search with multiple queries, and the gradient estimation with finite difference requires multiple computations of $g(\theta)$. Sign-OPT (Cheng et al., 2020) replaces the finite-difference term $g(\theta + \sigma\mathbf{u}) - g(\theta)$ with $\text{sign}(g(\theta + \sigma\mathbf{u}) - g(\theta))$, which improves query efficiency by only using a single query (Eq. (8)). However, it significantly reduces the accuracy of the gradient estimation. We propose to incorporate transfer-based priors to enhance accuracy without significantly increasing query complexity, thus achieving an optimal balance between query complexity and estimation accuracy.

The first challenge is how to obtain a transfer-based prior $\nabla g_{\hat{f}}(\theta)$ from a surrogate model $\hat{f}$, where $g_{\hat{f}}(\theta)$ represents the shortest distance along the direction θ to the adversarial region of $\hat{f}$. This is challenging because $g_{\hat{f}}(\theta)$ is typically evaluated using binary search, making it non-differentiable. To address this, for any non-zero vector $\theta_0 \in \mathbb{R}^d$ such that $g_{\hat{f}}(\theta_0) < +\infty$, we define a surrogate function $h(\theta, \lambda)$ such that $\nabla g_{\hat{f}}(\theta_0) = c \cdot \nabla_\theta h(\theta_0, \lambda_0)$, where $\lambda_0 = g_{\hat{f}}(\theta_0)$ is treated as a constant during differentiation. Here, λ is a scalar, and c is a non-zero constant. The surrogate function $h(\theta, \lambda)$ is defined as the negative Carlini & Wagner (C&W) loss function of $\hat{f}$:

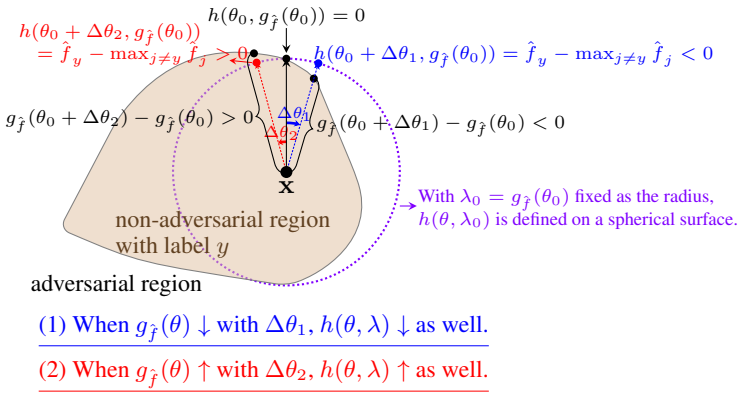

Figure 1: Geometrical explanation of $\nabla g_{\hat{f}}(\theta_0) \propto \nabla_\theta h(\theta_0, \lambda_0)$ by taking an untargeted attack as an example. When $g_{\hat{f}}(\theta)$ reduces/increases with a small $\Delta\theta$, $h(\theta, \lambda)$ changes at a similar rate. The formal proof is in Appendix A.

$$h(\theta, \lambda) := \begin{cases} \hat{f}_y - \max_{j \neq y} \hat{f}_j, & \text{if untargeted attack,} \\ \max_{j \neq \hat{y}_{\text{adv}}} \hat{f}_j - \hat{f}_{\hat{y}_{\text{adv}}}, & \text{if targeted attack,} \end{cases} \tag{4}$$

where $\hat{f}_i := \hat{f}\big(\mathbf{x} + \lambda \cdot \frac{\theta}{\|\theta\|}\big)_i$ is an abbreviation for the i-th element of the output of $\hat{f}$, and $\mathbf{x}$ is the original image. Any non-zero scalar can be used as λ, but the specific value $\lambda_0 = g_{\hat{f}}(\theta_0)$ yields a gradient proportional to $\nabla g_{\hat{f}}(\theta_0)$. The value λ_0 is obtained through binary search, where $h(\theta_0, \lambda_0)$ represents the negative C&W loss at the decision boundary of the surrogate model $\hat{f}$. The geometric explanation and formal proof of $\nabla g_{\hat{f}}(\theta_0) = c \cdot \nabla_\theta h(\theta_0, \lambda_0)$ are presented in Fig. 1 and Appendix A.

In targeted attacks, determining an appropriate λ_0 value becomes a challenging task. This is because the spatial distribution of classification regions, along with the shape and extent of the decision boundaries, varies across different models. Although we can locate the region corresponding to the predefined target class y_{adv} along the θ direction in the target model f, the same direction may not lead to the region of the class y_{adv} in a surrogate model $\hat{f}$. Therefore, we must set a new target class $\hat{y}_{\text{adv}}$ before determining λ_0 and computing Eq. (4). See Appendix B for detailed steps.

Given s non-zero vectors $\mathbf{k}_1, \ldots, \mathbf{k}_s$ representing transfer-based priors from s surrogate models and $q - s$ randomly sampled vectors $\mathbf{r}_i \sim \mathcal{N}(\mathbf{0}, \mathbf{I})$ for $i = 1, \ldots, q - s$, our objective is to estimate a gradient $\mathbf{v}^* \approx \nabla g(\theta)$ as accurately as possible using these q vectors. In *the score-based attack setting*, there is a subspace projection estimator theory (Meier et al., 2019; Cheng et al., 2021) that can solve this problem. Based on this theory, the optimal estimated gradient $\mathbf{v}^*$ that maximizes its similarity with the true gradient is given by Proposition 3.1 in the score-based setting[1].

Proposition 3.1. *(Optimality of the subspace projection estimator) Let $\mathbf{k}_1, \ldots, \mathbf{k}_s$ and $\mathbf{r}_1, \ldots, \mathbf{r}_{q-s}$ be defined above; let $S := \operatorname{span}\{\mathbf{k}_1, \ldots, \mathbf{k}_s, \mathbf{r}_1, \ldots, \mathbf{r}_{q-s}\}$ denote the subspace spanned by these vectors. Then the optimal $\mathbf{v}^*$ in S that maximizes $\overline{\nabla g(\theta)}^\top \mathbf{v}$ subject to $\|\mathbf{v}\| = 1$ is the ℓ_2-normalized projection of $\nabla g(\theta)$ onto S, denoted as $\mathbf{v}^* := \overline{\nabla g(\theta)_S}$.*

According to Proposition 3.1, finding the optimal approximate gradient is equivalent to finding a projection of the true gradient onto a low-dimensional subspace S spanned by all available vectors. The projection of a vector onto a subspace S can be calculated by summing its projections onto the orthonormal basis of S. To achieve this, we construct an orthonormal basis of S via Gram-Schmidt orthonormalization, which transforms $\mathbf{k}_1, \ldots, \mathbf{k}_s, \mathbf{r}_1, \ldots, \mathbf{r}_{q-s}$ into an orthonormal basis $\mathbf{p}_1, \ldots, \mathbf{p}_s, \mathbf{u}_1, \ldots, \mathbf{u}_{q-s}$. Note that $\mathbf{p}_1, \ldots, \mathbf{p}_s$ correspond to $\mathbf{k}_1, \ldots, \mathbf{k}_s$, and $\mathbf{u}_1, \ldots, \mathbf{u}_{q-s}$ correspond to $\mathbf{r}_1, \ldots, \mathbf{r}_{q-s}$. Then, we can compute the projection of $\nabla g(\theta)$ onto S by Eq. (5):

$$\mathbf{v}^* = \sum_{i=1}^{s} \nabla g(\theta)^\top \mathbf{p}_i \cdot \mathbf{p}_i + \sum_{i=1}^{q-s} \nabla g(\theta)^\top \mathbf{u}_i \cdot \mathbf{u}_i. \tag{5}$$

[1]Throughout this paper, for any vector $\mathbf{x}$, we denote its ℓ_2-normalized version by $\overline{\mathbf{x}}$, where $\overline{\mathbf{x}} := \mathbf{x}/\|\mathbf{x}\|$.

Given the queried function values, $\nabla g(\theta)^\top \mathbf{u}$ for the unit ℓ_2-norm vector $\mathbf{u}$ can be approximated by the finite-difference method, without requiring backpropagation:

$$\nabla g(\theta)^\top \mathbf{u} \approx \frac{g(\theta + \sigma \mathbf{u}) - g(\theta)}{\sigma}, \tag{6}$$

where σ is a small positive number. By plugging Eq. (6) into Eq. (5), we can easily calculate $\mathbf{v}^*$ in the score-based setting as $\mathbf{v}^* = \sum_{i=1}^{s} \frac{g(\theta+\sigma\mathbf{p}_i)-g(\theta)}{\sigma} \cdot \mathbf{p}_i + \sum_{i=1}^{q-s} \frac{g(\theta+\sigma\mathbf{u}_i)-g(\theta)}{\sigma} \cdot \mathbf{u}_i$. However, in *the hard-label setting*, the finite-difference requires a large number of queries due to the binary search of $g(\cdot)$. We propose two algorithms to reduce query cost by computing the approximate projection, i.e., Prior-Sign-OPT and Prior-OPT. With s priors, Prior-Sign-OPT uses Eq. (7) to improve performance:

$$\mathbf{v}^* = \sum_{i=1}^{s} \text{sign}(g(\theta + \sigma \mathbf{p}_i) - g(\theta)) \cdot \mathbf{p}_i + \sum_{i=1}^{q-s} \text{sign}(g(\theta + \sigma \mathbf{u}_i) - g(\theta)) \cdot \mathbf{u}_i. \tag{7}$$

Eq. (7) is similar to the formula of Sign-OPT, benefiting from using only a single query to calculate the sign of the directional derivative (Cheng et al., 2020):

$$\text{sign}(g(\theta + \sigma \mathbf{u}_i) - g(\theta)) = \begin{cases} +1, & f\left(\mathbf{x} + g(\theta)\frac{\theta+\sigma\mathbf{u}_i}{\|\theta+\sigma\mathbf{u}_i\|}\right) = y, \\ -1, & \text{otherwise.} \end{cases} \tag{8}$$

The accuracy of the estimated gradient is crucial in optimization. A natural way to assess accuracy is via the following metrics: $\mathbb{E}[\gamma]$ and $\mathbb{E}[\gamma^2]$, where γ is the cosine similarity between the estimated and true gradients. We propose a novel approach to compute $\mathbb{E}[\gamma]$ and $\mathbb{E}[\gamma^2]$ for Sign-OPT, Prior-Sign-OPT, and Prior-OPT. Our baseline extends Sign-OPT (Cheng et al., 2020) by employing orthogonal random vectors, while retaining the original name to maintain consistency within the method family.

Theorem 3.2. *For the Sign-OPT estimator approximated by Eq.* (6) *(defined as Eq.* (44)*), we let* $\gamma := \overline{\mathbf{v}}^\top \overline{\nabla g(\theta)}$ *be its cosine similarity to the true gradient, where* $\overline{\mathbf{v}} := \frac{\mathbf{v}}{\|\mathbf{v}\|}$*, then*

$$\mathbb{E}[\gamma] = \sqrt{q}\frac{\Gamma(\frac{d}{2})}{\Gamma(\frac{d+1}{2})\sqrt{\pi}}, \tag{9}$$

$$\mathbb{E}[\gamma^2] = \frac{1}{d}\left(\frac{2}{\pi}(q-1)+1\right). \tag{10}$$

The proof of Theorem 3.2 is included in Appendix C.1. For Prior-Sign-OPT, we have Theorem 3.3.

Theorem 3.3. *For the Prior-Sign-OPT estimator approximated by Eq.* (6) *(defined as Eq.* (82)*), we let* $\gamma := \overline{\mathbf{v}^*}^\top \overline{\nabla g(\theta)}$ *be its cosine similarity to the true gradient, where* $\overline{\mathbf{v}^*} := \frac{\mathbf{v}^*}{\|\mathbf{v}^*\|}$*, then*

$$\mathbb{E}[\gamma] = \frac{1}{\sqrt{q}}\left[\sum_{i=1}^{s}|\alpha_i| + (q-s)\sqrt{1-\sum_{i=1}^{s}\alpha_i^2}\cdot\frac{\Gamma(\frac{d-s}{2})}{\Gamma(\frac{d-s+1}{2})\sqrt{\pi}}\right], \tag{11}$$

$$\begin{aligned}\mathbb{E}[\gamma^2] = \frac{1}{q}\Bigg[&\left(\sum_{i=1}^{s}|\alpha_i|\right)^2 + \frac{q-s}{d-s}\left(\frac{2}{\pi}(q-s-1)+1\right)\left(1-\sum_{i=1}^{s}\alpha_i^2\right) \\ &+ 2\left(\sum_{i=1}^{s}|\alpha_i|\right)(q-s)\sqrt{1-\sum_{i=1}^{s}\alpha_i^2}\cdot\frac{\Gamma(\frac{d-s}{2})}{\Gamma(\frac{d-s+1}{2})\sqrt{\pi}}\Bigg],\end{aligned} \tag{12}$$

where $\alpha_i := \mathbf{p}_i^\top \overline{\nabla g(\theta)}$ *is the cosine similarity between the* i*-th prior and the true gradient.*

The proof of Theorem 3.3 is presented in Appendix C.2. Now we can compare $\mathbb{E}[\gamma]$ of Sign-OPT (Eq. (9)) and Prior-Sign-OPT (Eq. (11)). In Sign-OPT, applying Jensen's inequality yields the bound $\mathbb{E}[\gamma] \leq \sqrt{\mathbb{E}[\gamma^2]} = \sqrt{(2(q-1)+\pi)/(\pi d)}$. When $q \ll d$, $\mathbb{E}[\gamma]$ becomes very small, resulting in poor performance. In contrast, Prior-Sign-OPT with a single prior can improve performance. For instance, when attacking an image of size $32 \times 32 \times 3$, and using parameters $q = 200$ and $s = 1$, if $0.01422 \leq |\alpha_1| \leq 0.611$, $\mathbb{E}[\gamma]$ of Prior-Sign-OPT surpasses that of Sign-OPT. However, Prior-Sign-OPT may underperform Sign-OPT in certain cases, such as when $|\alpha_1| \geq 0.612$ in the example above, because it applies sign-based multipliers to both random vectors and priors. Intuitively, random

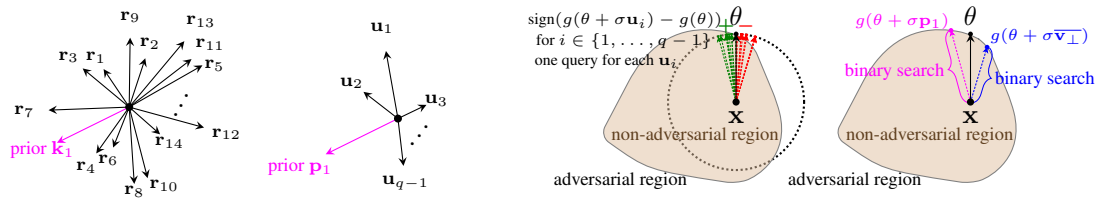

(a) Get prior $\mathbf{k}_1$ and sample $\mathbf{r}_i$. (b) Orthonormal basis. (c) Estimate a sign-based $\mathbf{v}_\perp$. (d) Estimate $\mathbf{v}^*$ with $\mathbf{v}_\perp$ and $\mathbf{p}_1$.

Figure 2: Simplified two-dimensional illustration of the gradient estimation of Prior-OPT with a single transfer-based prior. In Fig. 2a, we first sample random vectors $\mathbf{r}_i \sim \mathcal{N}(\mathbf{0}, \mathbf{I})$ for $i = 1, \ldots, q-1$ and obtain a transfer-based prior $\mathbf{k}_1$ using $\nabla_\theta h(\theta, \lambda)$, where $h(\theta, \lambda)$ is defined in Eq. (4). Then, as shown in Fig. 2b, we perform Gram-Schmidt orthonormalization on these vectors to obtain an orthonormal basis $\mathbf{p}_1, \mathbf{u}_1, \ldots, \mathbf{u}_{q-1}$, where $\mathbf{p}_1 = \mathbf{k}_1$. Next, we estimate $\mathbf{v}_\perp$ based on Eq. (14) with $\mathbf{u}_1, \ldots, \mathbf{u}_{q-1}$ (Fig. 2c), where each $\text{sign}(g(\theta+\sigma\mathbf{u}_i) - g(\theta))$ requires only a single query (Eq. (8)). Finally, as shown in Fig. 2d, we estimate a gradient $\mathbf{v}^*$ based on Eq. (13) with $\mathbf{p}_1$ and $\mathbf{v}_\perp$, where the values of $g(\theta+\sigma\mathbf{p}_1)$ and $g(\theta+\sigma\overline{\mathbf{v}_\perp})$ are obtained via the binary search with multiple queries.

vectors $\mathbf{u}_1, \ldots, \mathbf{u}_{q-s}$ have relatively consistent cosine similarities with the true gradient as they are identically distributed, allowing for efficient sign-based estimation. In contrast, the cosine similarities between the priors $\mathbf{p}_1, \ldots, \mathbf{p}_s$ and the true gradient differ, requiring more precise estimation. To address this, we propose Prior-OPT that treats priors and random vectors differently. Fig. 2 illustrates the process of gradient estimation in Prior-OPT, which is based on the following formula:

$$\mathbf{v}^* = \sum_{i=1}^{s} \frac{g(\theta+\sigma\mathbf{p}_i) - g(\theta)}{\sigma} \cdot \mathbf{p}_i + \frac{g(\theta+\sigma\overline{\mathbf{v}_\perp}) - g(\theta)}{\sigma} \cdot \overline{\mathbf{v}_\perp}, \tag{13}$$

where $\overline{\mathbf{v}_\perp}$ is the ℓ_2 normalization of $\mathbf{v}_\perp$, and $\mathbf{v}_\perp$ is obtained by:

$$\mathbf{v}_\perp \coloneqq \sum_{i=1}^{q-s} \text{sign}(g(\theta+\sigma\mathbf{u}_i) - g(\theta)) \cdot \mathbf{u}_i. \tag{14}$$

Since random vectors $\mathbf{u}_1, \ldots, \mathbf{u}_{q-s}$ poorly align with $\nabla g(\theta)$, we aggregate them into a single vector $\mathbf{v}_\perp$ using a less accurate estimator in Eq. (14), which is orthogonal to all priors. Compared with Eq. (7), Eq. (13) provides a more accurate projection approximation. We now present Theorem 3.4.

Theorem 3.4. *For the Prior-OPT estimator approximated by Eq.* (6) *(defined as Eq.* (114)*), we let* $\gamma \coloneqq \overline{\mathbf{v}^*}^\top \overline{\nabla g(\theta)}$ *be its cosine similarity to the true gradient, where* $\overline{\mathbf{v}^*} \coloneqq \frac{\mathbf{v}^*}{\|\mathbf{v}^*\|}$*, then*

$$\mathbb{E}[\gamma] \geq \sqrt{\sum_{i=1}^{s} \alpha_i^2 + \frac{(q-s)(1-\sum_{i=1}^{s}\alpha_i^2)}{\pi} \left(\frac{\Gamma(\frac{d-s}{2})}{\Gamma(\frac{d-s+1}{2})}\right)^2}, \tag{15}$$

$$\mathbb{E}[\gamma] \leq \sqrt{\sum_{i=1}^{s} \alpha_i^2 + \frac{1}{d-s}\left(\frac{2}{\pi}(q-s-1)+1\right)\left(1-\sum_{i=1}^{s}\alpha_i^2\right)}, \tag{16}$$

$$\mathbb{E}[\gamma^2] = \sum_{i=1}^{s} \alpha_i^2 + \frac{1}{d-s}\left(\frac{2}{\pi}(q-s-1)+1\right)\left(1-\sum_{i=1}^{s}\alpha_i^2\right), \tag{17}$$

where $\alpha_i \coloneqq \mathbf{p}_i^\top \overline{\nabla g(\theta)}$ *is the cosine similarity between the* i*-th prior and the true gradient.*

The proof of Theorem 3.4 is included in Appendix C.3. $\mathbb{E}[\gamma^2]$ is the second-order moment, which reflects the magnitude of γ in a statistical sense. Under certain assumptions, $\mathbb{E}[\gamma^2]$ directly affects the convergence rate of optimization algorithms (Cheng et al., 2021). Intuitively, a larger γ indicates more accurate gradient estimation, leading to faster optimization and improved query efficiency. Next, we compare $\mathbb{E}[\gamma^2]$ for Prior-OPT (Eq. (17)) and Sign-OPT (Eq. (10)). Under the reasonable assumption that $q \ll d$, Prior-OPT outperforms Sign-OPT if $\sum_{i=1}^{s} \alpha_i^2 > \frac{2s}{\pi d}$ (where $\frac{2s}{\pi d}$ is an approximate value), which is easily satisfied for large d. See Appendix D for details.

Algorithm 1 summarizes our attack procedure. The initialization of θ_0 has two options in *untargeted attacks*: (1) θ_0^{RND}: we select the best direction with the smallest distortion from 100 random directions

Algorithm 1 Prior-Sign-OPT and Prior-OPT attack

Input: benign image $\mathbf{x}$, objective function $g(\cdot)$, attack success indicator $\Phi(\cdot)$ defined in Eq. (2), iteration T, method $m \in \{$ `Prior-OPT`, `Prior-Sign-OPT`$\}$, the initialization strategy of untargeted attacks `init` $\in \{\theta_0^{\text{PGD}}, \theta_0^{\text{RND}}\}$, the maximum gradient norm $\mathbf{g}_{\max}$, attack norm $p \in \{2, \infty\}$, surrogate models $\mathbb{S} = \{\hat{f}_1, \ldots, \hat{f}_s\}$.
Output: adversarial example $\mathbf{x}^*$ that satisfies $\Phi(\mathbf{x}^*) = 1$.
$\tilde{\mathbf{x}}_0 \leftarrow \text{PGD}(\mathbf{x}, \hat{f}_1)$ if `init` $= \theta_0^{\text{PGD}}$, otherwise a random $\tilde{\mathbf{x}}_0$ that satisfies $\Phi(\tilde{\mathbf{x}}_0) = 1$ is selected for the θ_0^{RND} strategy; ▷ the targeted attack selects an image from the target class as $\tilde{\mathbf{x}}_0$.
$\theta_0 \leftarrow \frac{\tilde{\mathbf{x}}_0 - \mathbf{x}}{\|\tilde{\mathbf{x}}_0 - \mathbf{x}\|_2}, \quad d_0 \leftarrow \|\tilde{\mathbf{x}}_0 - \mathbf{x}\|_p$;
for t **in** $1, \ldots, T$ **do**
  for $\hat{f}_i$ **in** $\mathbb{S}$ **do**
    $\lambda_{t-1} \leftarrow \text{BinarySearch}(\mathbf{x}, \theta_{t-1}, \hat{f}_i, \Phi)$;
    $\mathbf{k}_i \leftarrow \nabla_\theta h(\theta_{t-1}, \lambda_{t-1})$ on $\hat{f}_i$ with λ_{t-1} treated as a constant in differentiation; ▷ obtain s transfer-based priors.
  end for
  $\mathbf{r}_i \sim \mathcal{N}(\mathbf{0}, \mathbf{I})$ for $i = 1, \ldots, q - s$;
  $\mathbf{p}_1, \ldots, \mathbf{p}_s, \mathbf{u}_1, \ldots, \mathbf{u}_{q-s} \leftarrow$ Gram-Schmidt orthonormalization$(\{\mathbf{k}_1, \ldots, \mathbf{k}_s, \mathbf{r}_1, \ldots, \mathbf{r}_{q-s}\})$;
  Estimate a gradient $\mathbf{v}^*$ using Eq. (7) if $m =$ `Prior-Sign-OPT`, otherwise using Eq. (13);
  $\mathbf{v}^* \leftarrow \text{ClipGradNorm}(\mathbf{v}^*, \mathbf{g}_{\max})$;
  $\eta^* \leftarrow \text{LineSearch}(\mathbf{x}, \mathbf{v}^*, \Phi, d_{t-1}, \theta_{t-1})$; ▷ search step size.
  $\theta_t \leftarrow \theta_{t-1} - \eta^* \mathbf{v}^*, \quad \theta_t \leftarrow \frac{\theta_t}{\|\theta_t\|_2}$;
  $d_t \leftarrow \|g(\theta_t) \cdot \theta_t\|_p$;
end for
return $\mathbf{x}^* \leftarrow \mathbf{x} + g(\theta_T) \frac{\theta_T}{\|\theta_T\|_2}$;

as θ_0; (2) θ_0^{PGD}: we apply PGD (Madry et al., 2018) to attack a surrogate model $\hat{f}_1$ to initialize θ_0, which uses the transfer-based attack as initialization. In *targeted attacks*, we initialize θ_0 with an image $\tilde{\mathbf{x}}_0$ selected from the target class in the training set. In each iteration, the algorithm first calculates the gradient of Eq. (4) on each surrogate model $\hat{f}_i$ in $\mathbb{S}$ to obtain the priors $\mathbf{k}_1, \ldots, \mathbf{k}_s$. Then, we combine these priors and the randomly sampled vectors $\mathbf{r}_1, \ldots, \mathbf{r}_{q-s}$ into a list $\mathbb{L}$, where the priors are positioned ahead of the random vectors. After performing Gram-Schmidt orthonormalization on $\mathbb{L}$, the orthonormal vectors $\mathbf{p}_1, \ldots, \mathbf{p}_s, \mathbf{u}_1, \ldots, \mathbf{u}_{q-s}$ are obtained, representing an orthonormal basis of the subspace. With these orthonormal vectors, we estimate the gradient $\mathbf{v}^*$ using Eq. (7) for Prior-Sign-OPT or Eq. (13) for Prior-OPT, respectively. Then, we employ the gradient clipping technique to address the large-norm gradient problem caused by finite difference. Finally, we use line search to find the optimal step size η^* and perform a gradient descent step to minimize $g(\theta)$.

4 Experiments

4.1 Experimental Setting

Datasets. All experiments are conducted on two datasets, i.e., CIFAR-10 (Krizhevsky & Hinton, 2009) and ImageNet (Deng et al., 2009). The image sizes are $32 \times 32 \times 3$ for CIFAR-10, and either $299 \times 299 \times 3$ or $224 \times 224 \times 3$ for ImageNet. We randomly select 1,000 images from the validation sets for experiments. In targeted attacks, for the same target class, we use the same image $\tilde{\mathbf{x}}_0$ as the initialization for all methods. We set the target label as $y_{adv} = (y + 1) \mod C$, where y is the true label and C is the number of classes. Results of the CIFAR-10 dataset are presented in Appendix G.5.

Method Setting. The hyperparameter settings of all methods are listed in Appendix F. In the experiments, surrogate models are denoted as subscripts in the method names. For instance, Prior-OPT$_{\text{ResNet50\&ConViT}}$ means using ResNet-50 and ConViT as the surrogate models for Prior-OPT, and Prior-OPT$_{\theta_0^{\text{PGD}} + \text{ResNet50}}$ applies PGD attack on the surrogate model ResNet-50 to initialize θ_0.

Compared Methods. To provide a comprehensive comparison, we select 11 state-of-the-art hard-label attacks, including Sign-OPT, SVM-OPT (Cheng et al., 2020), HSJA (Chen et al., 2020),

Triangle Attack (Wang et al., 2022), TA, G-TA (Ma et al., 2021b), SurFree (Maho et al., 2021), GeoDA (Rahmati et al., 2020), Evolutionary (Dong et al., 2019), BBA (Brunner et al., 2019), and SQBA (Park et al., 2024). SQBA, Triangle Attack, GeoDA, and our θ_0^{PGD} initialization strategy (e.g., Prior-OPT$_{\theta_0^{\text{PGD}}+\text{ResNet50}}$) only support untargeted attacks. Both BBA and SQBA use a single surrogate model, denoted as a subscript in the method name (e.g., SQBA$_{\text{ResNet50}}$).

Target Models and Surrogate Models. In the ImageNet dataset, we select 8 neural network architectures as the target models, including Convolutional Neural Networks (CNNs) and Vision Transformers (ViTs). The selected target models are Inception-v3 (Szegedy et al., 2016), Inception-v4 (Szegedy et al., 2017), ResNet-101 (He et al., 2016), SENet-154 (Hu et al., 2018), ResNeXt-101 (64×4d) (Xie et al., 2017), Vision Transformer (ViT) (Dosovitskiy et al., 2021), Swin Transformer (Liu et al., 2021), and Global Context Vision Transformer (GC ViT) (Hatamizadeh et al., 2023). The Inception-v3 and Inception-v4 require a resolution of 299×299 for the input images, and we select Inception-ResNet-v2 (IncResV2) and Xception as the surrogate models. ResNet-50 (He et al., 2016) and ConViT (D'Ascoli et al., 2021) are selected as the surrogate models for the remaining target models. In the attacks on defense models, we use the adversarially trained (AT) surrogate models (e.g., AT(ResNet110)), which are marked as subscripts in the method names, such as Prior-OPT$_{\text{AT(ResNet110)}}$.

Evaluation Metric. All methods are evaluated using the mean distortion over 1,000 images as $\frac{1}{|\mathbf{X}|}\sum_{\mathbf{x}\in\mathbf{X}}(\|\mathbf{x}_{\text{adv}}-\mathbf{x}\|_p)$ under different query budgets, where $\mathbf{X}$ is the test set and $p \in \{2, \infty\}$ is the attack norm. We also report the attack success rate (ASR) under the specific query budget, which is defined as the percentage of samples with distortions below a threshold ϵ. In ℓ_2 norm attacks, we set the threshold $\epsilon = \sqrt{0.001 \times d}$ on the ImageNet dataset, where d is the image dimension. Following Li et al. (2021), we calculate the area under the curve (AUC) of ℓ_2 distortions versus queries.

4.2 Comparison with State-of-the-Art Attacks

Table 1: Mean ℓ_2 distortions of different query budgets on the ImageNet dataset.

Target Model	Method	Untargeted Attack					Targeted Attack						
		@1K	@2K	@5K	@8K	@10K	@1K	@2K	@5K	@8K	@10K	@15K	@20K
Inception-v4	HSJA (Chen et al., 2020)	75.392	44.530	20.567	14.194	11.645	95.876	79.001	52.176	39.190	32.951	24.546	19.522
	TA (Ma et al., 2021b)	67.496	42.233	20.352	14.175	11.694	78.883	61.990	40.669	31.506	27.111	21.079	17.319
	G-TA (Ma et al., 2021b)	67.842	41.946	19.962	13.865	11.448	79.297	62.291	40.529	30.941	26.427	20.268	16.569
	Sign-OPT (Cheng et al., 2020)	86.716	48.233	18.258	11.067	8.786	80.366	65.200	42.866	32.104	27.526	20.394	16.281
	SVM-OPT (Cheng et al., 2020)	89.863	47.914	18.297	11.091	8.839	79.807	65.590	43.426	33.090	28.797	22.354	18.795
	GeoDA (Rahmati et al., 2020)	29.157	20.119	12.487	11.010	9.688	-	-	-	-	-	-	-
	Evolutionary (Dong et al., 2019)	61.966	42.665	20.815	13.382	10.839	81.761	65.060	43.021	32.120	27.385	19.942	15.610
	SurFree (Maho et al., 2021)	51.685	38.482	22.845	16.374	13.818	84.925	74.887	55.991	44.475	39.004	29.354	23.153
	Triangle Attack (Wang et al., 2022)	27.217	25.853	23.743	22.581	22.132	-	-	-	-	-	-	-
	SQBA$_{\text{IncResV2}}$ (Park et al., 2024)	26.134	19.035	11.189	8.432	7.417	-	-	-	-	-	-	-
	SQBA$_{\text{Xception}}$ (Park et al., 2024)	23.672	17.424	10.502	8.036	7.115	-	-	-	-	-	-	-
	BBA$_{\text{IncResV2}}$ (Brunner et al., 2019)	38.782	28.437	18.757	15.474	14.191	66.746	56.283	41.324	34.066	30.942	25.757	22.630
	BBA$_{\text{Xception}}$ (Brunner et al., 2019)	43.317	31.519	20.504	16.712	15.282	63.069	53.363	39.740	33.166	30.221	25.438	22.561
	Prior-Sign-OPT$_{\text{IncResV2}}$	81.991	42.403	12.835	7.365	5.842	74.597	55.421	31.856	22.958	19.513	14.361	11.665
	Prior-Sign-OPT$_{\text{IncResV2\&Xception}}$	77.683	37.099	9.058	5.195	4.199	69.526	49.368	**26.882**	**19.324**	**16.697**	**12.821**	**10.769**
	Prior-Sign-OPT$_{\theta_0^{\text{PGD}}+\text{IncResV2}}$	23.596	15.347	8.074	5.729	4.863	-	-	-	-	-	-	-
	Prior-OPT$_{\text{IncResV2}}$	49.279	18.135	5.718	4.451	4.027	67.300	49.842	33.477	27.602	25.281	21.837	19.800
	Prior-OPT$_{\text{IncResV2\&Xception}}$	42.541	13.418	**3.919**	**3.321**	**3.119**	**60.211**	**42.631**	27.547	23.011	21.441	19.193	17.983
	Prior-OPT$_{\theta_0^{\text{PGD}}+\text{IncResV2}}$	**22.852**	**12.194**	6.568	5.114	4.548	-	-	-	-	-	-	-
ViT	HSJA (Chen et al., 2020)	37.813	19.386	9.031	6.604	5.637	61.491	44.853	23.947	16.926	14.152	10.791	8.922
	TA (Ma et al., 2021b)	37.923	19.867	9.078	6.636	5.674	52.110	36.455	**20.536**	15.145	12.885	10.158	8.609
	G-TA (Ma et al., 2021b)	37.425	19.347	8.948	6.496	5.643	52.550	36.720	20.857	15.436	13.255	10.490	8.933
	Sign-OPT (Cheng et al., 2020)	51.120	25.290	8.559	5.482	4.572	55.941	41.867	23.784	16.541	13.873	10.129	8.267
	SVM-OPT (Cheng et al., 2020)	55.802	26.580	9.242	5.988	5.070	56.002	41.899	23.909	17.273	14.848	11.739	10.320
	GeoDA (Rahmati et al., 2020)	18.880	12.904	8.039	7.153	6.313	-	-	-	-	-	-	-
	Evolutionary (Dong et al., 2019)	40.382	25.709	11.925	7.974	6.719	57.141	40.187	21.782	15.191	12.795	9.677	8.311
	SurFree (Maho et al., 2021)	28.228	19.016	10.194	7.321	6.303	70.337	53.129	30.054	20.595	16.908	11.794	9.204
	Triangle Attack (Wang et al., 2022)	**12.789**	12.144	11.064	10.411	10.097	-	-	-	-	-	-	-
	SQBA$_{\text{ResNet50}}$ (Park et al., 2024)	21.741	14.004	7.738	5.861	5.201	-	-	-	-	-	-	-
	SQBA$_{\text{ConViT}}$ (Park et al., 2024)	12.886	9.762	6.240	4.947	4.452	-	-	-	-	-	-	-
	BBA$_{\text{ResNet50}}$ (Brunner et al., 2019)	29.755	20.053	12.580	10.375	9.567	**43.231**	**33.365**	21.889	17.635	16.046	13.726	12.463
	BBA$_{\text{ConViT}}$ (Brunner et al., 2019)	22.716	16.153	10.893	9.193	8.595	45.588	35.227	22.865	18.325	16.614	14.028	12.623
	Prior-Sign-OPT$_{\text{ResNet50}}$	50.161	27.953	9.474	5.872	4.850	55.095	40.480	22.354	15.626	13.201	9.789	8.048
	Prior-Sign-OPT$_{\text{ResNet50\&ConViT}}$	46.196	23.869	7.327	4.694	3.967	53.925	38.418	20.673	**14.422**	**12.153**	**9.090**	**7.544**
	Prior-Sign-OPT$_{\theta_0^{\text{PGD}}+\text{ResNet50}}$	29.912	18.425	7.848	5.175	4.331	-	-	-	-	-	-	-
	Prior-OPT$_{\text{ResNet50}}$	42.838	22.704	8.848	6.024	5.195	54.348	40.930	24.408	18.117	15.803	12.638	11.070
	Prior-OPT$_{\text{ResNet50\&ConViT}}$	26.495	**11.287**	**4.929**	**3.937**	**3.609**	53.369	40.002	24.706	19.148	17.116	14.114	12.650
	Prior-OPT$_{\theta_0^{\text{PGD}}+\text{ResNet50}}$	29.099	17.754	8.208	5.782	5.009	-	-	-	-	-	-	-

Table 2: Mean ℓ_2 distortions of the different numbers of priors on the ImageNet dataset.

Method	Priors	Target Model: ResNet-101[1]					Target Model: Swin Transformer[2]					Target Model: GC ViT[2]				
		@1K	@2K	@5K	@8K	@10K	@1K	@2K	@5K	@8K	@10K	@1K	@2K	@5K	@8K	@10K
Sign-OPT	no prior	37.248	21.235	8.982	5.811	4.754	86.373	53.399	20.686	12.406	9.899	57.903	35.762	14.763	9.047	7.185
Prior-Sign-OPT	1 prior	34.150	18.733	6.111	3.718	3.019	84.124	52.882	20.344	11.880	9.254	57.171	36.949	14.963	8.931	6.899
	2 priors	32.848	17.548	5.121	3.136	2.593	77.459	43.062	13.614	7.903	6.331	54.896	32.418	11.012	6.651	5.342
	3 priors	31.156	15.455	4.074	2.527	2.122	73.110	37.852	10.264	5.939	4.778	52.744	28.939	8.707	5.245	4.215
	4 priors	29.984	14.707	3.698	2.333	1.989	70.246	34.470	8.526	5.066	4.169	50.256	26.027	6.435	3.804	3.212
	5 priors	**29.601**	**14.195**	**3.573**	**2.275**	**1.951**	**67.616**	**32.225**	**7.321**	**4.219**	**3.467**	**48.935**	**24.821**	**6.123**	**3.601**	**2.893**
Prior-OPT	1 prior	18.355	7.100	2.840	2.324	2.158	69.432	39.447	16.536	11.241	9.625	50.467	29.091	11.537	7.311	5.948
	2 priors	17.373	6.465	2.454	2.096	1.979	41.152	17.977	7.289	5.453	4.896	36.055	16.176	6.094	4.413	3.747
	3 priors	15.373	5.350	1.919	1.714	1.653	**36.636**	13.877	5.166	4.008	3.687	**33.181**	13.005	4.702	3.644	3.264
	4 priors	**15.422**	**5.220**	**1.849**	**1.654**	**1.596**	38.343	12.650	3.784	3.027	2.850	34.396	10.994	3.047	2.356	2.171
	5 priors	15.556	5.395	1.881	1.672	1.605	37.712	**12.070**	**3.488**	**2.747**	**2.577**	33.351	**10.369**	**2.921**	**2.329**	**2.159**

[1] Five surrogate models: ResNet-50, SENet-154, ResNeXt-101 (64 × 4d), VGG-13, SqueezeNet v1.1
[2] Five surrogate models: ResNet-50, ConViT, CrossViT, MaxViT, ViT

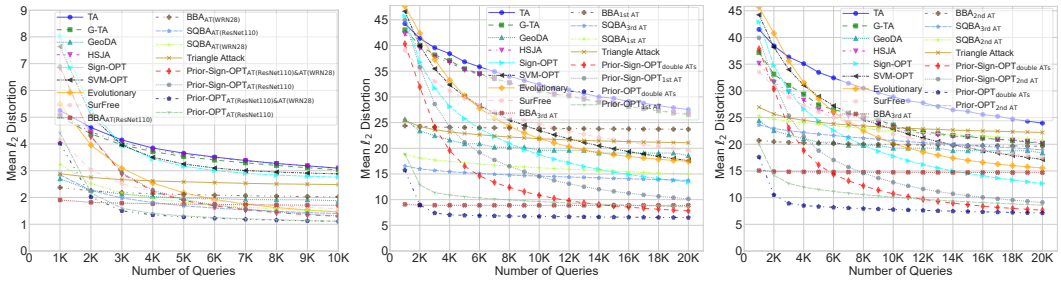

(a) TRADES$_{\epsilon_\infty=8/255}$ (CIFAR-10) (b) AT$_{\epsilon_\infty=4/255}$ (ImageNet)[1] (c) AT$_{\epsilon_\infty=8/255}$ (ImageNet)[2]

Figure 3: Mean distortions of untargeted attacks on the defense models equipped with the ResNet-50.

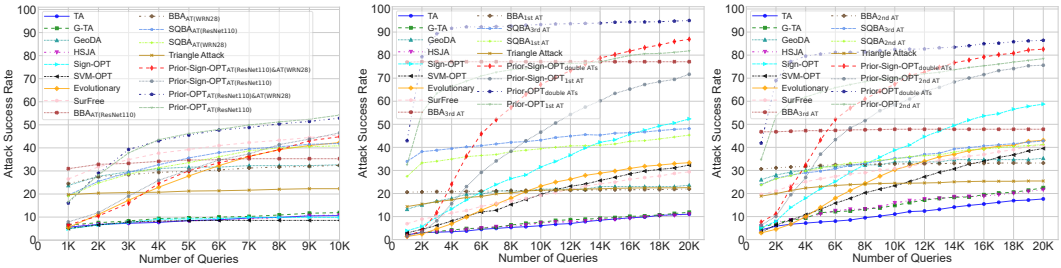

(a) TRADES (CIFAR-10) (b) AT$_{\epsilon_\infty=4/255}$ (ImageNet)[1] (c) AT$_{\epsilon_\infty=8/255}$ (ImageNet)[2]

Figure 4: Attack success rates of untargeted attacks with ℓ_2 norm constraint against defense models.

Results of Attacks against Undefended Models. Table 1 shows the results of attacks against undefended models on the ImageNet dataset. Additional results are in Appendix G.5. In summary:

(1) In untargeted attacks (Table 1 and Fig. 7), the performance of Prior-OPT significantly surpasses that of all methods, and using multiple surrogate models yields better performance than using a single surrogate model. In addition, the PGD initialization (θ_0^{PGD}) proves effective in early iterations, because it establishes a high-quality initial attack direction θ_0 through transfer-based attacks.

(2) In targeted attacks, Prior-OPT outperforms Prior-Sign-OPT when the query budget is below $5{,}000$, while Prior-Sign-OPT performs better in later iterations with more queries.

(3) Table 2 and Fig. 5c demonstrate that using more surrogate models (priors) can boost performance.

[1] 1st AT: AT(ResNet-50, $\epsilon_{\ell_\infty} = 8/255$), 3rd AT: AT(ResNet-50, $\epsilon_{\ell_2} = 3$), double ATs: combination of both
[2] 2nd AT: AT(ResNet-50, $\epsilon_{\ell_\infty} = 4/255$), 3rd AT: AT(ResNet-50, $\epsilon_{\ell_2} = 3$), double ATs: combination of both

Results of Attacks against Defense Models. We conduct untargeted attack experiments against two types of defense models, i.e., adversarial training (AT) (Madry et al., 2018) and TRADES (Zhang et al., 2019). Figs. 3 and 4 show that Prior-OPT with two surrogate models (Prior-OPT$_{\text{double ATs}}$) achieves the best performance on the ImageNet dataset and the CIFAR-10 dataset.

4.3 Comprehensive Understanding of Prior-OPT

In the ablation studies, we conduct control experiments based on theoretical analysis results and attacks on real images (Fig. 5). In Figs. 5a, 5b, and 5c, we set the image dimension to $d = 3{,}072$ and use $\mathbb{E}[\gamma]$ (Eq. (9) for Sign-OPT, Eq. (11) for Prior-Sign-OPT, Eq. (15) and Eq. (16) for the lower and upper bound of Prior-OPT) as the metric for gradient estimation accuracy, where $\gamma = \overline{\mathbf{v}^*}^\top \overline{\nabla g(\theta)}$. Figs. 5a and 5c are based on $q = 50$. Fig. 5a uses one prior and shows that Prior-OPT and Prior-Sign-OPT outperform Sign-OPT with different values of α. Fig. 5a also shows that Prior-Sign-OPT performs well when α is small and $\mathbb{E}[\gamma]$ decreases when α is close to 1. This is because when we set $\alpha = 1$, $\mathbb{E}[\gamma] = 1/\sqrt{q}$ in Eq. (11). Fig. 5b shows that $\mathbb{E}[\gamma]$ monotonically increases with q for each method, and Prior-Sign-OPT performs worse than Sign-OPT when $q > 500$. Fig. 5c validates that the performance can be improved when more priors are available, and prioritizing surrogate models with larger α values outperforms random selection. Fig. 5c is consistent with the conclusion of the experimental results in Table 2. Fig. 5d shows the untargeted attack results of Prior-OPT against Swin Transformer with varying q on ImageNet. A smaller q achieves better performance in the early iterations, but becomes less effective in the late stage of iterations with a higher number of queries.

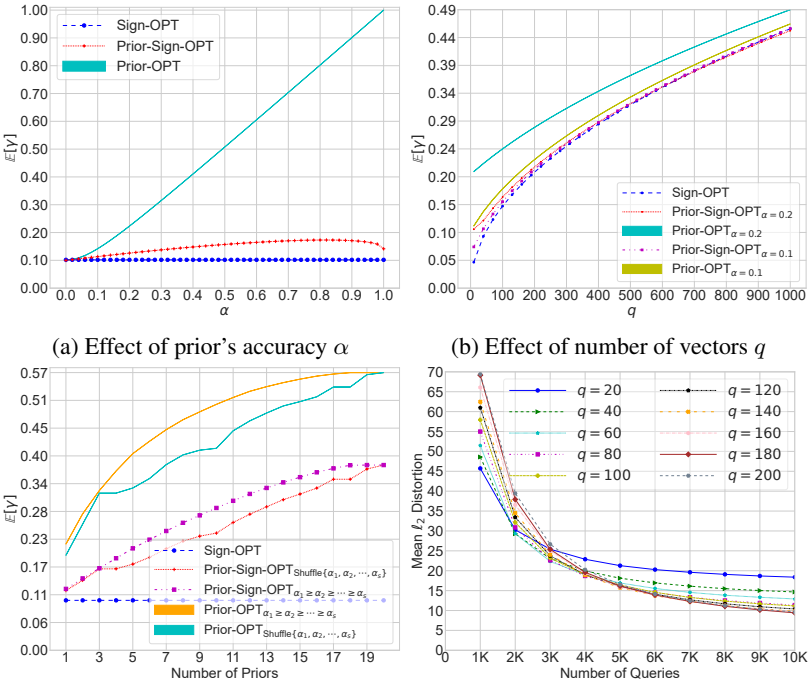

(a) Effect of prior's accuracy α

(b) Effect of number of vectors q

(c) Effect of number of priors

(d) Prior-OPT with different q

Figure 5: Results of ablation studies. Figs. 5a, 5b, and 5c are based on Eqs. (9), (11), (15), and (16).

5 Conclusion

In this paper, we propose novel hard-label attacks (i.e., Prior-OPT and Prior-Sign-OPT) that incorporate transfer-based priors into the gradient estimation of the ray direction and significantly boost the attack performance. Through theoretical analysis, we prove the effectiveness of our approach: we derive expressions for the expected cosine similarities between the estimated and true gradients, enabling theoretical comparison against the baseline. Therefore, our analysis offers a comprehensive understanding of Prior-OPT and Prior-Sign-OPT. Lastly, we evaluate our approach through extensive experiments, demonstrating superior performance compared to state-of-the-art methods.

ACKNOWLEDGMENTS

This work was supported by Key R&D Program of Zhejiang under Grant No. 2024C01164, by Zhejiang Provincial Natural Science Foundation of China under Grant No. LMS25F020005, and by the National Natural Science Foundation of China under Grant No. U21B2001.

ETHICS STATEMENT

We affirm our commitment to the ICLR Code of Ethics to ensure that our research on adversarial examples and AI security adheres to the highest ethical standards. Our work aims to identify potential vulnerabilities in AI systems with the intention of enhancing their security and resilience. Specifically, our approach can be integrated into the evaluation process for a model's robustness, enabling the study and implementation of targeted defense strategies and providing effective support to strengthen the security specifications of artificial intelligence models. We acknowledge the dual-use nature of this research. We have taken steps to responsibly share our findings, encouraging their use in developing robust defense mechanisms. We remain open to discussions about any ethical concerns that may arise and are dedicated to contributing positively to the field of AI security.

REPRODUCIBILITY STATEMENT

We have taken several steps to ensure the reproducibility of our research. The appendix provides comprehensive details on the algorithm settings, computational resources, and theoretical proofs. To further support reproducibility, we provide the complete attack code for our approach and all baseline methods at `https://github.com/machanic/hard_label_attacks`. These resources are intended to enable others to replicate our experiments.

REFERENCES

Wieland Brendel, Jonas Rauber, and Matthias Bethge. Decision-based adversarial attacks: reliable attacks against black-box machine learning models. In *International Conference on Learning Representations*, pp. 1–12, 2018.

T. Brunner, F. Diehl, M. T. Le, and A. Knoll. Guessing smart: biased sampling for efficient black-box adversarial attacks. In *IEEE/CVF International Conference on Computer Vision*, pp. 4957–4965, 2019.

Jianbo Chen, Jordan Michael I., and Wainwright Martin J. HopSkipJumpAttack: a query-efficient decision-based adversarial attack. In *IEEE Symposium on Security and Privacy*, pp. 1277–1294, 2020.

Jinghui Chen and Quanquan Gu. RayS: a ray searching method for hard-label adversarial attack. In *ACM SIGKDD International Conference on Knowledge Discovery and Data Mining*, pp. 1739–1747, 2020.

Minhao Cheng, Thong Le, Pin-Yu Chen, Huan Zhang, JinFeng Yi, and Cho-Jui Hsieh. Query-efficient hard-label black-box attack: an optimization-based approach. In *International Conference on Learning Representations*, 2019. URL `https://openreview.net/forum?id=rJlk6iRqKX`.

Minhao Cheng, Simranjit Singh, Pin-Yu Chen, Sijia Liu, and Cho-Jui Hsieh. Sign-OPT: a query-efficient hard-label adversarial attack. In *International Conference on Learning Representations*, 2020. URL `https://openreview.net/forum?id=SklTQCNtvS`.

Shuyu Cheng, Guoqiang Wu, and Jun Zhu. On the convergence of prior-guided zeroth-order optimization algorithms. In *Advances in Neural Information Processing Systems*, volume 34, pp. 14620–14631, 2021.

Stéphane D'Ascoli, Hugo Touvron, Matthew L Leavitt, Ari S Morcos, Giulio Biroli, and Levent Sagun. ConViT: improving Vision Transformers with soft convolutional inductive biases. In

International Conference on Machine Learning, volume 139 of *Proceedings of Machine Learning Research*, pp. 2286–2296, 2021.

Jia Deng, Wei Dong, Richard Socher, Li-Jia Li, Kai Li, and Li Fei-Fei. ImageNet: a large-scale hierarchical image database. In *IEEE Conference on Computer Vision and Pattern Recognition*, pp. 248–255, 2009. doi: 10.1109/CVPR.2009.5206848.

Yinpeng Dong, Hang Su, Baoyuan Wu, Zhifeng Li, Wei Liu, Tong Zhang, and Jun Zhu. Efficient decision-based black-box adversarial attacks on face recognition. In *IEEE/CVF Conference on Computer Vision and Pattern Recognition*, pp. 7714–7722, 2019.

Yinpeng Dong, Shuyu Cheng, Tianyu Pang, Hang Su, and Jun Zhu. Query-efficient black-box adversarial attacks guided by a transfer-based prior. *IEEE Transactions on Pattern Analysis and Machine Intelligence*, 44(12):9536–9548, 2022. doi: 10.1109/TPAMI.2021.3126733.

Alexey Dosovitskiy, Lucas Beyer, Alexander Kolesnikov, Dirk Weissenborn, Xiaohua Zhai, Thomas Unterthiner, Mostafa Dehghani, Matthias Minderer, Georg Heigold, Sylvain Gelly, Jakob Uszkoreit, and Neil Houlsby. An image is worth 16x16 words: Transformers for image recognition at scale. In *International Conference on Learning Representations*, 2021. URL `https://openreview.net/forum?id=YicbFdNTTy`.

Dongyoon Han, Jiwhan Kim, and Junmo Kim. Deep pyramidal residual networks. In *IEEE Conference on Computer Vision and Pattern Recognition*, pp. 5927–5935, 2017.

Ali Hatamizadeh, Hongxu Yin, Greg Heinrich, Jan Kautz, and Pavlo Molchanov. Global Context Vision Transformers. In *International Conference on Machine Learning*, volume 202 of *Proceedings of Machine Learning Research*, pp. 12633–12646, 2023.

Kaiming He, Xiangyu Zhang, Shaoqing Ren, and Jian Sun. Deep residual learning for image recognition. In *IEEE Conference on Computer Vision and Pattern Recognition*, pp. 770–778, 2016.

Jie Hu, Li Shen, and Gang Sun. Squeeze-and-excitation networks. In *IEEE/CVF Conference on Computer Vision and Pattern Recognition*, pp. 7132–7141, 2018.

Gao Huang, Zhuang Liu, Laurens Van Der Maaten, and Kilian Q Weinberger. Densely connected convolutional networks. In *IEEE conference on computer vision and pattern recognition*, pp. 4700–4708, 2017.

Alex Krizhevsky and Geoffrey Hinton. Learning multiple layers of features from tiny images. Technical Report 0, University of Toronto, 2009. URL `https://www.cs.toronto.edu/~kriz/learning-features-2009-TR.pdf`.

Jie Li, Rongrong Ji, Peixian Chen, Baochang Zhang, Xiaopeng Hong, Ruixin Zhang, Shaoxin Li, Jilin Li, Feiyue Huang, and Yongjian Wu. Aha! Adaptive history-driven attack for decision-based black-box models. In *IEEE/CVF International Conference on Computer Vision*, pp. 16168–16177, 2021.

Ze Liu, Yutong Lin, Yue Cao, Han Hu, Yixuan Wei, Zheng Zhang, Stephen Lin, and Baining Guo. Swin Transformer: hierarchical vision transformer using shifted windows. In *IEEE/CVF International Conference on Computer Vision*, pp. 10012–10022, 2021.

Chen Ma, Li Chen, and Jun-Hai Yong. Simulating unknown target models for query-efficient black-box attacks. In *IEEE/CVF Conference on Computer Vision and Pattern Recognition*, pp. 11835–11844, 2021a.

Chen Ma, Xiangyu Guo, Li Chen, Jun-Hai Yong, and Yisen Wang. Finding optimal tangent points for reducing distortions of hard-label attacks. In *Advances in Neural Information Processing Systems*, volume 34, pp. 19288–19300, 2021b.

Aleksander Madry, Aleksandar Makelov, Ludwig Schmidt, Dimitris Tsipras, and Adrian Vladu. Towards deep learning models resistant to adversarial attacks. In *International Conference on Learning Representations*, 2018. URL `https://openreview.net/forum?id=rJzIBfZAb`.

Thibault Maho, Teddy Furon, and Erwan Le Merrer. SurFree: a fast surrogate-free black-box attack. In *IEEE/CVF Conference on Computer Vision and Pattern Recognition*, pp. 10430–10439, 2021.

Florian Meier, Asier Mujika, Marcelo Matheus Gauy, and Angelika Steger. Improving gradient estimation in evolutionary strategies with past descent directions. *arXiv preprint arXiv:1910.05268*, 2019.

Seyed-Mohsen Moosavi-Dezfooli, Alhussein Fawzi, and Pascal Frossard. DeepFool: a simple and accurate method to fool deep neural networks. In *IEEE Conference on Computer Vision and Pattern Recognition*, pp. 2574–2582, 2016.

Yurii Nesterov and Vladimir Spokoiny. Random gradient-free minimization of convex functions. *Foundations of Computational Mathematics*, 17(2):527–566, 2017.

Jeonghwan Park, Paul Miller, and Niall McLaughlin. Hard-label based small query black-box adversarial attack. In *IEEE/CVF Winter Conference on Applications of Computer Vision*, pp. 3986–3995, 2024.

Ali Rahmati, Seyed-Mohsen Moosavi-Dezfooli, Pascal Frossard, and Huaiyu Dai. GeoDA: a geometric framework for black-box adversarial attacks. In *IEEE/CVF Conference on Computer Vision and Pattern Recognition*, pp. 8446–8455, 2020.

Md Farhamdur Reza, Ali Rahmati, Tianfu Wu, and Huaiyu Dai. CGBA: curvature-aware geometric black-box attack. In *IEEE/CVF International Conference on Computer Vision*, pp. 124–133, 2023.

Oswaldo Rio Branco de Oliveira. The implicit and the inverse function theorems: easy proofs. *arXiv preprint arXiv:1212.2066*, 2012.

Yucheng Shi, Yahong Han, Qinghua Hu, Yi Yang, and Qi Tian. Query-efficient black-box adversarial attack with customized iteration and sampling. *IEEE Transactions on Pattern Analysis and Machine Intelligence*, 45(2):2226–2245, 2023. doi: 10.1109/TPAMI.2022.3169802.

Christian Szegedy, Vincent Vanhoucke, Sergey Ioffe, Jon Shlens, and Zbigniew Wojna. Rethinking the Inception architecture for computer vision. In *IEEE Conference on Computer Vision and Pattern Recognition*, pp. 2818–2826, 2016.

Christian Szegedy, Sergey Ioffe, Vincent Vanhoucke, and Alexander A. Alemi. Inception-v4, Inception-ResNet and the impact of residual connections on learning. In *AAAI Conference on Artificial Intelligence*, pp. 4278—4284, 2017.

Michail Tsagris, Christina Beneki, and Hossein Hassani. On the folded normal distribution. *Mathematics*, 2(1):12–28, 2014. ISSN 2227-7390. doi: 10.3390/math2010012.

Xiaosen Wang, Zeliang Zhang, Kangheng Tong, Dihong Gong, Kun He, Zhifeng Li, and Wei Liu. Triangle Attack: a query-efficient decision-based adversarial attack. In *European Conference on Computer Vision*, pp. 156–174, 2022.

Saining Xie, Ross Girshick, Piotr Dollar, Zhuowen Tu, and Kaiming He. Aggregated residual transformations for deep neural networks. In *IEEE Conference on Computer Vision and Pattern Recognition*, pp. 1492–1500, 2017.

Yoshihiro Yamada, Masakazu Iwamura, Takuya Akiba, and Koichi Kise. Shakedrop regularization for deep residual learning. *IEEE Access*, 7:186126–186136, 2019. doi: 10.1109/ACCESS.2019.2960566.

Sergey Zagoruyko and Nikos Komodakis. Wide residual networks. In *British Machine Vision Conference*, pp. 87.1–87.12, 2016. doi: 10.5244/C.30.87.

Hongyang Zhang, Yaodong Yu, Jiantao Jiao, Eric Xing, Laurent El Ghaoui, and Michael Jordan. Theoretically principled trade-off between robustness and accuracy. In *International Conference on Machine Learning*, volume 97 of *Proceedings of Machine Learning Research*, pp. 7472–7482, 2019.

APPENDIX

A PROOF FOR SURROGATE GRADIENT COMPUTATION

For a surrogate model $\hat{f}$, we define f as the negative C&W loss function as follows.

$$f(\mathbf{x}') \coloneqq \begin{cases} \hat{f}(\mathbf{x}')_y - \max_{j \neq y} \hat{f}(\mathbf{x}')_j, & \text{if untargeted attack,} \\ \max_{j \neq \hat{y}_{\text{adv}}} \hat{f}(\mathbf{x}')_j - \hat{f}(\mathbf{x}')_{\hat{y}_{\text{adv}}}, & \text{if targeted attack,} \end{cases} \tag{18}$$

where $\hat{f}(\mathbf{x}')_i$ denotes the i-th element of the output of $\hat{f}(\mathbf{x}')$. Note that $h(\theta, \lambda)$ defined in Eq. (4) of the main text equals $f\left(\mathbf{x} + \lambda \cdot \frac{\theta}{\|\theta\|}\right)$. Now we consider $g(\theta)$, the distance from the benign image $\mathbf{x}$ to the adversarial region along the ray direction θ, as defined in Eq. (3). For any $\mathbf{x}'$, $\Phi(\mathbf{x}') = 1 \Leftrightarrow f(\mathbf{x}') \leq 0$, so we have

$$g(\theta) = \inf\left\{\lambda : \lambda > 0, f\big(\mathbf{x} + \lambda \frac{\theta}{\|\theta\|}\big) \leq 0\right\}, \tag{19}$$

where $\inf(\cdot)$ denotes the infimum of a subset of $\mathbb{R}$. We define $g(\theta) = +\infty$ when no valid λ exists, since $\inf \emptyset = +\infty$ by convention. Now we can prove the following proposition.

Proposition A.1. *If f is continuous, $f(\mathbf{x}) > 0$, then given any $\theta \neq \mathbf{0}$ s.t. $g(\theta) < +\infty$, we have $g(\theta) > 0$ and $f\left(\mathbf{x} + g(\theta)\frac{\theta}{\|\theta\|}\right) = 0$.*

Proof. We first prove that $g(\theta) > 0$. We begin by defining the function $f_\theta(\lambda) \coloneqq f\left(\mathbf{x} + \lambda \cdot \frac{\theta}{\|\theta\|}\right)$. Note that f_θ is continuous (w.r.t. λ) because f is continuous. Since $f_\theta(0) = f(\mathbf{x}) > 0$, there exists $\delta > 0$ such that $\forall 0 < \lambda < \delta$, $f_\theta(\lambda) > 0$. Since $g(\theta) < +\infty$, by the definition we have $g(\theta) = \inf(\{\lambda : \lambda > 0, f_\theta(\lambda) \leq 0\}) \geq \delta > 0$.

Next, we want to prove $f\left(\mathbf{x} + g(\theta)\frac{\theta}{\|\theta\|}\right) = 0$, i.e., $f_\theta(g(\theta)) = 0$. To simplify notation in the proof, let us denote $A_\theta \coloneqq \{\lambda : \lambda > 0, f_\theta(\lambda) \leq 0\}$.

If $f_\theta(g(\theta)) < 0$, then since f_θ is continuous and $g(\theta) > 0$, there exists $\epsilon > 0$ such that $f_\theta(g(\theta) - \epsilon) < 0$ and $g(\theta) - \epsilon > 0$. Therefore, we have $g(\theta) - \epsilon \in A_\theta$, which implies that $g(\theta) > \inf(A_\theta)$. This contradicts the definition $g(\theta) = \inf(A_\theta)$.

If $f_\theta(g(\theta)) > 0$, then there exists $\epsilon > 0$ such that $f_\theta(\lambda) > 0$ holds for all $g(\theta) \leq \lambda \leq g(\theta) + \epsilon$. This means that $[g(\theta), g(\theta) + \epsilon] \cap A_\theta = \emptyset$. Noting that $g(\theta)$ is a lower bound of A_θ, this implies that $g(\theta) + \epsilon$ is also a lower bound of A_θ, which contradicts the definition $g(\theta) = \inf(A_\theta)$.

Therefore $f_\theta(g(\theta)) = 0$. □

Next, we show how to calculate $\nabla g(\theta)$ based on some weak assumptions.

Theorem A.2. *Suppose f is continuously differentiable[2] and $f(\mathbf{x}) > 0$. Let $h(\theta, \lambda) = f\left(\mathbf{x} + \lambda \frac{\theta}{\|\theta\|}\right)$. For any $\theta_0 \neq \mathbf{0}$ s.t. $g(\theta_0) < +\infty$, let $\lambda_0 = g(\theta_0)$, and assume that $\frac{\partial h}{\partial \lambda}(\theta_0, \lambda_0) \neq 0$, then we conclude that g is differentiable at θ_0, and*

$$\nabla g(\theta_0) = -\frac{1}{\frac{\partial h}{\partial \lambda}(\theta_0, \lambda_0)} \nabla_\theta h(\theta_0, \lambda_0). \tag{20}$$

Remark A.3. The assumptions in the theorem are rather weak. $f(\mathbf{x}) > 0$ (the unperturbed sample can be successfully classified) is a standard assumption; $g(\theta_0) < +\infty$ is a common assumption, necessary for ray search procedure to work; f is continuously differentiable almost everywhere under common network architectures. The only special condition required here is that $\frac{\partial h}{\partial \lambda}(\theta_0, \lambda_0) \neq 0$, which is generally satisfied unless a specific function f is explicitly constructed to violate it. Intuitively, as λ increases, the function value decreases from a positive value to a non-positive value, and the derivative w.r.t. λ is typically non-zero when the function value crosses zero.

[2] A function f is said to be continuously differentiable if all partial derivatives of f exist and are continuous.

Proof. Since $(\theta, \lambda) \mapsto \mathbf{x} + \lambda \frac{\theta}{\|\theta\|}$ is continuously differentiable at $\{(\theta, \lambda) : \theta \in \mathbb{R}^d, \lambda \in \mathbb{R}, \theta \neq \mathbf{0}\}$ and f is continuously differentiable everywhere, h is continuously differentiable when $\theta \neq \mathbf{0}$ by the chain rule. By Proposition A.1, $h(\theta_0, \lambda_0) = 0$. Since $\frac{\partial h}{\partial \lambda}(\theta_0, \lambda_0) \neq 0$, by the Implicit Function Theorem (see Theorem 1 in Rio Branco de Oliveira (2012)), there exists a neighborhood $\Theta \subseteq \mathbb{R}^d$ of θ_0 and an open interval $\Lambda := (\lambda_0 - \eta, \lambda_0 + \eta)$ such that for each $\theta \in \Theta$, there is a unique $\lambda \in \Lambda$ satisfying $h(\theta, \lambda) = 0$. Since θ uniquely determines λ, we define $\tilde{g} : \Theta \to \Lambda$ satisfying $h(\theta, \tilde{g}(\theta)) = 0$ for all $\theta \in \Theta$. Moreover, the Implicit Function Theorem tells us that $\tilde{g}$ is continuously differentiable, and

$$\nabla \tilde{g}(\theta_0) = -\frac{1}{\frac{\partial h}{\partial \lambda}(\theta_0, \lambda_0)} \nabla_\theta h(\theta_0, \lambda_0). \tag{21}$$

Now it suffices to prove g is differentiable at θ_0 and $\nabla g(\theta_0) = \nabla \tilde{g}(\theta_0)$. We shall prove that there exists a neighborhood of θ_0 in which g and $\tilde{g}$ are equal. Since $h(\theta, \tilde{g}(\theta)) = 0$, from the definition of g, we have $g(\theta) \leq \tilde{g}(\theta) < +\infty$ for all $\theta \in \Theta$. By Proposition A.1, $h(\theta, g(\theta)) = 0$, so the uniqueness in Implicit Function Theorem tells us that $\forall \theta \in \Theta$, if $\lambda_0 - \eta < g(\theta) < \lambda_0 + \eta$, then $g(\theta) = \tilde{g}(\theta)$. Since $g(\theta) \leq \tilde{g}(\theta) < \lambda_0 + \eta$, it suffices to prove that $g(\theta) > \lambda_0 - \eta$.

Now we prove that there exists a neighborhood Θ' of θ_0 such that $\forall \theta \in \Theta'$, $\forall \lambda \in [0, \lambda_0 - \eta]$, $h(\theta, \lambda) > 0$ (this would imply that $\forall \theta \in \Theta', g(\theta) > \lambda_0 - \eta$, since $h(\theta, g(\theta)) = 0$ by Proposition A.1). To prove that, we first note that $\forall \lambda \in [0, \lambda_0 - \eta]$, $h(\theta_0, \lambda) > 0$ since $g(\theta_0) = \lambda_0 > \lambda_0 - \eta$. Since $h(\theta_0, \lambda)$ is continuous w.r.t. λ, by the Extreme Value Theorem, $h(\theta_0, \lambda)$ on $\lambda \in [0, \lambda_0 - \eta]$ could attain the minimum $h(\theta_0, \lambda^*)$ which is positive, so there exists $\epsilon > 0$ such that $\forall \lambda \in [0, \lambda_0 - \eta], h(\theta_0, \lambda) \geq \epsilon$. We pick a bounded closed neighborhood of θ_0, denoted by Θ'' such that $\mathbf{0} \notin \Theta''$. h is continuous on the compact set $\{(\theta, \lambda) : \theta \in \Theta'', \lambda \in [0, \lambda_0 - \eta]\}$, so by Heine-Cantor Theorem, h is uniformly continuous on the same set. This implies that there exists $\delta > 0$ such that for all $\theta \in \Theta''$ satisfying $\|\theta - \theta_0\| < \delta$, we have $|h(\theta, \lambda) - h(\theta_0, \lambda)| < \epsilon$ and hence $h(\theta, \lambda) > 0$ for all $\lambda \in [0, \lambda_0 - \eta]$. Setting $\Theta' = \Theta'' \cap \{\theta : \|\theta - \theta_0\| < \delta\}$, we have $\forall \theta \in \Theta', \forall \lambda \in [0, \lambda_0 - \eta], h(\theta, \lambda) > 0$, and thus the proposition at the beginning of this paragraph is proven, i.e., $\forall \theta \in \Theta', g(\theta) > \lambda_0 - \eta$.

Therefore, we have proven that there exists a neighborhood of θ_0, $\Theta \cap \Theta'$, in which g and $\tilde{g}$ are equal. Since the differentiability at θ_0 and the gradient only rely on the function value in a neighborhood of θ_0, g is differentiable at θ_0 and $\nabla g(\theta_0) = \nabla \tilde{g}(\theta_0)$. By Eq. (21), the proof is completed. □

B Acquisition of Transfer-based Priors in Targeted Attacks

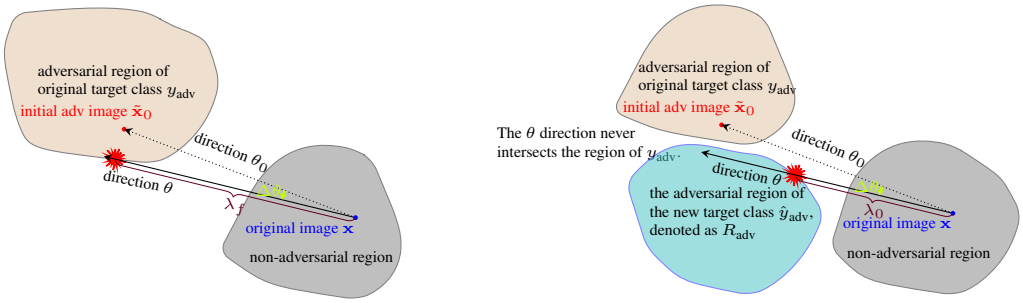

(a) The θ direction in the target model f.

(b) The θ direction in the surrogate model $\hat{f}$.

Figure 6: Illustration of setting the new target class $\hat{y}_{\text{adv}}$ and λ_0 before obtaining priors.

In targeted attacks, obtaining transfer-based priors is more challenging. Fig. 6 illustrates that θ_0 is initialized as the direction from the original image $\mathbf{x}$ to an initial adversarial image $\tilde{\mathbf{x}}_0$, which is selected from the target class y_{adv}. The θ_0 direction is used as the initial direction in both the surrogate model and the target model. If both models classify $\tilde{\mathbf{x}}_0$ correctly, the θ_0 direction leads to the region of the target class y_{adv} in both models. During the optimization process, a small perturbation $\Delta\theta$ is added to θ_0, resulting in a new direction θ. Although the θ direction may successfully guide the attack towards the adversarial region of the target class y_{adv} in the target model f, it may not lead to the same region in the surrogate model $\hat{f}$. This is a result of the varying decision boundaries between the two models, which differ in both shape and extent. Therefore, $g_{\hat{f}}(\theta)$ becomes infinitely large in

this case, as shown in Fig. 6b. To address this issue, we set a new target class $\hat{y}_{\text{adv}}$ and λ_0 before computing the transfer-based priors. The procedure is as follows:

(1) Starting at the original image $\mathbf{x}$, we move along the θ direction in the surrogate model $\hat{f}$. The region located at a distance of $\lambda_f + 1$ along θ is defined as the new adversarial region R_{adv} with label $\hat{y}_{\text{adv}}$, where λ_f represents the shortest distance from $\mathbf{x}$ along θ to the adversarial region of the original target class y_{adv} in the target model f. The shortest distance from $\mathbf{x}$ to R_{adv} along the θ direction is denoted as λ_0, as shown in Fig. 6b.

(2) If no adversarial region with the label $\hat{y}_{\text{adv}}$ different from the true label y is found in the previous steps, we then search for the first adversarial region R_{adv} along the θ direction in the surrogate model $\hat{f}$, within a distance range of 0 to 200. The label of R_{adv} is denoted as $\hat{y}_{\text{adv}}$, and the shortest distance from $\mathbf{x}$ to R_{adv} along the θ direction is denoted as λ_0.

C Theoretical Analysis of Sign-OPT, Prior-Sign-OPT, and Prior-OPT

Lemma C.1. *Suppose $\mathbf{u} \sim \mathcal{U}(\mathbb{S}_{d-1})$ where $\mathcal{U}(\mathbb{S}_{d-1})$ denotes the uniform distribution on the unit hypersphere in $\mathbb{R}^d$. Suppose $\mathbf{g}$ is a fixed vector in $\mathbb{R}^d$ with $\|\mathbf{g}\| = 1$. Let $\beta := \mathbf{u}^\top \mathbf{g}$. Then*

$$\mathbb{E}[|\beta|] = \frac{\Gamma(\frac{d}{2})}{\Gamma(\frac{d+1}{2})\sqrt{\pi}}, \tag{22}$$

$$\mathbb{E}[\beta^2] = \frac{1}{d}, \tag{23}$$

where Γ is the gamma function.

Proof. Let $\mathbf{a} \sim \mathcal{N}(\mathbf{0}, \mathbf{I}) \in \mathbb{R}^d$, then we let $\mathbf{u} = \frac{\mathbf{a}}{\|\mathbf{a}\|}$. Hence $\beta = \frac{\mathbf{a}^\top \mathbf{g}}{\|\mathbf{a}\|}$. Note that $\frac{\mathbf{a}}{\|\mathbf{a}\|}$ and $\|\mathbf{a}\|$ are independent because the distribution of $\frac{\mathbf{a}}{\|\mathbf{a}\|}$ is always the uniform distribution on the unit hypersphere given any restriction to the value of $\|\mathbf{a}\|$. Therefore, $\beta = \frac{\mathbf{a}^\top \mathbf{g}}{\|\mathbf{a}\|}$ and $\|\mathbf{a}\|$ are also independent, so $|\beta|$ and $\|\mathbf{a}\|$ are independent. Noting that $|\beta|\|\mathbf{a}\| = |\mathbf{a}^\top \mathbf{g}|$, we have

$$\mathbb{E}[|\mathbf{a}^\top \mathbf{g}|] = \mathbb{E}[|\beta|]\mathbb{E}[\|\mathbf{a}\|]. \tag{24}$$

Since $\mathbf{a}^\top \mathbf{g}$ is a affine transformation of the multivariate Gaussian variable $\mathbf{a}$, $\mathbf{a}^\top \mathbf{g}$ also has a Gaussian distribution with the mean 0 and the variance $\mathbf{g}^\top \mathbf{I} \mathbf{g} = 1$, so $\mathbf{a}^\top \mathbf{g} \sim \mathcal{N}(0, 1)$. Therefore, $|\mathbf{a}^\top \mathbf{g}|$ follows the folded normal distribution (actually its special case: the half-normal distribution), and by the formula in Tsagris et al. (2014),

$$\mathbb{E}[|\mathbf{a}^\top \mathbf{g}|] = \frac{\sqrt{2}}{\sqrt{\pi}}. \tag{25}$$

$\|\mathbf{a}\|$ follows the chi distribution with d degrees of freedom, so by the formula of its mean

$$\mathbb{E}[\|\mathbf{a}\|] = \sqrt{2}\frac{\Gamma(\frac{d+1}{2})}{\Gamma(\frac{d}{2})}. \tag{26}$$

Substituting Eq. (25) and Eq. (26) into Eq. (24), we have proved Eq. (22).

Since β and $\|\mathbf{a}\|$ are independent, similarly to Eq. (24), we have

$$\mathbb{E}[(\mathbf{a}^\top \mathbf{g})^2] = \mathbb{E}[\beta^2]\mathbb{E}[\|\mathbf{a}\|^2]. \tag{27}$$

Since $\mathbf{a} \sim \mathcal{N}(\mathbf{0}, \mathbf{I})$, $\mathbb{E}[\mathbf{a}\mathbf{a}^\top] = \mathbf{I}$. Hence $\mathbb{E}[(\mathbf{a}^\top \mathbf{g})^2] = \mathbb{E}[\mathbf{g}^\top \mathbf{a} \cdot \mathbf{a}^\top \mathbf{g}] = \mathbf{g}^\top \mathbb{E}[\mathbf{a}\mathbf{a}^\top]\mathbf{g} = \|\mathbf{g}\|^2 = 1$, and $\mathbb{E}[\|\mathbf{a}\|^2] = \mathbb{E}[\text{Tr}(\mathbf{a}\mathbf{a}^\top)] = \text{Tr}(\mathbb{E}[\mathbf{a}\mathbf{a}^\top]) = d$. By Eq. (27), Eq. (23) has been proved.

□

Lemma C.2. *Suppose $\mathbf{g}$ is a fixed vector in $\mathbb{R}^d$ with $\|\mathbf{g}\| = 1$. Suppose $\mathbf{p}$ is another fixed vector in $\mathbb{R}^d$ with $\|\mathbf{p}\| = 1$, and let $\beta_p := \mathbf{g}^\top \mathbf{p}$. Let $\mathbf{u}$ be a random vector uniformly sampled from the unit*

hypersphere in the $(d-1)$*-dimensional subspace orthogonal to* $\mathbf{p}$*. Specifically,* $\mathbf{u}$ *can be constructed as* $\mathbf{u} = \overline{\boldsymbol{\xi} - \boldsymbol{\xi}^\top \mathbf{p} \cdot \mathbf{p}}$ *where* $\boldsymbol{\xi} \sim \mathcal{U}(\mathbb{S}_{d-1})$*. Let* $\beta_\perp \coloneqq \mathbf{g}^\top \mathbf{u}$*, then*

$$\mathbb{E}[|\beta_\perp|] = \frac{\Gamma(\frac{d-1}{2})}{\Gamma(\frac{d}{2})\sqrt{\pi}} \sqrt{1-\beta_p^2}. \tag{28}$$

Proof. To observe the property of $\beta_\perp$, since $\mathbf{u}$ is orthogonal to $\mathbf{p}$, we do the following decomposition for $\mathbf{g}$:

$$\mathbf{g} = \mathbf{g}^\top \mathbf{p} \cdot \mathbf{p} + \mathbf{g}_\perp = \beta_p \mathbf{p} + \mathbf{g}_\perp, \tag{29}$$

where $\mathbf{g}_\perp \coloneqq \mathbf{g} - \mathbf{g}^\top \mathbf{p} \cdot \mathbf{p}$ denotes the projection of $\mathbf{g}$ to the $(d-1)$-dimensional subspace orthogonal to $\mathbf{p}$. By expanding the inner product, we have

$$\|\mathbf{g}_\perp\|^2 = 1 - 2\beta_p^2 + \beta_p^2 = 1 - \beta_p^2, \tag{30}$$

so $\|\mathbf{g}_\perp\| = \sqrt{1-\beta_p^2}$. Meanwhile,

$$\beta_\perp = \mathbf{g}^\top \mathbf{u} = (\mathbf{g}^\top \mathbf{p} \cdot \mathbf{p} + \mathbf{g}_\perp)^\top \mathbf{u} = \mathbf{g}_\perp^\top \mathbf{u}. \tag{31}$$

Therefore, $\beta_\perp$ is essentially the inner product between a random vector uniformly sampled from the unit hypersphere in a $(d-1)$-dimensional subspace and a fixed vector with norm $\sqrt{1-\beta_p^2}$ in this subspace. Taking the expectation of the absolute values on both sides of Eq. (31), we have

$$\mathbb{E}[|\beta_\perp|] = \mathbb{E}[|\mathbf{g}_\perp^\top \mathbf{u}|] = \|\mathbf{g}_\perp\| \mathbb{E}[|\overline{\mathbf{g}_\perp}^\top \mathbf{u}|]. \tag{32}$$

Since both $\overline{\mathbf{g}_\perp}$ and $\mathbf{u}$ reside in the $(d-1)$-dimensional subspace orthogonal to $\mathbf{p}$, it follows that $\mathbb{E}[|\overline{\mathbf{g}_\perp}^\top \mathbf{u}|]$ corresponds to $\mathbb{E}[|\beta|]$ in Eq. (22), with d replaced by $d-1$. Therefore,

$$\mathbb{E}[|\beta_\perp|] = \|\mathbf{g}_\perp\| \mathbb{E}[|\overline{\mathbf{g}_\perp}^\top \mathbf{u}|] = \frac{\Gamma(\frac{d-1}{2})}{\Gamma(\frac{d}{2})\sqrt{\pi}} \sqrt{1-\beta_p^2}, \tag{33}$$

and the proof is completed. □

Lemma C.3. *Let* β *be as defined in Lemma C.1, then the probability density function of* β *is (note that* $-1 \le \beta \le 1$*)*

$$p(\beta) = \frac{\left(\sqrt{1-\beta^2}\right)^{d-3}}{\mathrm{B}\left(\frac{d-1}{2}, \frac{1}{2}\right)}, \tag{34}$$

where $\mathrm{B}(\cdot,\cdot)$ *is the beta function.*

Proof. We note that when $-1 \le x \le 0$, $P(\beta \le x)$ is equal to the ratio of the surface area of the hyperspherical cap of a hypersphere in $\mathbb{R}^d$ to the surface area of the hypersphere. For a hyperspherical cap with height h on a unit hypersphere, its surface area is $\frac{1}{2} A_d I_{2h-h^2}\left(\frac{d-1}{2}, \frac{1}{2}\right)$, where A_d is the surface area of the unit hypersphere in $\mathbb{R}^d$ and $I(\cdot,\cdot)$ is the regularized incomplete beta function. To compute $P(\beta \le x)$ for $-1 \le x \le 0$, substituting $h = x+1$ and dividing the area by A_d, we have

$$P(\beta \le x) = \frac{1}{2} I_{1-x^2}\left(\frac{d-1}{2}, \frac{1}{2}\right), \tag{35}$$

where I is the regularized incomplete beta function, defined as

$$I_x(a,b) = \frac{\int_0^x t^{a-1}(1-t)^{b-1}\mathrm{d}t}{\mathrm{B}(a,b)}. \tag{36}$$

Hence the probability density function is

$$\begin{aligned}
p_\beta(x) &= \frac{\partial}{\partial x} P(\beta \le x) && (37)\\
&= \frac{1}{2} \cdot \frac{-2x}{\mathrm{B}\left(\frac{d-1}{2}, \frac{1}{2}\right)} \left(1-x^2\right)^{\frac{d-1}{2}-1} \left(1-(1-x^2)\right)^{\frac{1}{2}-1} && (38)\\
&= \frac{-x}{|x|} \cdot \frac{\left(\sqrt{1-x^2}\right)^{d-3}}{\mathrm{B}\left(\frac{d-1}{2}, \frac{1}{2}\right)} && (39)\\
&= \frac{\left(\sqrt{1-x^2}\right)^{d-3}}{\mathrm{B}\left(\frac{d-1}{2}, \frac{1}{2}\right)}. && (40)
\end{aligned}$$

Note that the last equality holds because $x \leq 0$.

Therefore, we have proven Eq. (34) for $\beta \leq 0$. When $\beta > 0$, the formula is the same due to the symmetry. The proof is completed. □

C.1 Analysis for Sign-OPT

We can compute the projection of $\nabla g(\theta)$ onto S with $s = 0$ by summing over all its projection onto the orthonormal basis:

$$\mathbf{v} := \sum_{i=1}^{q} \frac{g(\theta + \sigma \mathbf{u}_i) - g(\theta)}{\sigma} \cdot \mathbf{u}_i, \tag{41}$$

where $\{\mathbf{u}_1, \ldots, \mathbf{u}_q\}$ is a uniformly random orthonormal set of q vectors in $\mathbb{R}^d$, so $\mathbf{u}_i \sim \mathcal{U}(\mathbb{S}_{d-1})$ for any $i \leq q$. However, in hard-label attacks the coefficients above for each basis vector are costly to estimate. In the Sign-OPT estimator, each coefficient is replaced by its sign which is much easier to obtain using hard-label queries:

$$\mathbf{v} = \sum_{i=1}^{q} \text{sign}(g(\theta + \sigma \mathbf{u}_i) - g(\theta)) \cdot \mathbf{u}_i. \tag{42}$$

In the following analysis, we assume that g is differentiable at θ so that we have $g(\theta + \sigma \mathbf{u}) - g(\theta) = \sigma \cdot \nabla g(\theta)^\top \mathbf{u} + o(\sigma)$ where $\lim_{\sigma \to 0} \frac{o(\sigma)}{\sigma} = 0$ for any unit vector $\mathbf{u}$. We further assume that σ is sufficiently small so that we can omit $o(\sigma)$. In practice, if the target model is deterministic, picking a small σ is feasible until the numerical error dominates. Therefore, in the following analysis we assume that

$$\text{sign}(g(\theta + \sigma \mathbf{u}) - g(\theta)) \approx \text{sign}(\nabla g(\theta)^\top \mathbf{u}), \tag{43}$$

where $\mathbf{u}$ is a unit vector in $\mathbb{R}^d$. Now we can write Sign-OPT in the following form:

$$\mathbf{v} = \sum_{i=1}^{q} \text{sign}(\nabla g(\theta)^\top \mathbf{u}_i) \cdot \mathbf{u}_i. \tag{44}$$

Now, we present the proof of Theorem 3.2 for the Sign-OPT estimator defined in Eq. (44).

Proof. Since $\{\mathbf{u}_i\}_{i=1}^q$ are orthonormal, we have $\|\mathbf{v}\| = \sqrt{\sum_{i=1}^q (\text{sign}(\nabla g(\theta)^\top \mathbf{u}_i))^2} = \sqrt{q}$. We note that $\text{sign}(\nabla g(\theta)^\top \mathbf{u}_i) = \text{sign}(\overline{\nabla g(\theta)}^\top \mathbf{u}_i)$, so

$$\mathbf{v} = \sum_{i=1}^{q} \text{sign}(\overline{\nabla g(\theta)}^\top \mathbf{u}_i) \cdot \mathbf{u}_i. \tag{45}$$

Hence

$$\gamma = \frac{\mathbf{v}^\top \overline{\nabla g(\theta)}}{\|\mathbf{v}\|} = \frac{1}{\sqrt{q}} \sum_{i=1}^{q} \text{sign}(\overline{\nabla g(\theta)}^\top \mathbf{u}_i) \cdot (\overline{\nabla g(\theta)}^\top \mathbf{u}_i) \tag{46}$$

$$= \frac{1}{\sqrt{q}} \sum_{i=1}^{q} \left| \overline{\nabla g(\theta)}^\top \mathbf{u}_i \right|. \tag{47}$$

Since $\nabla g(\theta)$ is a fixed vector w.r.t. the randomness of $\{\mathbf{u}_i\}_{i=1}^q$, and the marginal distribution of $\mathbf{u}_i$ is $\mathcal{U}(\mathbb{S}_{d-1})$ for any i, by Eq. (22) we have

$$\mathbb{E}[\gamma] = \frac{1}{\sqrt{q}} q \frac{\Gamma(\frac{d}{2})}{\Gamma(\frac{d+1}{2})\sqrt{\pi}} = \sqrt{q} \frac{\Gamma(\frac{d}{2})}{\Gamma(\frac{d+1}{2})\sqrt{\pi}}. \tag{48}$$

Computing $\mathbb{E}[\gamma^2]$ is more complicated. First we have

$$\gamma^2 = \frac{1}{q} \left(\sum_{i=1}^{q} \left| \overline{\nabla g(\theta)}^\top \mathbf{u}_i \right| \right)^2 \tag{49}$$

$$= \frac{1}{q} \sum_{i=1}^{q} \left(\overline{\nabla g(\theta)}^\top \mathbf{u}_i \right)^2 + \frac{1}{q} \sum_{i \neq j} \left| \overline{\nabla g(\theta)}^\top \mathbf{u}_i \right| \cdot \left| \overline{\nabla g(\theta)}^\top \mathbf{u}_j \right|. \tag{50}$$

For the first part, by Eq. (23) we have

$$\forall i, \mathbb{E}[(\overline{\nabla g(\theta)}^\top \mathbf{u}_i)^2] = \frac{1}{d}. \tag{51}$$

For the second part, let us denote $\beta_i \coloneqq \overline{\nabla g(\theta)}^\top \mathbf{u}_i$ and $\beta_j \coloneqq \overline{\nabla g(\theta)}^\top \mathbf{u}_j$. Then we need to compute for $i \neq j$:

$$\mathbb{E}[|\beta_i| \cdot |\beta_j|] = \mathbb{E}_{\mathbf{u}_i}[\mathbb{E}[(|\beta_i| \cdot |\beta_j|)\big|\mathbf{u}_i]] \tag{52}$$

$$= \mathbb{E}_{\mathbf{u}_i}[|\beta_i|\mathbb{E}[|\beta_j|\big|\mathbf{u}_i]]. \tag{53}$$

Next, we aim to compute $\mathbb{E}[|\beta_j|\big|\mathbf{u}_i]$. Since $\mathbf{u}_i$ and $\mathbf{u}_j$ are orthonormal, conditioned on $\mathbf{u}_i$, the vector $\mathbf{u}_j$ is uniformly distributed on the unit hypersphere in the $(d-1)$-dimensional subspace orthogonal to $\mathbf{u}_i$. When calculating the conditional expectation, we consider $\mathbf{u}_i$ to be fixed and use Lemma C.2. Specifically, in Lemma C.2 we let $\mathbf{g}$ be $\overline{\nabla g(\theta)}$ and let $\mathbf{p}$ be $\mathbf{u}_i$. Then we have

$$\mathbb{E}[|\beta_j|\big|\mathbf{u}_i] = \frac{\Gamma(\frac{d-1}{2})}{\Gamma(\frac{d}{2})\sqrt{\pi}}\sqrt{1-\beta_i^2}. \tag{54}$$

Substituting Eq. (54) into Eq. (53), we have

$$\mathbb{E}[|\beta_i| \cdot |\beta_j|] = \frac{\Gamma(\frac{d-1}{2})}{\Gamma(\frac{d}{2})\sqrt{\pi}}\mathbb{E}\left[|\beta_i|\sqrt{1-\beta_i^2}\right]. \tag{55}$$

Here the distribution of β_i is the same as that of β in Lemma C.1, and we need to compute $\mathbb{E}[|\beta|\sqrt{1-\beta^2}]$. By Eq. (22) and Eq. (34), we have

$$\frac{\Gamma(\frac{d}{2})}{\Gamma(\frac{d+1}{2})\sqrt{\pi}} = \mathbb{E}[|\beta|] = \int_{-1}^{1} p(\beta)|\beta|\mathrm{d}\beta \tag{56}$$

$$= \int_{-1}^{1} |\beta| \frac{\left(\sqrt{1-\beta^2}\right)^{d-3}}{\mathrm{B}\left(\frac{d-1}{2}, \frac{1}{2}\right)}\mathrm{d}\beta, \tag{57}$$

so

$$\int_{-1}^{1} |\beta| \left(\sqrt{1-\beta^2}\right)^{d-3} \mathrm{d}\beta = \frac{\Gamma(\frac{d}{2})}{\Gamma(\frac{d+1}{2})\sqrt{\pi}}\mathrm{B}\left(\frac{d-1}{2}, \frac{1}{2}\right). \tag{58}$$

Hence

$$\mathbb{E}\left[|\beta|\sqrt{1-\beta^2}\right] = \int_{-1}^{1} |\beta|\sqrt{1-\beta^2}p(\beta)\mathrm{d}\beta \tag{59}$$

$$= \frac{1}{\mathrm{B}\left(\frac{d-1}{2}, \frac{1}{2}\right)} \int_{-1}^{1} |\beta| \left(\sqrt{1-\beta^2}\right)^{d-2} \mathrm{d}\beta \tag{60}$$

$$= \frac{1}{\mathrm{B}\left(\frac{d-1}{2}, \frac{1}{2}\right)} \frac{\Gamma(\frac{d+1}{2})}{\Gamma(\frac{d+2}{2})\sqrt{\pi}}\mathrm{B}\left(\frac{d}{2}, \frac{1}{2}\right), \tag{61}$$

where the last equality is obtained by setting d in Eq. (58) to $d+1$. Therefore, by Eq. (55) we have

$$\mathbb{E}[|\beta_i| \cdot |\beta_j|] = \frac{1}{\pi}\frac{\mathrm{B}\left(\frac{d}{2}, \frac{1}{2}\right)}{\mathrm{B}\left(\frac{d-1}{2}, \frac{1}{2}\right)}\frac{\Gamma(\frac{d-1}{2})}{\Gamma(\frac{d}{2})}\frac{\Gamma(\frac{d+1}{2})}{\Gamma(\frac{d+2}{2})} \tag{62}$$

$$= \frac{1}{\pi}\frac{\Gamma(\frac{d}{2})\Gamma(\frac{d}{2})}{\Gamma(\frac{d+1}{2})\Gamma(\frac{d-1}{2})}\frac{\Gamma(\frac{d-1}{2})}{\Gamma(\frac{d}{2})}\frac{\Gamma(\frac{d+1}{2})}{\Gamma(\frac{d+2}{2})} \tag{63}$$

$$= \frac{1}{\pi}\frac{\Gamma(\frac{d}{2})}{\Gamma(\frac{d+2}{2})} \tag{64}$$

$$= \frac{2}{\pi d}. \tag{65}$$

Here, the second equality is due to the identity $\mathrm{B}(a,b) = \frac{\Gamma(a)\Gamma(b)}{\Gamma(a+b)}$, and the last equality is due to the identity $\Gamma(a+1) = a\Gamma(a)$.

Taking the expectation on both sides of Eq. (50) and using Eq. (51) and Eq. (65), we have

$$\mathbb{E}[\gamma^2] = \frac{1}{q} \cdot q \cdot \frac{1}{d} + \frac{1}{q} \cdot q(q-1) \cdot \frac{2}{\pi d} \tag{66}$$

$$= \frac{1}{d} + \frac{2(q-1)}{\pi d} = \frac{1}{d}\left(\frac{2}{\pi}(q-1)+1\right). \tag{67}$$

The proof is completed. □

C.2 Analysis for Prior-Sign-OPT

The Prior-Sign-OPT estimator is defined in Eq. (7). Note that there are s priors $\{\mathbf{p}_1, \ldots, \mathbf{p}_s\}$ (we assume that they are normalized to have unit norm), and $\{\mathbf{u}_1, \mathbf{u}_2, \ldots, \mathbf{u}_{q-s}\}$ is a uniformly random orthonormal set of $q-s$ vectors in the $(d-s)$-dimensional subspace orthogonal to $\{\mathbf{p}_1, \ldots, \mathbf{p}_s\}$. For convenience we first consider the case of $s = 1$, and the analysis can easily be generalized to the case of $s > 1$.

C.2.1 The Case of $s = 1$

When $s = 1$, we rewrite the Prior-Sign-OPT estimator in the following form:

$$\mathbf{v}^* = \mathrm{sign}(\nabla g(\theta)^\top \mathbf{p}) \cdot \mathbf{p} + \sum_{i=1}^{q-1} \mathrm{sign}(\nabla g(\theta)^\top \mathbf{u}_i) \cdot \mathbf{u}_i, \tag{68}$$

where $\mathbf{p}$ is the prior vector with $\|\mathbf{p}\| = 1$, and $\{\mathbf{u}_i\}_{i=1}^{q-1}$ is the random orthonormal basis of the $(d-1)$-dimensional subspace orthogonal to $\mathbf{p}$. Note that the directional derivative approximation is also employed, as in Eq. (43).

Theorem C.4. *For the Prior-Sign-OPT estimator defined in Eq.* (68)*, we let* $\gamma \coloneqq \overline{\mathbf{v}^*}^\top \overline{\nabla g(\theta)}$ *be its cosine similarity to the true gradient, where the notation* $\overline{\mathbf{v}^*} \coloneqq \frac{\mathbf{v}^*}{\|\mathbf{v}^*\|}$ *is defined to be the* ℓ_2 *normalization of the corresponding vector, then*

$$\mathbb{E}[\gamma] = \frac{1}{\sqrt{q}}\left[|\alpha| + (q-1)\sqrt{1-\alpha^2}\frac{\Gamma(\frac{d-1}{2})}{\Gamma(\frac{d}{2})\sqrt{\pi}}\right], \tag{69}$$

$$\mathbb{E}[\gamma^2] = \frac{1}{q}\left[\alpha^2 + \frac{q-1}{d-1}\left(\frac{2}{\pi}(q-2)+1\right)(1-\alpha^2) + 2|\alpha|(q-1)\sqrt{1-\alpha^2}\frac{\Gamma(\frac{d-1}{2})}{\Gamma(\frac{d}{2})\sqrt{\pi}}\right], \tag{70}$$

where $\alpha \coloneqq \mathbf{p}^\top \overline{\nabla g(\theta)}$ *is the cosine similarity between the prior and the true gradient.*

Proof. Note that the property of sign function (e.g., $\mathrm{sign}(\nabla g(\theta)^\top \mathbf{u}) = \mathrm{sign}(\overline{\nabla g(\theta)}^\top \mathbf{u})$), in Eq. (68), we denote

$$\mathbf{v}_\perp \coloneqq \sum_{i=1}^{q-1} \mathrm{sign}(\nabla g(\theta)^\top \mathbf{u}_i) \cdot \mathbf{u}_i = \sum_{i=1}^{q-1} \mathrm{sign}(\overline{\nabla g(\theta)}^\top \mathbf{u}_i) \cdot \mathbf{u}_i, \tag{71}$$

then $\mathbf{v}^* = \mathrm{sign}(\alpha)\mathbf{p} + \mathbf{v}_\perp$. Now

$$\gamma = \frac{(\mathbf{v}^*)^\top \overline{\nabla g(\theta)}}{\|\mathbf{v}^*\|} \tag{72}$$

$$= \frac{1}{\sqrt{q}}(|\alpha| + \mathbf{v}_\perp^\top \overline{\nabla g(\theta)}). \tag{73}$$

The following argument is similar to that in the proof of Lemma C.2. Let $\mathbf{g} \coloneqq \overline{\nabla g(\theta)}$, and let $\mathbf{g}_\perp \coloneqq \mathbf{g} - \mathbf{g}^\top \mathbf{p} \cdot \mathbf{p}$ denote the projection of $\mathbf{g}$ to the $(d-1)$-dimensional subspace orthogonal

to $\mathbf{p}$. It follows that $\mathbf{v}_\perp^\top \mathbf{g} = \mathbf{v}_\perp^\top \mathbf{g}_\perp$. Moreover, since $\{\mathbf{u}_i\}_{i=1}^{q-1}$ are orthogonal to $\mathbf{p}$, we have $\mathbf{v}_\perp = \sum_{i=1}^{q-1} \text{sign}(\mathbf{g}_\perp^\top \mathbf{u}_i) \cdot \mathbf{u}_i$. Since $\{\mathbf{u}_i\}_{i=1}^{q-1}$ are uniformly distributed on the unit hypersphere in the $(d-1)$-dimensional subspace orthogonal to $\mathbf{p}$, and $\mathbf{g}_\perp$ also resides in this subspace, $\mathbf{v}_\perp$ can be considered as the Sign-OPT estimator for $\mathbf{g}_\perp$ as in Eq. (44), with q replaced by $q-1$ and the effective dimension being $d-1$ rather than d. By Eq. (9) we have

$$\mathbb{E}[\overline{\mathbf{v}_\perp}^\top \overline{\mathbf{g}_\perp}] = \sqrt{q-1}\frac{\Gamma(\frac{d-1}{2})}{\Gamma(\frac{d}{2})\sqrt{\pi}}. \tag{74}$$

Noting that $\|\mathbf{g}_\perp\| = \sqrt{1-\alpha^2}$ by Eq. (30) and $\|\mathbf{v}_\perp\| = \sqrt{q-1}$, we have

$$\mathbb{E}[\mathbf{v}_\perp^\top \mathbf{g}] = \mathbb{E}[\mathbf{v}_\perp^\top \mathbf{g}_\perp] = \mathbb{E}[\overline{\mathbf{v}_\perp}^\top \overline{\mathbf{g}_\perp}\|\mathbf{v}_\perp\|\|\mathbf{g}_\perp\|] \tag{75}$$

$$= (q-1)\sqrt{1-\alpha^2}\frac{\Gamma(\frac{d-1}{2})}{\Gamma(\frac{d}{2})\sqrt{\pi}}. \tag{76}$$

Taking the expectation on both sides of Eq. (73) and substituting Eq. (76), Eq. (69) has been proved.

Next we derive $\mathbb{E}[\gamma^2]$. By Eq. (73) we have

$$\gamma^2 = \frac{1}{q}(|\alpha| + \mathbf{v}_\perp^\top \mathbf{g})^2 \tag{77}$$

$$= \frac{1}{q}(\alpha^2 + (\mathbf{v}_\perp^\top \mathbf{g})^2 + 2|\alpha|\mathbf{v}_\perp^\top \mathbf{g}). \tag{78}$$

As discussed in the paragraph preceding Eq. (74), $\mathbf{v}_\perp$ can be considered as the Sign-OPT estimator for $\mathbf{g}_\perp$ as in Eq. (44), with q replaced by $q-1$ and the effective dimension being $d-1$ rather than d. By Eq. (10) we have

$$\mathbb{E}[(\overline{\mathbf{v}_\perp}^\top \overline{\mathbf{g}_\perp})^2] = \frac{1}{d-1}\left(\frac{2}{\pi}(q-2)+1\right). \tag{79}$$

Noting that $\|\mathbf{g}_\perp\| = \sqrt{1-\alpha^2}$ by Eq. (30) and $\|\mathbf{v}_\perp\| = \sqrt{q-1}$, we have

$$\mathbb{E}[(\mathbf{v}_\perp^\top \mathbf{g})^2] = \mathbb{E}[(\mathbf{v}_\perp^\top \mathbf{g}_\perp)^2] = \mathbb{E}[(\overline{\mathbf{v}_\perp}^\top \overline{\mathbf{g}_\perp})^2\|\mathbf{v}_\perp\|^2\|\mathbf{g}_\perp\|^2] \tag{80}$$

$$= \frac{q-1}{d-1}\left(\frac{2}{\pi}(q-2)+1\right)(1-\alpha^2). \tag{81}$$

Taking the expectation on both sides of Eq. (78) and substituting Eq. (76) and Eq. (81), Eq. (70) has been proved. □

C.2.2 THE CASE OF $s > 1$

In the case of $s > 1$, we rewrite the Prior-Sign-OPT estimator in the following form:

$$\mathbf{v}^* = \sum_{i=1}^{s} \text{sign}(\nabla g(\theta)^\top \mathbf{p}_i) \cdot \mathbf{p}_i + \sum_{i=1}^{q-s} \text{sign}(\nabla g(\theta)^\top \mathbf{u}_i) \cdot \mathbf{u}_i. \tag{82}$$

Now, we present the proof of Theorem 3.3 for the Prior-Sign-OPT estimator defined in Eq. (82).

Proof. The following argument is similar to that in the proof of Theorem C.4. Now we have

$$\mathbf{v}_\perp \coloneqq \sum_{i=1}^{q-s} \text{sign}(\nabla g(\theta)^\top \mathbf{u}_i) \cdot \mathbf{u}_i = \sum_{i=1}^{q-s} \text{sign}(\overline{\nabla g(\theta)}^\top \mathbf{u}_i) \cdot \mathbf{u}_i, \tag{83}$$

then $\mathbf{v}^* = \sum_{i=1}^{s} \text{sign}(\alpha_i)\mathbf{p}_i + \mathbf{v}_\perp$, and

$$\gamma = \frac{(\mathbf{v}^*)^\top \overline{\nabla g(\theta)}}{\|\mathbf{v}^*\|} \tag{84}$$

$$= \frac{1}{\sqrt{q}}\left(\sum_{i=1}^{s} |\alpha_i| + \mathbf{v}_\perp^\top \overline{\nabla g(\theta)}\right). \tag{85}$$

Let $\mathbf{g} \coloneqq \overline{\nabla g(\theta)}$, and let $\mathbf{g}_\perp \coloneqq \mathbf{g} - \sum_{i=1}^{s} \mathbf{g}^\top \mathbf{p}_i \cdot \mathbf{p}_i$ denote the projection of $\mathbf{g}$ to the $(d-s)$-dimensional subspace orthogonal to $\{\mathbf{p}_i\}_{i=1}^{s}$. It follows that $\mathbf{v}_\perp^\top \mathbf{g} = \mathbf{v}_\perp^\top \mathbf{g}_\perp$. Using the similar analysis to that in the case of $s = 1$, when $s > 1$ we have

$$\mathbb{E}[\overline{\mathbf{v}_\perp}^\top \overline{\mathbf{g}_\perp}] = \sqrt{q-s}\frac{\Gamma(\frac{d-s}{2})}{\Gamma(\frac{d-s+1}{2})\sqrt{\pi}}. \tag{86}$$

Similar to the derivation of Eq. (30), we can derive that $\|\mathbf{g}_\perp\| = \sqrt{1 - \sum_{i=1}^{s} \alpha_i^2}$. Since $\|\mathbf{v}_\perp\| = \sqrt{q-s}$, we have

$$\mathbb{E}[\mathbf{v}_\perp^\top \mathbf{g}] = \mathbb{E}[\mathbf{v}_\perp^\top \mathbf{g}_\perp] = \mathbb{E}[\overline{\mathbf{v}_\perp}^\top \overline{\mathbf{g}_\perp} \|\mathbf{v}_\perp\| \|\mathbf{g}_\perp\|] \tag{87}$$

$$= (q-s)\sqrt{1 - \sum_{i=1}^{s} \alpha_i^2}\frac{\Gamma(\frac{d-s}{2})}{\Gamma(\frac{d-s+1}{2})\sqrt{\pi}}. \tag{88}$$

Taking the expectation on both sides of Eq. (85) and substituting Eq. (88), Eq. (11) has been proved.

Next we derive $\mathbb{E}[\gamma^2]$. By Eq. (85) we have

$$\gamma^2 = \frac{1}{q}\left(\sum_{i=1}^{s} |\alpha_i| + \mathbf{v}_\perp^\top \mathbf{g}\right)^2 \tag{89}$$

$$= \frac{1}{q}\left(\left(\sum_{i=1}^{s} |\alpha_i|\right)^2 + \left(\mathbf{v}_\perp^\top \mathbf{g}\right)^2 + 2 \cdot \left(\sum_{i=1}^{s} |\alpha_i|\right) \cdot \mathbf{v}_\perp^\top \mathbf{g}\right). \tag{90}$$

Similar to the case of $s = 1$, when $s > 1$ we have

$$\mathbb{E}[(\overline{\mathbf{v}_\perp}^\top \overline{\mathbf{g}_\perp})^2] = \frac{1}{d-s}\left(\frac{2}{\pi}(q-s-1)+1\right). \tag{91}$$

Noting that $\|\mathbf{g}_\perp\| = \sqrt{1 - \sum_{i=1}^{s} \alpha_i^2}$ and $\|\mathbf{v}_\perp\| = \sqrt{q-s}$, we have

$$\mathbb{E}[(\mathbf{v}_\perp^\top \mathbf{g})^2] = \mathbb{E}[(\mathbf{v}_\perp^\top \mathbf{g}_\perp)^2] = \mathbb{E}[(\overline{\mathbf{v}_\perp}^\top \overline{\mathbf{g}_\perp})^2 \|\mathbf{v}_\perp\|^2 \|\mathbf{g}_\perp\|^2] \tag{92}$$

$$= \frac{q-s}{d-s}\left(\frac{2}{\pi}(q-s-1)+1\right)\left(1 - \sum_{i=1}^{s} \alpha_i^2\right). \tag{93}$$

Taking the expectation on both sides of Eq. (90) and substituting Eq. (88) and Eq. (93), Eq. (12) has been proved. □

C.3 Analysis for Prior-OPT

The Prior-OPT estimator is defined in Eq. (13). Note that there are s priors $\{\mathbf{p}_1, \ldots, \mathbf{p}_s\}$ (we assume that they have been normalized so that they have unit norm), and $\{\mathbf{u}_1, \mathbf{u}_2, \ldots, \mathbf{u}_{q-s}\}$ is a uniformly random orthonormal set of $q-s$ vectors in the $(d-s)$-dimensional subspace orthogonal to $\{\mathbf{p}_1, \ldots, \mathbf{p}_s\}$. For convenience, we first consider the case of $s = 1$, and the analysis can easily be generalized to the case of $s > 1$.

C.3.1 The Case of $s = 1$

When $s = 1$, we rewrite the Prior-OPT estimator in the following form:

$$\mathbf{v}^* = \nabla g(\theta)^\top \mathbf{p} \cdot \mathbf{p} + \nabla g(\theta)^\top \overline{\mathbf{v}_\perp} \cdot \overline{\mathbf{v}_\perp}, \tag{94}$$

where

$$\mathbf{v}_\perp \coloneqq \sum_{i=1}^{q-1} \text{sign}(\nabla g(\theta)^\top \mathbf{u}_i) \cdot \mathbf{u}_i. \tag{95}$$

Here $\mathbf{p}$ is the prior vector with $\|\mathbf{p}\| = 1$, and $\{\mathbf{u}_i\}_{i=1}^{q-1}$ is the random orthonormal basis of the $(d-1)$-dimensional subspace orthogonal to $\mathbf{p}$. Note that we employ the directional derivative approximation as in Eq. (43). Furthermore, it should also be noted that $\mathbf{v}_\perp$ defined in Eq. (95) is consistent with that in Eq. (71), and thus the conclusions regarding $\mathbf{v}_\perp$ derived in Appendix C.2.1 remain valid in this section (e.g., Eq. (76)).

Theorem C.5. *For the Prior-OPT estimator defined in Eq.* (94)*, we let* $\gamma \coloneqq \overline{\mathbf{v}^*}^\top \overline{\nabla g(\theta)}$ *be its cosine similarity to the true gradient, where the notation* $\overline{\mathbf{v}^*} \coloneqq \frac{\mathbf{v}^*}{\|\mathbf{v}^*\|}$ *is defined to be the* ℓ_2 *normalization of the corresponding vector, then*

$$\mathbb{E}[\gamma] \geq \sqrt{\alpha^2 + \frac{(q-1)(1-\alpha^2)}{\pi}\left(\frac{\Gamma(\frac{d-1}{2})}{\Gamma(\frac{d}{2})}\right)^2}, \tag{96}$$

$$\mathbb{E}[\gamma] \leq \sqrt{\alpha^2 + \frac{1}{d-1}\left(\frac{2}{\pi}(q-2)+1\right)(1-\alpha^2)}, \tag{97}$$

$$\mathbb{E}[\gamma^2] = \alpha^2 + \frac{1}{d-1}\left(\frac{2}{\pi}(q-2)+1\right)(1-\alpha^2), \tag{98}$$

where $\alpha \coloneqq \mathbf{p}^\top \overline{\nabla g(\theta)}$ *is the cosine similarity between the prior and the true gradient.*

Proof. Let $\mathbf{g} \coloneqq \overline{\nabla g(\theta)}$. Then $\mathbf{v}^* = \|\nabla g(\theta)\|(\mathbf{g}^\top \mathbf{p} \cdot \mathbf{p} + \mathbf{g}^\top \overline{\mathbf{v}_\perp} \cdot \overline{\mathbf{v}_\perp})$. We also note that $\mathbf{v}_\perp$ is a linear combination of $\mathbf{u}_1$ to $\mathbf{u}_{q-1}$, all of which are orthogonal to $\mathbf{p}$, so $\mathbf{v}_\perp$ is also orthogonal to $\mathbf{p}$. Therefore, $\|\mathbf{v}^*\| = \|\nabla g(\theta)\|\sqrt{(\mathbf{p}^\top \mathbf{g})^2 + (\overline{\mathbf{v}_\perp}^\top \mathbf{g})^2}$. Hence

$$\gamma = \frac{(\mathbf{v}^*)^\top \overline{\nabla g(\theta)}}{\|\mathbf{v}^*\|} \tag{99}$$

$$= \frac{(\mathbf{p}^\top \mathbf{g})^2 + (\overline{\mathbf{v}_\perp}^\top \mathbf{g})^2}{\sqrt{(\mathbf{p}^\top \mathbf{g})^2 + (\overline{\mathbf{v}_\perp}^\top \mathbf{g})^2}} \tag{100}$$

$$= \sqrt{(\mathbf{p}^\top \mathbf{g})^2 + (\overline{\mathbf{v}_\perp}^\top \mathbf{g})^2}. \tag{101}$$

We define a new estimator

$$\widetilde{\mathbf{v}^*} \coloneqq \nabla g(\theta)^\top \mathbf{p} \cdot \mathbf{p} + \mathbb{E}[\overline{\mathbf{v}_\perp}^\top \nabla g(\theta)] \cdot \overline{\mathbf{v}_\perp} \tag{102}$$

$$= \|\nabla g(\theta)\| \left(\mathbf{g}^\top \mathbf{p} \cdot \mathbf{p} + \mathbb{E}[\overline{\mathbf{v}_\perp}^\top \mathbf{g}] \cdot \overline{\mathbf{v}_\perp}\right). \tag{103}$$

Let $\widetilde{\gamma}$ be the cosine similarity between $\widetilde{\mathbf{v}^*}$ and $\nabla g(\theta)$. Then

$$\widetilde{\gamma} \coloneqq \frac{(\widetilde{\mathbf{v}^*})^\top \overline{\nabla g(\theta)}}{\|\widetilde{\mathbf{v}^*}\|} \tag{104}$$

$$= \frac{(\mathbf{p}^\top \mathbf{g})^2 + \mathbb{E}[\overline{\mathbf{v}_\perp}^\top \mathbf{g}]\overline{\mathbf{v}_\perp}^\top \mathbf{g}}{\sqrt{(\mathbf{p}^\top \mathbf{g})^2 + \mathbb{E}[\overline{\mathbf{v}_\perp}^\top \mathbf{g}]^2}}. \tag{105}$$

Therefore,

$$\mathbb{E}[\widetilde{\gamma}] = \mathbb{E}\left[\frac{(\mathbf{p}^\top \mathbf{g})^2 + \mathbb{E}[\overline{\mathbf{v}_\perp}^\top \mathbf{g}]\overline{\mathbf{v}_\perp}^\top \mathbf{g}}{\sqrt{(\mathbf{p}^\top \mathbf{g})^2 + \mathbb{E}[\overline{\mathbf{v}_\perp}^\top \mathbf{g}]^2}}\right] \tag{106}$$

$$= \frac{\alpha^2 + \mathbb{E}[\overline{\mathbf{v}_\perp}^\top \mathbf{g}]^2}{\sqrt{\alpha^2 + \mathbb{E}[\overline{\mathbf{v}_\perp}^\top \mathbf{g}]^2}} \tag{107}$$

$$= \sqrt{\alpha^2 + \mathbb{E}[\overline{\mathbf{v}_\perp}^\top \mathbf{g}]^2}. \tag{108}$$

Since $\mathbb{E}[\overline{\mathbf{v}_\perp}^\top \mathbf{g}] = \frac{1}{\|\mathbf{v}_\perp\|}\mathbb{E}[\mathbf{v}_\perp^\top \mathbf{g}]$, we substitute Eq. (76) and $\|\mathbf{v}_\perp\| = \sqrt{q-1}$ into this expression, yielding $\mathbb{E}[\overline{\mathbf{v}_\perp}^\top \mathbf{g}] = \sqrt{q-1}\sqrt{1-\alpha^2}\frac{\Gamma(\frac{d-1}{2})}{\Gamma(\frac{d}{2})\sqrt{\pi}}$. Hence,

$$\mathbb{E}[\widetilde{\gamma}] = \sqrt{\alpha^2 + \frac{(q-1)(1-\alpha^2)}{\pi}\left(\frac{\Gamma(\frac{d-1}{2})}{\Gamma(\frac{d}{2})}\right)^2}. \tag{109}$$

The remaining part is to show the relationship between $\mathbb{E}[\gamma]$ and $\mathbb{E}[\widetilde{\gamma}]$. Note that $\mathbf{v}^*$ is the projection of $\nabla g(\theta)$ on the 2-dimensional subspace spanned by $\mathbf{p}$ and $\overline{\mathbf{v}_\perp}$. By Proposition 1 in Meier et al. (2019), among all the vectors in the subspace spanned by $\mathbf{p}$ and $\overline{\mathbf{v}_\perp}$, $\mathbf{v}^*$ has the largest cosine similarity with $\nabla g(\theta)$. Since $\widetilde{\mathbf{v}^*}$ is a linear combination of $\mathbf{p}$ and $\overline{\mathbf{v}_\perp}$, $\gamma \geq \widetilde{\gamma}$ always holds. Therefore, $\mathbb{E}[\gamma] \geq \mathbb{E}[\widetilde{\gamma}]$, which directly proves the lower bound given in Eq. (96).

Next, we derive $\mathbb{E}[\gamma^2]$. By Eq. (99) we have

$$\mathbb{E}[\gamma^2] = \alpha^2 + \mathbb{E}[(\overline{\mathbf{v}_\perp}^\top \mathbf{g})^2]. \tag{110}$$

Since $\|\mathbf{v}_\perp\| = \sqrt{q-1}$, using Eq. (81) we have

$$\mathbb{E}[(\overline{\mathbf{v}_\perp}^\top \mathbf{g})^2] = \frac{1}{\|\mathbf{v}_\perp\|^2}\mathbb{E}[(\mathbf{v}_\perp^\top \mathbf{g})^2] \tag{111}$$

$$= \frac{1}{d-1}\left(\frac{2}{\pi}(q-2)+1\right)(1-\alpha^2). \tag{112}$$

Plugging Eq. (112) into Eq. (110), we obtain Eq. (98).

Finally, by applying Jensen's inequality $(\mathbb{E}[\gamma])^2 \leq \mathbb{E}[\gamma^2]$, we derive the upper bound for $\mathbb{E}[\gamma]$, which leads to the following result:

$$\mathbb{E}[\gamma] \leq \sqrt{\mathbb{E}[\gamma^2]} = \sqrt{\alpha^2 + \frac{1}{d-1}\left(\frac{2}{\pi}(q-2)+1\right)(1-\alpha^2)}. \tag{113}$$

This establishes Eq. (97), thereby completing the proof. □

C.3.2 THE CASE OF $s > 1$

In the case of $s > 1$, we rewrite the Prior-OPT estimator in the following form:

$$\mathbf{v}^* = \sum_{i=1}^{s} \nabla g(\theta)^\top \mathbf{p}_i \cdot \mathbf{p}_i + \nabla g(\theta)^\top \overline{\mathbf{v}_\perp} \cdot \overline{\mathbf{v}_\perp}, \tag{114}$$

where

$$\mathbf{v}_\perp \coloneqq \sum_{i=1}^{q-s} \operatorname{sign}(\nabla g(\theta)^\top \mathbf{u}_i) \cdot \mathbf{u}_i. \tag{115}$$

Note that Eq. (115) approximates Eq. (14) under the directional derivative approximation. Furthermore, it should also be noted that $\mathbf{v}_\perp$ defined in Eq. (115) is consistent with that in Eq. (83), and thus the conclusions regarding $\mathbf{v}_\perp$ derived in Appendix C.2.2 remain valid in this section (e.g., Eq. (88)).

Now, we present the proof of Theorem 3.4 for the Prior-OPT estimator defined in Eq. (114).

Proof. Let $\mathbf{g} \coloneqq \overline{\nabla g(\theta)}$. Then

$$\mathbf{v}^* = \|\nabla g(\theta)\| \left(\sum_{i=1}^{s} \mathbf{g}^\top \mathbf{p}_i \cdot \mathbf{p}_i + \mathbf{g}^\top \overline{\mathbf{v}_\perp} \cdot \overline{\mathbf{v}_\perp}\right). \tag{116}$$

We also note that $\mathbf{v}_\perp$ is a linear combination of $\mathbf{u}_1$ to $\mathbf{u}_{q-s}$, all of which are orthogonal to $\{\mathbf{p}_i\}_{i=1}^s$, so $\mathbf{v}_\perp$ is also orthogonal to $\{\mathbf{p}_i\}_{i=1}^s$. Therefore, $\|\mathbf{v}^*\| = \|\nabla g(\theta)\|\sqrt{\sum_{i=1}^s (\mathbf{p}_i^\top \mathbf{g})^2 + (\overline{\mathbf{v}_\perp}^\top \mathbf{g})^2}$. Hence

$$\gamma = \frac{(\mathbf{v}^*)^\top \overline{\nabla g(\theta)}}{\|\mathbf{v}^*\|} \tag{117}$$

$$= \sqrt{\sum_{i=1}^{s} (\mathbf{p}_i^\top \mathbf{g})^2 + (\overline{\mathbf{v}_\perp}^\top \mathbf{g})^2}. \tag{118}$$

We define a new estimator

$$\widetilde{\mathbf{v}^*} := \sum_{i=1}^{s} \nabla g(\theta)^\top \mathbf{p}_i \cdot \mathbf{p}_i + \mathbb{E}[\overline{\mathbf{v}_\perp}^\top \nabla g(\theta)] \cdot \overline{\mathbf{v}_\perp} \tag{119}$$

$$= \|\nabla g(\theta)\| \left(\sum_{i=1}^{s} \mathbf{g}^\top \mathbf{p}_i \cdot \mathbf{p}_i + \mathbb{E}[\overline{\mathbf{v}_\perp}^\top \mathbf{g}] \cdot \overline{\mathbf{v}_\perp} \right). \tag{120}$$

Let $\widetilde{\gamma}$ be the cosine similarity between $\widetilde{\mathbf{v}^*}$ and $\nabla g(\theta)$. Then

$$\widetilde{\gamma} := \frac{(\widetilde{\mathbf{v}^*})^\top \overline{\nabla g(\theta)}}{\|\widetilde{\mathbf{v}^*}\|} \tag{121}$$

$$= \frac{\sum_{i=1}^{s} (\mathbf{p}_i^\top \mathbf{g})^2 + \mathbb{E}[\overline{\mathbf{v}_\perp}^\top \mathbf{g}] \overline{\mathbf{v}_\perp}^\top \mathbf{g}}{\sqrt{\sum_{i=1}^{s} (\mathbf{p}_i^\top \mathbf{g})^2 + \mathbb{E}[\overline{\mathbf{v}_\perp}^\top \mathbf{g}]^2}}. \tag{122}$$

Therefore,

$$\mathbb{E}[\widetilde{\gamma}] = \mathbb{E}\left[\frac{\sum_{i=1}^{s} (\mathbf{p}_i^\top \mathbf{g})^2 + \mathbb{E}[\overline{\mathbf{v}_\perp}^\top \mathbf{g}] \overline{\mathbf{v}_\perp}^\top \mathbf{g}}{\sqrt{\sum_{i=1}^{s} (\mathbf{p}_i^\top \mathbf{g})^2 + \mathbb{E}[\overline{\mathbf{v}_\perp}^\top \mathbf{g}]^2}} \right] \tag{123}$$

$$= \frac{\sum_{i=1}^{s} \alpha_i^2 + \mathbb{E}[\overline{\mathbf{v}_\perp}^\top \mathbf{g}]^2}{\sqrt{\sum_{i=1}^{s} \alpha_i^2 + \mathbb{E}[\overline{\mathbf{v}_\perp}^\top \mathbf{g}]^2}} \tag{124}$$

$$= \sqrt{\sum_{i=1}^{s} \alpha_i^2 + \mathbb{E}[\overline{\mathbf{v}_\perp}^\top \mathbf{g}]^2}. \tag{125}$$

Since $\mathbb{E}[\overline{\mathbf{v}_\perp}^\top \mathbf{g}] = \frac{1}{\|\mathbf{v}_\perp\|} \mathbb{E}[\mathbf{v}_\perp^\top \mathbf{g}]$, we substitute Eq. (88) and $\|\mathbf{v}_\perp\| = \sqrt{q-s}$ into this expression, yielding $\mathbb{E}[\overline{\mathbf{v}_\perp}^\top \mathbf{g}] = \sqrt{q-s}\sqrt{1 - \sum_{i=1}^{s} \alpha_i^2} \frac{\Gamma(\frac{d-s}{2})}{\Gamma(\frac{d-s+1}{2})\sqrt{\pi}}$. Hence,

$$\mathbb{E}[\widetilde{\gamma}] = \sqrt{\sum_{i=1}^{s} \alpha_i^2 + \frac{(q-s)\left(1 - \sum_{i=1}^{s} \alpha_i^2\right)}{\pi} \left(\frac{\Gamma(\frac{d-s}{2})}{\Gamma(\frac{d-s+1}{2})} \right)^2}. \tag{126}$$

The remaining part is to show the relationship between $\mathbb{E}[\gamma]$ and $\mathbb{E}[\widetilde{\gamma}]$. We note that $\mathbf{v}^*$ is the projection of $\nabla g(\theta)$ on the $(s+1)$-dimensional subspace spanned by $\{\mathbf{p}_1, \mathbf{p}_2, \ldots, \mathbf{p}_s, \overline{\mathbf{v}_\perp}\}$. By Proposition 1 in Meier et al. (2019), among all the vectors in the subspace spanned by $\{\mathbf{p}_1, \mathbf{p}_2, \ldots, \mathbf{p}_s, \overline{\mathbf{v}_\perp}\}$, $\mathbf{v}^*$ has the largest cosine similarity with $\nabla g(\theta)$. Since $\widetilde{\mathbf{v}^*}$ also lies in this subspace, $\gamma \geq \widetilde{\gamma}$ always holds. Therefore, $\mathbb{E}[\gamma] \geq \mathbb{E}[\widetilde{\gamma}]$, which directly proves the lower bound given in Eq. (15).

Next, we derive $\mathbb{E}[\gamma^2]$. By Eq. (117) we have

$$\mathbb{E}[\gamma^2] = \sum_{i=1}^{s} \alpha_i^2 + \mathbb{E}[(\overline{\mathbf{v}_\perp}^\top \mathbf{g})^2]. \tag{127}$$

Since $\|\mathbf{v}_\perp\| = \sqrt{q-s}$, using Eq. (93) we have

$$\mathbb{E}[(\overline{\mathbf{v}_\perp}^\top \mathbf{g})^2] = \frac{1}{\|\mathbf{v}_\perp\|^2} \mathbb{E}[(\mathbf{v}_\perp^\top \mathbf{g})^2] \tag{128}$$

$$= \frac{1}{d-s} \left(\frac{2}{\pi}(q-s-1) + 1 \right) \left(1 - \sum_{i=1}^{s} \alpha_i^2 \right). \tag{129}$$

Plugging Eq. (129) into Eq. (127), we obtain Eq. (17).

Finally, by applying Jensen's inequality $(\mathbb{E}[\gamma])^2 \leq \mathbb{E}[\gamma^2]$, we derive the upper bound for $\mathbb{E}[\gamma]$, which leads to the following result:

$$\mathbb{E}[\gamma] \leq \sqrt{\mathbb{E}[\gamma^2]} = \sqrt{\sum_{i=1}^{s} \alpha_i^2 + \frac{1}{d-s} \left(\frac{2}{\pi}(q-s-1) + 1 \right) \left(1 - \sum_{i=1}^{s} \alpha_i^2 \right)}. \tag{130}$$

This establishes Eq. (16), thereby completing the proof. □

D Derivation of the Condition for Prior-OPT to Outperform Sign-OPT

With the formulas of $\mathbb{E}[\gamma^2]$ of Sign-OPT (Eq. (10)) and Prior-OPT (Eq. (17)), we now derive the exact value of α_i for which Prior-OPT can outperform Sign-OPT on gradient estimation.

Now, we rewrite the formulas of $\mathbb{E}[\gamma^2]$ of Sign-OPT and Prior-OPT as follows:

$$\mathbb{E}[\gamma^2]_{\text{Sign-OPT}} = \frac{1}{d}\left(\frac{2}{\pi}(q-1)+1\right), \tag{131}$$

$$\mathbb{E}[\gamma^2]_{\text{Prior-OPT}} = \sum_{i=1}^{s}\alpha_i^2 + \frac{1}{d-s}\left(\frac{2}{\pi}(q-s-1)+1\right)\left(1-\sum_{i=1}^{s}\alpha_i^2\right). \tag{132}$$

We need to find the value of α_i such that $\mathbb{E}[\gamma^2]_{\text{Prior-OPT}} > \mathbb{E}[\gamma^2]_{\text{Sign-OPT}}$.

Let $A \coloneqq \sum_{i=1}^{s}\alpha_i^2$, and the inequality becomes:

$$A + (1-A)\cdot\frac{1}{d-s}\left(\frac{2}{\pi}(q-s-1)+1\right) > \frac{1}{d}\left(\frac{2}{\pi}(q-1)+1\right). \tag{133}$$

Now let us simplify the left side of Eq. (133) to $\mathbb{E}[\gamma^2]_{\text{Prior-OPT}} = A + (1-A)C_2$, where $C_2 \coloneqq \frac{1}{d-s}\left(\frac{2}{\pi}(q-s-1)+1\right)$.

Then, let us simplify the right side of Eq. (133) to $\mathbb{E}[\gamma^2]_{\text{Sign-OPT}} = C_1$, where $C_1 \coloneqq \frac{1}{d}\left(\frac{2}{\pi}(q-1)+1\right)$.

The inequality of Eq. (133) becomes:

$$A + (1-A)C_2 > C_1. \tag{134}$$

We rearrange the above inequality as $A(1-C_2)+C_2 > C_1$, and then we solve for A:

$$A > \frac{C_1 - C_2}{1-C_2}. \tag{135}$$

Substituting the formulas of A, C_1, and C_2 into Eq. (135), we have:

$$\sum_{i=1}^{s}\alpha_i^2 > \frac{\frac{1}{d}\left(\frac{2}{\pi}(q-1)+1\right) - \frac{1}{d-s}\left(\frac{2}{\pi}(q-s-1)+1\right)}{1-\frac{1}{d-s}\left(\frac{2}{\pi}(q-s-1)+1\right)}. \tag{136}$$

This is the condition of $\sum_{i=1}^{s}\alpha_i^2$ for Prior-OPT to outperform Sign-OPT. But this inequality is complex, next we show how to further simplify this inequality. Under the reasonable assumptions that $q \ll d$, which implies that the input dimension is much larger than the total number of vectors (and consequently $s \ll d$ since $s < q$), the above inequality can be simplified.

We first approximate denominator of Eq. (136), note that when $s \ll d$, we have $d - s \approx d$. Therefore, the denominator simplifies to:

$$D \coloneqq 1 - \frac{1}{d-s}\left(\frac{2}{\pi}(q-s-1)+1\right) \approx 1 - \frac{1}{d}\left(\frac{2}{\pi}(q-s-1)+1\right). \tag{137}$$

Since $\frac{1}{d}\left(\frac{2}{\pi}(q-s-1)+1\right)$ is a small number because $q \ll d$ (denote it as ϵ), the denominator becomes $D \approx 1-\epsilon \approx 1$. Next, we simplify the numerator as:

$$N := \frac{1}{d}\left(\frac{2}{\pi}(q-1)+1\right) - \frac{1}{d-s}\left(\frac{2}{\pi}(q-s-1)+1\right) \tag{138}$$

$$\approx \frac{1}{d}\left(\frac{2}{\pi}(q-1)+1\right) - \frac{1}{d}\left(\frac{2}{\pi}(q-s-1)+1\right) \tag{139}$$

$$= \frac{1}{d}\left(\frac{2}{\pi}(q-1)+1-\left(\frac{2}{\pi}(q-s-1)+1\right)\right) \tag{140}$$

$$= \frac{2s}{\pi d}. \tag{141}$$

Now, let us substitute the simplified N and D into the right side of Eq. (136), we have

$$\sum_{i=1}^{s} \alpha_i^2 > \frac{N}{D} \approx \frac{2s}{\pi d}. \tag{142}$$

This is the simplified condition of $\sum_{i=1}^{s} \alpha_i^2$ for Prior-OPT to outperform Sign-OPT.

Dividing both sides by s, we get the condition for the average squared cosine similarity $\overline{\alpha^2} := \frac{1}{s}\sum_{i=1}^{s} \alpha_i^2 > \frac{2}{\pi d}$. Since $\frac{2}{\pi d}$ is typically a very small value due to the large input dimension d, this threshold is relatively easy to satisfy. Therefore, Prior-OPT generally outperforms Sign-OPT when the priors have even a minimal level of informativeness (non-zero α_i).

E Discussions

E.1 Prior Accuracy α_i

$\alpha_i = \mathbf{p}_i^\top \overline{\nabla g(\theta)}$ is the cosine similarity between the i-th surrogate model's gradient (the i-th prior) and the true gradient. The value of α_i is only used in the theoretical analysis and is not required for practical algorithm. Algorithm 1 does not require any α_i or the true gradient to run. We assume that α_i is known in the theoretical analysis so that we can analyze its impact on the expectation of the final estimated gradient's cosine similarity γ to the true gradient, which derives the solutions of $\mathbb{E}[\gamma]$ and $\mathbb{E}[\gamma^2]$. Figs. 5 and 13 demonstrate the quantitative analysis for $\mathbb{E}[\gamma]$ and $\mathbb{E}[\gamma^2]$, respectively.

E.2 Differences between OPT and Prior-OPT

Although the gradient estimation formulas in OPT (Cheng et al., 2019) and Prior-OPT (Eq. (13)) exhibit some similarities, they differ in two key aspects.

First, the formula of Prior-OPT (Eq. (13)) is not identical to that of OPT. In Eq. (13), the last term involves the ℓ_2 normalization of $\mathbf{v}_\perp$, where $\mathbf{v}_\perp = \sum_{i=1}^{q-s} \text{sign}(g(\theta+\sigma\mathbf{u}_i) - g(\theta)) \cdot \mathbf{u}_i$. and $\mathbf{u}_1, \ldots, \mathbf{u}_{q-s}$ are orthonormal random vectors. Consequently, Prior-OPT employs more precise finite difference estimation for the priors (the first term), while relying on sign-based estimation for the random vector components. This distinction arises because random vectors $\mathbf{u}_1, \ldots, \mathbf{u}_{q-s}$ are identically distributed, leading to a relatively consistent cosine similarity with the true gradient. This observation enables efficient sign-based estimation for random vectors. In contrast, the cosine similarities between the prior directions $\mathbf{p}_1, \ldots, \mathbf{p}_s$ and the true gradient $\nabla g(\theta)$ are unknown and may differ significantly. Thus, the coefficients for priors require more precise estimation, necessitating a separate binary search procedure. Therefore, Prior-OPT is not merely a simple extension of OPT that incorporates priors, as it handles priors and random directions differently to address these challenges.

Second, OPT does not require its random directions to be orthogonality, while Prior-OPT explicitly does. Although a small number of randomly sampled vectors are approximately orthogonal in the high-dimensional space, this is not always the case for *multiple priors*. Priors derived from potentially correlated models are less likely to be orthogonal to each other. If the Gram-Schmidt orthonormalization is omitted, the estimated gradient obtained using Eq. (7) and Eq. (13) may become less accurate, potentially degrading performance. Furthermore, the formulas of $\mathbb{E}[\gamma]$ and $\mathbb{E}[\gamma^2]$ derived from our theoretical analysis would no longer hold in such scenarios.

E.3 PRACTICALITY OF THEORY

No matter how complex a real-world situation is, the generation of adversarial examples mainly relies on gradient vectors, as they increase the classification loss, leading to misclassifications. Our theory focuses on the similarity between the estimated and true gradient, which applies to all image classifiers. One of the most common challenges in real-world scenarios is the significant difference between models, which results in different gradients. We address this issue by introducing the variable α_i in Eqs. (11), (12), (15), (16), and (17), which represents the cosine similarity between the i-th prior and the true gradient, and is assumed to be known in our theoretical analysis. In summary, our theory is universally applicable to real-world scenarios.

F EXPERIMENTAL SETTING

In this section, we provide the hyperparameter settings of our approach and compared methods, which include HSJA, TA, G-TA, GeoDA, Evolutionary, Triangle Attack, SurFree, Sign-OPT, SVM-OPT, SQBA, and BBA.

Experimental Equipment. The experiments of all methods are conducted by using PyTorch 1.7.1 framework on NVIDIA V100 and A100. NVIDIA A100 GPU has TensorFloat-32 (TF32) tensor cores to achieve better performance (i.e., the computation speed), and enabling TF32 tensor cores causes a large relative error compared to double precision, especially in attacks of ViTs. Therefore, in all experiments, we set `torch.backends.cuda.matmul.allow_tf32 = False` and `torch.backends.cudnn.allow_tf32 = False` to obtain higher precision.

CIFAR-10 dataset. In the CIFAR-10 dataset, we select 4 networks as target models, including a 272-layer PyramidNet+ShakeDrop network (PyramidNet-272) (Han et al., 2017; Yamada et al., 2019), two wide residual networks with 28 and 40 layers (WRN-28 and WRN-40) (Zagoruyko & Komodakis, 2016), and DenseNet-BC-190 ($k = 40$) (Huang et al., 2017). We adopt the ResNet-110 as the surrogate model in the CIFAR-10 dataset.

Prior-OPT and Prior-Sign-OPT. Hyperparameters of Prior-OPT and Prior-Sign-OPT are listed in Table 3. Our implementation source code is based on the PyTorch framework. In the experiments of targeted attacks with the same target class, we set the initial direction θ_0 of Prior-OPT and Prior-Sign-OPT to the direction of the same image of the target class used by other methods.

Table 3: The hyperparameters of Prior-OPT and Prior-Sign-OPT.

Dataset	Hyperparameter	Value
CIFAR-10	q, total number of vectors for estimating a gradient, including priors and random vectors	200
	the binary search's stopping threshold	$\frac{\beta}{500}$
	the number of iterations	1,000
	$\mathbf{g}_{\max}$, the maximum gradient norm for the gradient clipping operation	0.1
ImageNet	q, total number of vectors for estimating a gradient, including priors and random vectors	200
	the binary search's stopping threshold	1×10^{-4}
	the number of iterations	1,000
	$\mathbf{g}_{\max}$, the maximum gradient norm for the gradient clipping operation	1.0

Table 4: The hyperparameters of Sign-OPT and SVM-OPT.

Hyperparameter	Value
q, number of queries for estimating an approximate gradient	200
the number of iterations	1,000
the binary search's stopping threshold of the CIFAR-10 dataset	$\frac{\beta}{500}$
the binary search's stopping threshold of the ImageNet dataset	1×10^{-4}

Table 5: The hyperparameters of HSJA, TA and G-TA.

Hyperparameter	Value
γ, threshold of the binary search	1.0
B_0, the initial batch size for gradient estimation	100
B_{max}, the maximum batch size for gradient estimation	10,000
the search method for step size	geometric progression
number of iterations	64
radius ratio r for the ImageNet dataset in G-TA	1.1
radius ratio r for the CIFAR-10 dataset in G-TA	1.5

Table 6: The hyperparameters of Evolutionary.

Hyperparameter	Value
c_{cov}, the hyperparameter of updating the diagonal covariance matrix $\mathbf{C}$	0.001
σ, the deviation for bias	0.03
μ, the mean for bias, and it is a critical hyper-parameter controlling the strength of going towards the original image	0.01
`maxlen`, the maximum length of successful attacks for calculating μ	30

Table 7: The hyperparameters of GeoDA.

Dataset	Hyperparameter	Value
CIFAR-10	subspace dimension, the dimension of 2D DCT basis's subspace	10
	ϵ, the step size of searching the decision boundary	0.5
ImageNet	subspace dimension, the dimension of 2D DCT basis's subspace	75
	ϵ, the step size of searching the decision boundary	5

Table 8: The hyperparameters of Triangle Attack.

Dataset	Hyperparameter	Value
CIFAR-10	d, the number of picked dimensions	3
	`ratio mask`, the ratio of the mask size for obtaining the low-frequency mask	0.3
	θ_{init}, the initial angle of the subspace equals $\theta_{\text{init}} \times \pi/32$	2
	α_{init}, the initial angle of alpha	$\pi/2$
	the maximum iteration number of attack algorithm in 2D subspace	2
ImageNet	d, the number of picked dimensions	3
	`ratio mask`, the ratio of the mask size for obtaining the low-frequency mask	0.1
	θ_{init}, the initial angle of the subspace equals $\theta_{\text{init}} \times \pi/32$	2
	α_{init}, the initial angle of alpha	$\pi/2$
	the maximum iteration number of attack algorithm in 2D subspace	2

Sign-OPT and SVM-OPT. Hyperparameters of Sign-OPT and SVM-OPT are listed in Table 4. For fair comparison, we set the hyperparameters of Prior-OPT and Prior-Sign-OPT to be same with Sign-OPT and SVM-OPT, e.g., the same number of vectors for the gradient estimation q.

HSJA, TA and G-TA. Hyperparameters of HSJA, TA and G-TA are listed in Table 5. TA has no additional hyperparameters. G-TA has an additional hyperparameter radius ratio r to control the shape of the virtual semi-ellipsoid, which is set to be different values in CIFAR-10 and ImageNet, as shown in Table 5.

Evolutionary. We follow the official implementation source code of Evolutionary to set its hyperparameters, as shown in Table 6.

GeoDA. GeoDA only supports untargeted attacks, and the convergence of ℓ_2 norm attacks of GeoDA is proved. Thus, we conduct experiments of ℓ_2 norm untargeted attacks of GeoDA, and the hyperparameters of GeoDA are shown in Table 7.

Table 9: The hyperparameters of SurFree.

Hyperparameter	Value
BS_gamma, the stopping threshold in the binary search of α	0.01
BS_max_iteration, the maximum iterations in the binary search for α	10
ρ, the parameter for determining θ_{max}	0.98
T, the parameter for determining the range of α and the best θ	3
θ_{max}, the parameter for determining the range of α	30
n_ortho, the parameter for finding the direction of the lowest ϵ in _get_candidates	100
the binary search's stopping threshold of the ImageNet dataset	1×10^{-4}
frequence_range, the parameter used in constructing dct_mask	$0 \sim 0.5$
with_distance_line_search, the parameter used in _get_candidates	false
with_interpolation, the parameter used in _get_candidates	false
with_alpha_line_search, the parameter used in _get_best_theta	true

Table 10: The hyperparameters of SQBA.

Hyperparameter	Value
threshold, the stopping threshold in the binary search	0.001
min_randoms, the value indirectly determines the number of queries in each gradient estimation	10

Table 11: The hyperparameters of BBA.

Hyperparameter	Value
use_surrogate_bias, whether to use a surrogate model as the bias	True
use_mask_bias, whether to use regional masks as the bias	False
use_perlin_bias, whether to use Perlin Noise as the bias	False
pg_factor, the hyperparameter that controls the strength of the bias	0.3

Triangle Attack. We set the hyperparameter of "ratio mask" as 0.1 and 0.3 in the ImageNet dataset and the CIFAR-10 dataset, respectively. All hyperparameters of Triangle Attack are shown in Table 8.

SurFree. SurFree only supports the ℓ_2 norm attacks. We translate the code from SurFree's official version into the PyTorch version for experiments, and the hyperparameters of SurFree are shown in Table 9.

SQBA. SQBA only supports the ℓ_2 norm untargeted attacks, and the hyperparameters of SQBA are shown in Table 10.

BBA. BBA only supports the ℓ_2 norm attacks, and the hyperparameters of BBA are shown in Table 11. We only use the bias of the surrogate model, and the hyperparameter pg_factor controls the strength of this bias. When the value of pg_factor $= 1$, then the orthogonal step would be equivalent to an iteration of PGD attack. Brunner et al. (2019) suggest that pg_factor $= 0.3$.

G Additional Experimental Results

In this section, we present the computational overhead test results and additional experimental results.

G.1 Computational Overhead

The primary additional computational cost of Prior-OPT compared to Sign-OPT arises from the binary search procedure performed on the priors during gradient estimation. Let d represent the dimension of the input image, q the number of vectors used in gradient estimation, and $f(d)$ the inference time of the target model for an input of dimension d. The time complexity of gradient estimation in Sign-OPT is $O(q \cdot f(d))$. In Prior-OPT, s priors are introduced. Each prior requires a binary search procedure, which involves approximately k inference steps. While k may vary slightly depending on the specific prior or the input configuration, its value generally remains bounded and

logarithmic in scale, given the nature of binary search. Consequently, the time complexity of the gradient estimation step of Prior-OPT can be expressed as:

$$O\left((q - s + (s+1) \cdot k) \cdot f(d) + s \cdot \hat{f}(d)\right). \tag{143}$$

When q is large, s and k is relatively small (i.e., the number of priors is small, and k typically ranges in the tens), $s \cdot \hat{f}(d)$ denotes the time of taking s priors, the additional overhead introduced by Prior-OPT is limited compared to Sign-OPT. While Prior-OPT introduces extra computation due to the binary search procedure on the priors, the increase in time complexity is relatively modest, especially when s remains much smaller than q. This demonstrates that Prior-OPT achieves a balance between computational efficiency and improved gradient estimation.

Table 12 demonstrates the time consumption of Sign-OPT, SVM-OPT, Prior-Sign-OPT, and Prior-OPT, which are measured by conducting untargeted attack on the ImageNet dataset. The surrogate model employs the ResNet-50 architecture and the GPU is NVIDIA Tesla V100. The additional time overhead of Prior-Sign-OPT is mainly the time of obtaining priors on surrogate models. Prior-OPT calculates Eq. (13) to estimate gradients, which calls $s + 1$ times of binary search, where s is the number of surrogate models. This will result in additional time consumption than Prior-Sign-OPT. Note that the major metrics of black-box attacks are not time consumption, but the number of queries and the attack success rate. Because in real-world systems, the number of queries is the main limitation. We need to use as few queries as possible to achieve the highest possible success rate. Table 13 shows the GPU memory allocations of Sign-OPT, Prior-Sign-OPT, and Prior-OPT. Prior-OPT and Prior-Sign-OPT require the transfer-based priors, and thus the additional memory allocation of our approach is mainly consumed in the feed-forward and back-propagation processes of the surrogate models. After obtaining a prior, the GPU memory will be released in a timely manner to save occupancy. Thus, our approach does not take up too much additional GPU memory.

Table 12: The time consumption of attacking one image with $10{,}000$ queries, which are measured by `seconds` on a NVIDIA Tesla V100 GPU.

Method	ResNet-101	SENet-154	ResNeXt-101	GC ViT	Swin Transformer
Sign-OPT (Cheng et al., 2020)	112	197	91	131	88
SVM-OPT (Cheng et al., 2020)	119	189	102	158	98
Prior-Sign-OPT$_{\text{ResNet50}}$	240	372	195	203	183
Prior-OPT$_{\text{ResNet50}}$	342	476	321	357	203

Table 13: The GPU memory allocations of attacks against different target models, which are measured by `MiB` on a NVIDIA Tesla V100 GPU.

Method	ResNet-101	SENet-154	ResNeXt-101	GC ViT	Swin Transformer
Sign-OPT (Cheng et al., 2020)	4,686	6,244	7,272	7,352	8,854
SVM-OPT (Cheng et al., 2020)	4,688	6,246	7,274	7,354	8,856
Prior-Sign-OPT$_{\text{ResNet50}}$	5,222	6,750	7,828	7,856	9,410
Prior-OPT$_{\text{ResNet50}}$	5,222	6,746	7,816	7,846	9,390

G.2 Experimental Results of Large Vision-Language Model

To evaluate the scalability of the proposed approach, we conduct experiments of attacking a CLIP model with the backbone of ViT-L/14, and the surrogate models include ImageNet pretrained ResNet-50, ConViT, CrossViT, MaxViT, and ViT. It is worth noting that these surrogate models are pretrained on ImageNet and their training paradigms are entirely different from the CLIP model. The CLIP model, which stands for Contrastive Language-Image Pretraining, is trained on millions of image-text pairs from the internet using a contrastive learning approach, enabling it to generalize effectively through natural language supervision. By aligning images and text in a shared embedding space, the CLIP model functions as a zero-shot image classifier. We encapsulate it as a $1{,}000$-class classifier by constructing a set of text prompts that correspond to the class names, which are then embedded into the same space as the images. The ViT-L/14 refers to a large variant of the Vision Transformer architecture with the patch size of 14×14.

In the experiments, due to the differences between CLIP and standard classification models, the tested images used in previous experiments may not be classified correctly by CLIP. Therefore, we select a new set of $1{,}000$ images that are correctly classified by both CLIP and the five surrogate models (ResNet-50, ConViT, CrossViT, MaxViT, and ViT) to conduct experiments. The results are shown in Table 14, which demonstrate that incorporating more surrogate models (priors) significantly enhances attack performance. Notably, although the surrogate models are pretrained on the ImageNet dataset and use training methods that are fundamentally different from those of the CLIP model, they still contribute to improved performance.

Table 14: The experimental results of attacking against CLIP with the backbone of ViT-L/14, and the surrogate models include ImageNet pretrained ResNet-50, ConViT, CrossViT, MaxViT, and ViT.

Method	Priors	Mean ℓ_2 Distortion					Attack Success Rate[1]				
		@1K	@2K	@5K	@8K	@10K	@1K	@2K	@5K	@8K	@10K
Sign-OPT (Cheng et al., 2020)	no prior	58.180	49.435	40.261	37.020	35.713	13.4%	15.2%	17.4%	19.1%	19.4%
Prior-Sign-OPT$_{\text{ResNet50}}$	1 prior	56.935	47.234	35.189	30.957	29.517	13.5%	15.5%	22.0%	25.3%	27.3%
Prior-Sign-OPT$_{\text{ConViT}}$	1 prior	55.036	43.327	31.387	27.577	26.250	14.3%	16.3%	24.0%	28.8%	31.5%
Prior-Sign-OPT$_{\text{ResNet50\&ConViT}}$	2 priors	53.658	40.868	27.988	23.954	22.737	14.1%	17.6%	28.0%	34.3%	37.4%
Prior-Sign-OPT$_{\text{ResNet50\&ConViT\&CrossViT}}$	3 priors	50.875	36.428	23.410	19.589	18.414	15.3%	20.5%	37.2%	44.1%	46.7%
Prior-Sign-OPT$_{\text{ResNet50\&ConViT\&CrossViT\&MaxViT}}$	4 priors	49.438	33.941	20.801	17.466	16.296	**15.7%**	23.3%	44.3%	53.2%	57.1%
Prior-Sign-OPT$_{\text{ResNet50\&ConViT\&CrossViT\&MaxViT\&ViT}}$	5 priors	**48.214**	**32.298**	**19.114**	**15.790**	**14.726**	15.0%	**24.1%**	**48.0%**	**56.5%**	**59.3%**
Prior-OPT$_{\text{ResNet50}}$	1 prior	38.934	27.384	20.184	18.520	18.153	23.4%	34.9%	47.3%	50.6%	51.4%
Prior-OPT$_{\text{ConViT}}$	1 prior	31.822	21.267	15.568	14.623	14.362	29.2%	43.3%	56.6%	58.8%	58.9%
Prior-OPT$_{\text{ResNet50\&ConViT}}$	2 priors	29.596	18.088	11.770	10.724	10.427	31.3%	50.1%	68.3%	72.2%	73.4%
Prior-OPT$_{\text{ResNet50\&ConViT\&CrossViT}}$	3 priors	26.355	15.251	9.953	8.834	8.625	35.0%	55.7%	75.2%	79.1%	79.5%
Prior-OPT$_{\text{ResNet50\&ConViT\&CrossViT\&MaxViT}}$	4 priors	26.433	14.261	7.899	6.807	6.562	35.6%	59.5%	82.0%	86.5%	87.3%
Prior-OPT$_{\text{ResNet50\&ConViT\&CrossViT\&MaxViT\&ViT}}$	5 priors	**25.170**	**13.327**	**6.745**	**5.931**	**5.737**	**39.2%**	**63.0%**	**85.9%**	**89.4%**	**89.8%**

[1] The distortion threshold for the attack success rate is 12.26898528811572, which is calculated as $\sqrt{0.001 \times 224 \times 224 \times 3}$.

G.3 Performance of Prior-Only Gradient Estimators

The experimental results in previous sections demonstrate that incorporating a single transfer-based prior enhances performance. To explore this further, it is valuable to investigate an alternative approach where only prior vectors are used, rather than relying on random vectors. We can examine this approach from both theoretical and empirical perspectives.

If all random vectors are eliminated in gradient estimation, the gradient estimator's performance lacks a lower bound, making it unable to guarantee accuracy in the worst-case scenario. However, when random vectors are included in the gradient estimation, the accuracy of the estimator is ensured to have a lower bound. This means that, regardless of how poor the priors are, the estimator maintains a guaranteed minimum level of performance in the worst case. This can be verified through $\mathbb{E}[\gamma]$ derived for Prior-Sign-OPT (Eq. (11)) and Prior-OPT (Eq. (15)).

Specifically, when all random vectors are removed in Prior-Sign-OPT and set $q = s$, Eq. (11) reduces to

$$\mathbb{E}[\gamma] = \frac{1}{\sqrt{q}} \left(\sum_{i=1}^{s} |\alpha_i| \right). \tag{144}$$

In this case, $\mathbb{E}[\gamma]$ depends solely on α_i, which reflects the accuracy of the priors. If α_i is extremely small, the accuracy of the estimated gradient degrades significantly. Similarly, when we remove all random vectors in Prior-OPT and set $q = s$, Eq. (15) reduces to

$$\mathbb{E}[\gamma] \geq \sqrt{\sum_{i=1}^{s} \alpha_i^2}. \tag{145}$$

This demonstrates that, without random vectors, the gradient estimation is entirely reliant on the quality of the priors (i.e., the α_i values), and poor priors can result in arbitrarily poor performance.

Conversely, when random vectors are included, the formula incorporating them guarantees a lower bound for $\mathbb{E}[\gamma]$. This lower bound can be derived by setting $\alpha_i = 0$ in Eq. (11) and Eq. (15). For Prior-Sign-OPT, the lower bound of $\mathbb{E}[\gamma]$ is

$$\mathbb{E}[\gamma] \geq \frac{q-s}{\sqrt{q}} \cdot \frac{\Gamma(\frac{d-s}{2})}{\Gamma(\frac{d-s+1}{2})\sqrt{\pi}}. \tag{146}$$

Table 15: Mean ℓ_2 distortions of targeted attacks on the ImageNet dataset against GC ViT, where Pure-Prior-Sign-OPT and Pure-Prior-OPT use only priors in the gradient estimation.

Method	Priors	Targeted Attacks								
		@1K	@2K	@5K	@8K	@10K	@12K	@15K	@18K	@20K
Sign-OPT (Cheng et al., 2020)	no prior	53.026	42.049	28.210	22.156	19.557	17.661	15.556	14.018	13.194
Pure-Prior-Sign-OPT$_{\text{ResNet50}}$	1 prior	52.337	51.255	51.024	51.017	51.017	51.017	51.017	51.017	51.017
Pure-Prior-Sign-OPT$_{\text{ResNet50\&ConViT}}$	2 priors	**41.468**	38.481	37.791	37.787	37.787	37.787	37.787	37.787	37.787
Pure-Prior-OPT$_{\text{ResNet50}}$	1 prior	53.673	53.416	53.385	53.385	53.385	53.385	53.385	53.385	53.385
Pure-Prior-OPT$_{\text{ResNet50\&ConViT}}$	2 priors	41.631	38.687	38.256	38.250	38.250	38.250	38.250	38.250	38.250
Prior-Sign-OPT$_{\text{ResNet50}}$ (**ours**)	1 prior	52.491	41.333	26.857	20.829	18.427	16.681	14.741	13.337	12.593
Prior-Sign-OPT$_{\text{ResNet50\&ConViT}}$ (**ours**)	2 priors	51.465	39.537	25.124	19.216	16.841	**15.115**	**13.321**	**12.030**	**11.377**
Prior-OPT$_{\text{ResNet50}}$ (**ours**)	1 prior	50.323	39.615	25.876	20.309	18.120	16.488	14.750	13.535	12.918
Prior-OPT$_{\text{ResNet50\&ConViT}}$ (**ours**)	2 priors	47.739	**36.129**	**23.177**	**18.528**	**16.764**	15.467	14.121	13.193	12.699

Table 16: Attack success rates of targeted attacks on the ImageNet dataset against GC ViT, where Pure-Prior-Sign-OPT and Pure-Prior-OPT use only priors in the gradient estimation.

Method	Priors	Targeted Attacks								
		@1K	@2K	@5K	@8K	@10K	@12K	@15K	@18K	@20K
Sign-OPT (Cheng et al., 2020)	no prior	1.0%	1.9%	8.5%	20.3%	30.2%	38.7%	48.8%	57.5%	61.2%
Pure-Prior-Sign-OPT$_{\text{ResNet50}}$	1 prior	2.3%	2.6%	2.7%	2.7%	2.7%	2.7%	2.7%	2.7%	2.7%
Pure-Prior-Sign-OPT$_{\text{ResNet50\&ConViT}}$	2 priors	8.6%	10.7%	11.6%	11.6%	11.6%	11.6%	11.6%	11.6%	11.6%
Pure-Prior-OPT$_{\text{ResNet50}}$	1 prior	2.1%	2.3%	2.3%	2.3%	2.3%	2.3%	2.3%	2.3%	2.3%
Pure-Prior-OPT$_{\text{ResNet50\&ConViT}}$	2 priors	**9.7%**	**12.5%**	12.7%	12.7%	12.7%	12.7%	12.7%	12.7%	12.7%
Prior-Sign-OPT$_{\text{ResNet50}}$ (**ours**)	1 prior	0.9%	2.6%	12.0%	25.1%	34.4%	41.9%	49.6%	58.2%	62.9%
Prior-Sign-OPT$_{\text{ResNet50\&ConViT}}$ (**ours**)	2 priors	0.9%	3.3%	15.8%	32.2%	40.2%	**47.9%**	**57.1%**	**62.5%**	**66.0%**
Prior-OPT$_{\text{ResNet50}}$ (**ours**)	1 prior	1.5%	4.6%	14.2%	25.4%	32.8%	40.4%	50.5%	56.8%	60.5%
Prior-OPT$_{\text{ResNet50\&ConViT}}$ (**ours**)	2 priors	2.6%	9.2%	**24.7%**	**36.2%**	**41.0%**	46.8%	53.5%	58.0%	60.7%

For Prior-OPT, the lower bounds of $\mathbb{E}[\gamma]$ is

$$\mathbb{E}[\gamma] \geq \sqrt{\frac{q-s}{\pi}} \cdot \frac{\Gamma(\frac{d-s}{2})}{\Gamma(\frac{d-s+1}{2})}, \tag{147}$$

thereby providing robustness with random vectors when the priors are of low quality. Furthermore, in Prior-OPT's gradient estimation, each prior requires a binary search, whereas random vectors do not. Random vectors require only a single query per vector, making them more efficient in this regard.

We present experimental results of targeted attacks using variants of the Prior-Sign-OPT and Prior-OPT algorithms, in which random vectors are excluded from the gradient estimation, and only priors (i.e., gradients from surrogate models) are used. These variants are referred to as **Pure-Prior-Sign-OPT** and **Pure-Prior-OPT**. The experimental results of attacks against GC ViT (Hatamizadeh et al., 2023) on the ImageNet dataset are presented in Tables 15 and 16. The results indicate that Pure-Prior-Sign-OPT and Pure-Prior-OPT fail to outperform Sign-OPT when the query budget exceeds $2{,}000$, even though Sign-OPT relies solely on random vectors without incorporating priors. Furthermore, as the query budget increases, the distortions and attack success rates for Pure-Prior-Sign-OPT and Pure-Prior-OPT remain relatively stable, highlighting their inefficiency in utilizing additional queries to improve attack effectiveness.

G.4 Effect of PGD Initialization on the Performance of SQBA and BBA Methods

Previous experiments have demonstrated that applying PGD (Projected Gradient Descent) initialization, denoted as Prior-OPT$_{\theta_0^{\text{PGD}}}$ and Prior-Sign-OPT$_{\theta_0^{\text{PGD}}}$, significantly enhances the performance of adversarial attacks. This raises the question: How would other baseline methods perform if PGD initialization were applied to them as well? To investigate this, we propose variants of the SQBA (Park et al., 2024) and BBA (Brunner et al., 2019) methods, labeled as SQBA$_{\theta_0^{\text{PGD}}}$ and BBA$_{\theta_0^{\text{PGD}}}$, in which PGD initialization is utilized on a surrogate model to generate the initial adversarial examples.

The mean ℓ_2 distortions of the experimental results on the ImageNet dataset are presented in Tables 17, 18, 19, 20, and 21, while the corresponding attack success rates are shown in Tables 22, 23, 24, 25, and 26. The distortion threshold for attack success rates is 16.37690446940447 for attacks

Table 17: Mean ℓ_2 distortions of untargeted attacks on the ImageNet dataset against Inception-v4.

Method	Untargeted Attacks									
	@1K	@2K	@3K	@4K	@5K	@6K	@7K	@8K	@9K	@10K
SQBA$_{\text{IncResV2}}$ (Park et al., 2024)	26.134	19.035	15.200	12.799	11.189	10.015	9.129	8.432	7.878	7.417
SQBA$_{\theta_0^{\text{PGD}}+\text{IncResV2}}$ (Park et al., 2024)	**22.698**	16.882	13.731	11.699	10.314	9.301	8.543	7.931	7.426	7.017
BBA$_{\text{IncResV2}}$ (Brunner et al., 2019)	38.782	28.437	23.673	20.745	18.757	17.373	16.307	15.474	14.781	14.191
BBA$_{\theta_0^{\text{PGD}}+\text{IncResV2}}$ (Brunner et al., 2019)	26.297	20.370	17.460	15.647	14.404	13.484	12.754	12.177	11.700	11.295
Prior-Sign-OPT$_{\text{IncResV2}}$	81.991	42.403	25.355	17.163	12.835	10.191	8.508	7.365	6.508	5.842
Prior-Sign-OPT$_{\theta_0^{\text{PGD}}+\text{IncResV2}}$	23.596	15.347	11.565	9.458	8.074	7.085	6.330	5.729	5.249	4.863
Prior-OPT$_{\text{IncResV2}}$	49.279	18.135	9.426	**6.798**	**5.718**	**5.148**	**4.747**	**4.451**	**4.215**	**4.027**
Prior-OPT$_{\theta_0^{\text{PGD}}+\text{IncResV2}}$	22.852	**12.194**	**8.896**	7.452	6.568	5.947	5.485	5.114	4.809	4.548

Table 18: Mean ℓ_2 distortions of untargeted attacks on the ImageNet dataset against ViT.

Method	Untargeted Attacks									
	@1K	@2K	@3K	@4K	@5K	@6K	@7K	@8K	@9K	@10K
SQBA$_{\text{ConViT}}$ (Park et al., 2024)	12.886	9.762	8.045	6.972	6.240	5.702	5.278	4.947	4.681	4.452
SQBA$_{\theta_0^{\text{PGD}}+\text{ConViT}}$ (Park et al., 2024)	10.794	8.424	7.094	6.227	5.647	5.204	4.856	4.572	4.337	4.143
BBA$_{\text{ConViT}}$ (Brunner et al., 2019)	22.716	16.153	13.409	11.886	10.893	10.155	9.614	9.193	8.868	8.595
BBA$_{\theta_0^{\text{PGD}}+\text{ConViT}}$ (Brunner et al., 2019)	11.163	9.431	8.535	7.958	7.534	7.227	6.982	6.783	6.615	6.477
Prior-Sign-OPT$_{\text{ConViT}}$	46.883	24.551	14.592	10.329	8.057	6.669	5.755	5.142	4.688	4.313
Prior-Sign-OPT$_{\theta_0^{\text{PGD}}+\text{ConViT}}$	9.011	6.935	5.752	5.025	**4.504**	**4.108**	**3.803**	**3.549**	**3.345**	**3.174**
Prior-OPT$_{\text{ConViT}}$	26.649	11.706	7.632	6.025	5.228	4.728	4.380	4.117	3.909	3.754
Prior-OPT$_{\theta_0^{\text{PGD}}+\text{ConViT}}$	**8.688**	**6.646**	**5.595**	**4.962**	4.551	4.245	4.003	3.808	3.640	3.511

Table 19: Mean ℓ_2 distortions of untargeted attacks on the ImageNet dataset against GC ViT.

Method	Untargeted Attacks									
	@1K	@2K	@3K	@4K	@5K	@6K	@7K	@8K	@9K	@10K
SQBA$_{\text{ConViT}}$ (Park et al., 2024)	19.307	14.049	11.170	9.327	8.072	7.135	6.434	5.877	5.426	5.056
SQBA$_{\theta_0^{\text{PGD}}+\text{ConViT}}$ (Park et al., 2024)	**15.652**	11.520	9.197	7.752	6.754	6.033	5.479	5.034	4.673	4.370
BBA$_{\text{ConViT}}$ (Brunner et al., 2019)	29.928	21.095	17.061	14.680	13.103	11.954	11.020	10.302	9.694	9.188
BBA$_{\theta_0^{\text{PGD}}+\text{ConViT}}$ (Brunner et al., 2019)	15.959	12.688	11.054	9.997	9.230	8.627	8.164	7.766	7.430	7.131
Prior-Sign-OPT$_{\text{ConViT}}$	55.864	34.707	22.793	16.584	12.893	10.546	8.895	7.678	6.712	5.972
Prior-Sign-OPT$_{\theta_0^{\text{PGD}}+\text{ConViT}}$	17.159	11.230	8.642	7.209	6.250	5.551	5.009	4.560	**4.205**	**3.916**
Prior-OPT$_{\text{ConViT}}$	39.497	18.955	12.320	9.275	7.641	6.599	5.828	5.251	4.817	4.453
Prior-OPT$_{\theta_0^{\text{PGD}}+\text{ConViT}}$	16.949	**10.708**	**8.251**	**6.937**	**6.031**	**5.391**	**4.913**	**4.530**	4.219	3.961

Table 20: Mean ℓ_2 distortions of untargeted attacks on the ImageNet dataset against ResNet-101.

Method	Untargeted Attacks									
	@1K	@2K	@3K	@4K	@5K	@6K	@7K	@8K	@9K	@10K
SQBA$_{\text{ResNet50}}$ (Park et al., 2024)	8.873	7.229	6.172	5.449	4.934	4.531	4.215	3.957	3.745	3.563
SQBA$_{\theta_0^{\text{PGD}}+\text{ResNet50}}$ (Park et al., 2024)	6.882	5.675	4.894	4.364	3.985	3.689	3.456	3.264	3.101	2.961
BBA$_{\text{ResNet50}}$ (Brunner et al., 2019)	14.935	11.764	10.346	9.484	8.870	8.421	8.051	7.754	7.511	7.295
BBA$_{\theta_0^{\text{PGD}}+\text{ResNet50}}$ (Brunner et al., 2019)	6.281	5.488	5.051	4.779	4.577	4.425	4.302	4.196	4.109	4.029
Prior-Sign-OPT$_{\text{ResNet50}}$	34.150	18.733	11.452	7.977	6.111	4.982	4.247	3.718	3.323	3.019
Prior-Sign-OPT$_{\theta_0^{\text{PGD}}+\text{ResNet50}}$	5.423	4.303	3.632	3.182	2.859	2.615	2.414	**2.267**	**2.142**	**2.045**
Prior-OPT$_{\text{ResNet50}}$	18.355	7.100	4.190	3.214	2.840	2.612	2.450	2.324	2.233	2.158
Prior-OPT$_{\theta_0^{\text{PGD}}+\text{ResNet50}}$	**4.932**	**3.807**	**3.273**	**2.940**	**2.710**	**2.532**	**2.390**	2.275	2.181	2.107

Table 21: Mean ℓ_2 distortions of untargeted attacks on the ImageNet dataset against SENet-154.

Method	Untargeted Attacks									
	@1K	@2K	@3K	@4K	@5K	@6K	@7K	@8K	@9K	@10K
SQBA$_{\text{ResNet50}}$ (Park et al., 2024)	16.332	11.802	9.335	7.788	6.765	6.016	5.445	4.994	4.630	4.332
SQBA$_{\theta_0^{\text{PGD}}+\text{ResNet50}}$ (Park et al., 2024)	13.342	9.871	7.944	6.707	5.863	5.246	4.779	4.410	4.115	3.860
BBA$_{\text{ResNet50}}$ (Brunner et al., 2019)	24.402	17.863	14.923	13.134	11.915	11.009	10.330	9.796	9.348	8.976
BBA$_{\theta_0^{\text{PGD}}+\text{ResNet50}}$ (Brunner et al., 2019)	13.074	10.435	9.080	8.221	7.626	7.187	6.843	6.559	6.320	6.112
Prior-Sign-OPT$_{\text{ResNet50}}$	45.340	26.404	17.200	12.317	9.412	7.551	6.285	5.400	4.740	4.223
Prior-Sign-OPT$_{\theta_0^{\text{PGD}}+\text{ResNet50}}$	12.375	8.859	6.900	5.684	4.865	**4.272**	**3.817**	**3.461**	**3.184**	**2.958**
Prior-OPT$_{\text{ResNet50}}$	29.578	14.233	8.955	6.677	5.542	4.823	4.316	3.947	3.630	3.394
Prior-OPT$_{\theta_0^{\text{PGD}}+\text{ResNet50}}$	**11.952**	**8.431**	**6.580**	**5.542**	**4.863**	4.368	3.980	3.680	3.420	3.215

Table 22: Success rates of untargeted attacks on ImageNet against Inception-v4.

Method	Untargeted Attacks									
	@1K	@2K	@3K	@4K	@5K	@6K	@7K	@8K	@9K	@10K
SQBA$_{\text{IncResV2}}$ (Park et al., 2024)	41.9%	55.8%	65.9%	74.7%	79.2%	85.6%	87.7%	89.9%	91.4%	93.0%
SQBA$_{\theta_0^{\text{PGD}}+\text{IncResV2}}$ (Park et al., 2024)	51.5%	63.7%	71.3%	79.4%	82.8%	87.4%	90.2%	91.2%	92.6%	93.3%
BBA$_{\text{IncResV2}}$ (Brunner et al., 2019)	16.3%	29.0%	39.0%	46.9%	54.3%	57.5%	60.6%	63.9%	66.6%	68.8%
BBA$_{\theta_0^{\text{PGD}}+\text{IncResV2}}$ (Brunner et al., 2019)	43.9%	53.4%	60.1%	65.6%	69.0%	71.7%	74.8%	77.0%	78.8%	79.6%
Prior-Sign-OPT$_{\text{IncResV2}}$	3.8%	16.6%	38.9%	60.4%	75.7%	85.0%	89.4%	91.8%	94.2%	96.3%
Prior-Sign-OPT$_{\theta_0^{\text{PGD}}+\text{IncResV2}}$	62.6%	72.2%	77.8%	84.4%	88.3%	90.7%	93.4%	94.5%	95.8%	96.9%
Prior-OPT$_{\text{IncResV2}}$	17.8%	63.4%	**86.6%**	**94.2%**	**96.4%**	**97.4%**	**98.4%**	**98.8%**	**99.0%**	**99.1%**
Prior-OPT$_{\theta_0^{\text{PGD}}+\text{IncResV2}}$	**64.7%**	**76.6%**	84.1%	89.2%	92.5%	95.1%	96.1%	96.7%	97.6%	98.1%

Table 23: Success rates of untargeted attacks on ImageNet against ViT.

Method	Untargeted Attacks									
	@1K	@2K	@3K	@4K	@5K	@6K	@7K	@8K	@9K	@10K
SQBA$_{\text{ConViT}}$ (Park et al., 2024)	55.9%	71.7%	81.1%	88.4%	91.9%	94.4%	96.7%	97.4%	97.8%	98.3%
SQBA$_{\theta_0^{\text{PGD}}+\text{ConViT}}$ (Park et al., 2024)	67.1%	80.7%	87.8%	91.6%	94.6%	96.2%	96.9%	97.6%	98.2%	98.3%
BBA$_{\text{ConViT}}$ (Brunner et al., 2019)	19.0%	39.6%	53.0%	61.6%	66.2%	70.2%	73.9%	75.2%	77.7%	79.3%
BBA$_{\theta_0^{\text{PGD}}+\text{ConViT}}$ (Brunner et al., 2019)	69.9%	76.4%	80.3%	84.8%	86.5%	87.5%	89.1%	89.5%	90.6%	91.3%
Prior-Sign-OPT$_{\text{ConViT}}$	8.4%	23.8%	49.2%	71.4%	83.6%	90.4%	94.0%	96.0%	97.1%	98.1%
Prior-Sign-OPT$_{\theta_0^{\text{PGD}}+\text{ConViT}}$	**83.8%**	**89.7%**	**93.6%**	**95.2%**	**96.4%**	**97.5%**	**97.9%**	**98.3%**	98.7%	**99.2%**
Prior-OPT$_{\text{ConViT}}$	26.2%	65.7%	83.6%	91.3%	94.7%	96.2%	97.1%	97.7%	**98.9%**	**99.2%**
Prior-OPT$_{\theta_0^{\text{PGD}}+\text{ConViT}}$	83.6%	**89.7%**	93.4%	94.9%	96.3%	97.3%	**97.9%**	98.1%	98.6%	98.9%

Table 24: Success rates of untargeted attacks on ImageNet against GC ViT.

Method	Untargeted Attacks									
	@1K	@2K	@3K	@4K	@5K	@6K	@7K	@8K	@9K	@10K
SQBA$_{\text{ConViT}}$ (Park et al., 2024)	38.1%	53.3%	64.4%	73.8%	79.6%	84.7%	87.7%	90.9%	93.1%	94.4%
SQBA$_{\theta_0^{\text{PGD}}+\text{ConViT}}$ (Park et al., 2024)	50.2%	65.5%	74.6%	81.9%	86.8%	89.7%	92.1%	94.1%	95.4%	96.2%
BBA$_{\text{ConViT}}$ (Brunner et al., 2019)	10.7%	28.2%	42.4%	50.4%	56.6%	62.9%	67.8%	71.5%	74.0%	77.6%
BBA$_{\theta_0^{\text{PGD}}+\text{ConViT}}$ (Brunner et al., 2019)	51.7%	60.3%	66.0%	69.4%	74.2%	78.1%	79.7%	82.7%	85.1%	86.5%
Prior-Sign-OPT$_{\text{ConViT}}$	1.7%	9.2%	27.5%	48.2%	62.7%	72.0%	78.7%	82.7%	86.3%	89.0%
Prior-Sign-OPT$_{\theta_0^{\text{PGD}}+\text{ConViT}}$	**63.4%**	73.6%	81.1%	85.4%	89.4%	91.2%	92.8%	94.3%	95.4%	96.4%
Prior-OPT$_{\text{ConViT}}$	10.0%	45.3%	68.1%	82.2%	87.9%	90.1%	92.4%	93.5%	94.8%	95.7%
Prior-OPT$_{\theta_0^{\text{PGD}}+\text{ConViT}}$	63.2%	**74.1%**	**81.4%**	**86.4%**	**89.9%**	**92.0%**	**93.5%**	**94.4%**	**95.7%**	**96.7%**

Table 25: Success rates of untargeted attacks on ImageNet against ResNet-101.

Method	Untargeted Attacks									
	@1K	@2K	@3K	@4K	@5K	@6K	@7K	@8K	@9K	@10K
SQBA$_{\text{ResNet50}}$ (Park et al., 2024)	78.7%	85.3%	89.6%	92.6%	94.6%	96.2%	97.0%	98.1%	98.3%	98.9%
SQBA$_{\theta_0^{\text{PGD}}+\text{ResNet50}}$ (Park et al., 2024)	88.5%	93.2%	95.2%	96.0%	97.1%	97.5%	98.1%	98.7%	98.9%	99.3%
BBA$_{\text{ResNet50}}$ (Brunner et al., 2019)	47.6%	62.3%	70.2%	75.2%	79.4%	81.1%	83.7%	84.6%	85.7%	86.9%
BBA$_{\theta_0^{\text{PGD}}+\text{ResNet50}}$ (Brunner et al., 2019)	89.8%	92.2%	93.9%	95.1%	95.9%	96.0%	96.4%	96.8%	97.1%	97.1%
Prior-Sign-OPT$_{\text{ResNet50}}$	10.9%	35.4%	65.0%	83.0%	91.1%	94.0%	95.9%	97.3%	98.6%	99.4%
Prior-Sign-OPT$_{\theta_0^{\text{PGD}}+\text{ResNet50}}$	94.5%	**96.1%**	**97.2%**	97.9%	98.2%	98.7%	99.0%	99.3%	99.4%	99.7%
Prior-OPT$_{\text{ResNet50}}$	42.0%	87.4%	96.2%	**98.3%**	**99.2%**	**99.3%**	**99.7%**	**99.7%**	**99.8%**	**100.0%**
Prior-OPT$_{\theta_0^{\text{PGD}}+\text{ResNet50}}$	**94.6%**	95.9%	96.9%	97.8%	98.3%	98.7%	98.7%	99.0%	99.2%	99.5%

Table 26: Success rates of untargeted attacks on ImageNet against SENet-154.

Method	Untargeted Attacks									
	@1K	@2K	@3K	@4K	@5K	@6K	@7K	@8K	@9K	@10K
SQBA$_{\text{ResNet50}}$ (Park et al., 2024)	45.1%	61.5%	72.9%	81.7%	85.7%	89.0%	91.7%	94.6%	96.4%	97.9%
SQBA$_{\theta_0^{\text{PGD}}+\text{ResNet50}}$ (Park et al., 2024)	59.1%	72.3%	81.1%	86.7%	90.2%	92.4%	94.4%	96.5%	97.5%	98.4%
BBA$_{\text{ResNet50}}$ (Brunner et al., 2019)	16.6%	33.9%	45.6%	54.9%	61.2%	66.3%	69.7%	72.7%	74.2%	76.9%
BBA$_{\theta_0^{\text{PGD}}+\text{ResNet50}}$ (Brunner et al., 2019)	60.8%	69.7%	75.4%	79.9%	83.2%	85.6%	87.0%	88.6%	89.9%	90.6%
Prior-Sign-OPT$_{\text{ResNet50}}$	3.7%	16.2%	36.6%	58.3%	75.2%	83.1%	88.3%	92.1%	95.0%	96.7%
Prior-Sign-OPT$_{\theta_0^{\text{PGD}}+\text{ResNet50}}$	71.9%	79.6%	87.2%	91.3%	94.2%	**96.3%**	**97.2%**	**97.6%**	97.9%	98.3%
Prior-OPT$_{\text{ResNet50}}$	16.3%	55.9%	77.5%	88.3%	93.0%	95.4%	97.0%	**97.6%**	**98.6%**	**98.9%**
Prior-OPT$_{\theta_0^{\text{PGD}}+\text{ResNet50}}$	**72.5%**	**81.3%**	**88.5%**	**91.6%**	**94.3%**	96.2%	97.1%	97.5%	98.0%	98.6%

on Inception-v4 and 12.26898528811572 for attacks on other networks, calculated as $\sqrt{0.001 \times d}$, where d is the input image's dimension . As shown in these tables, the PGD initialization improves the performance of both SQBA and BBA, resulting in reduced mean ℓ_2 distortions and higher attack success rates. Furthermore, our approach with PGD initialization outperforms both SQBA and BBA.

G.5 Comparison with State-Of-The-Art Methods

Table 27: Untargeted attack results of ViTs on the ImageNet dataset, where "Mean ℓ_2" denotes the average ℓ_2 norm distortion of the final adversarial examples, "AUC" denotes the area under the curve of mean ℓ_2 distortions versus the number of queries (lower is better), and "ASR" denotes the attack success rate of the final adversarial examples.

Method	ViT			GC ViT			Swin Transformer		
	Mean ℓ_2	AUC	ASR	Mean ℓ_2	AUC	ASR	Mean ℓ_2	AUC	ASR
HSJA (Chen et al., 2020)	5.637	102956.7	96.7%	7.955	163915.1	82.8%	10.635	228806.0	70.3%
TA (Ma et al., 2021b)	5.674	104023.3	96.6%	9.102	176063.8	76.7%	10.513	230351.0	68.4%
G-TA (Ma et al., 2021b)	5.643	102013.4	96.4%	8.671	170511.6	77.6%	9.929	219877.9	72.6%
GeoDA (Rahmati et al., 2020)	6.313	83176.7	91.0%	12.998	172173.2	54.3%	19.120	245094.6	31.5%
Evolutionary (Dong et al., 2019)	6.719	128659.9	89.8%	8.615	174592.0	79.1%	15.738	266695.9	52.6%
SurFree (Maho et al., 2021)	6.303	104053.9	91.6%	10.967	193400.6	65.4%	13.059	200688.5	58.3%
Triangle Attack (Wang et al., 2022)	10.097	99746.4	69.0%	30.119	298578.9	21.2%	29.005	288358.2	23.1%
$\text{BBA}_{\text{ResNet50}}$ (Brunner et al., 2019)	9.567	125221.1	74.0%	11.294	161711.4	67.5%	14.084	185551.7	59.9%
$\text{BBA}_{\text{ConViT}}$ (Brunner et al., 2019)	8.595	105826.6	79.3%	9.188	128468.5	77.6%	12.375	156081.9	59.5%
$\text{SQBA}_{\text{ResNet50}}$ (Park et al., 2024)	5.201	79423.0	95.7%	6.186	100435.8	89.2%	7.557	115845.7	83.2%
$\text{SQBA}_{\text{ConViT}}$ (Park et al., 2024)	4.452	**60295.8**	98.3%	5.056	79670.8	94.4%	5.883	82141.3	91.0%
Sign-OPT (Cheng et al., 2020)	4.572	111439.9	98.3%	7.185	166001.9	85.9%	9.899	238907.0	74.7%
SVM-OPT (Cheng et al., 2020)	5.070	120008.9	97.1%	7.325	171869.8	83.9%	10.526	249491.3	72.1%
Prior-Sign-$\text{OPT}_{\text{ResNet50}}$	4.850	119961.6	97.4%	6.723	165586.5	87.1%	9.254	234462.4	75.7%
Prior-Sign-$\text{OPT}_{\text{ConViT}}$	4.313	105379.9	98.1%	5.972	151725.9	89.0%	7.622	198431.3	84.2%
Prior-Sign-$\text{OPT}_{\text{ResNet50\&ConViT}}$	3.967	99940.6	98.6%	5.286	137011.9	92.9%	6.331	177589.1	89.2%
Prior-Sign-$\text{OPT}_{\theta_0^{\text{PGD}}+\text{ResNet50}}$	4.331	88120.1	97.7%	5.243	98749.0	92.6%	8.112	128167.1	80.3%
Prior-$\text{OPT}_{\text{ResNet50}}$	5.195	106791.0	97.3%	6.066	134255.9	90.7%	9.625	190534.1	73.0%
Prior-$\text{OPT}_{\text{ConViT}}$	3.754	62928.1	**99.2%**	4.453	92662.3	95.7%	5.558	102428.7	91.8%
Prior-$\text{OPT}_{\text{ResNet50\&ConViT}}$	**3.609**	60449.0	**99.2%**	**3.700**	**76896.1**	**98.3%**	**4.896**	**91211.7**	**94.5%**
Prior-$\text{OPT}_{\theta_0^{\text{PGD}}+\text{ResNet50}}$	5.009	90005.1	96.4%	5.502	98555.8	92.8%	8.552	128766.0	76.4%

Table 28: Untargeted attack results of CNNs on the ImageNet dataset, where "Mean ℓ_2" denotes the average ℓ_2 norm distortion of the final adversarial examples, "AUC" denotes the area under the curve of mean ℓ_2 distortions versus the number of queries (lower is better), and "ASR" denotes the attack success rate of the final adversarial examples.

Method	ResNet-101			ResNeXt-101 (64 × 4d)			SENet-154		
	Mean ℓ_2	AUC	ASR	Mean ℓ_2	AUC	ASR	Mean ℓ_2	AUC	ASR
HSJA (Chen et al., 2020)	5.158	96234.2	95.8%	5.484	110376.8	95.0%	9.385	177364.9	74.9%
TA (Ma et al., 2021b)	5.239	96858.5	95.9%	5.565	110870.1	95.0%	9.379	172600.0	73.8%
G-TA (Ma et al., 2021b)	5.225	95901.1	96.3%	5.524	109990.5	95.0%	5.430	119281.1	92.9%
GeoDA (Rahmati et al., 2020)	6.364	82320.0	91.9%	6.898	88947.7	89.3%	8.209	107267.4	80.9%
Evolutionary (Dong et al., 2019)	5.406	107841.6	93.2%	6.042	123706.5	91.3%	6.111	130032.0	90.1%
SurFree (Maho et al., 2021)	6.627	104285.4	88.1%	7.550	123394.0	83.7%	8.247	131295.4	79.5%
Triangle Attack (Wang et al., 2022)	12.123	117731.5	61.3%	11.883	116639.5	63.7%	15.019	145508.7	48.9%
$\text{BBA}_{\text{ResNet50}}$ (Brunner et al., 2019)	7.295	83314.7	86.9%	9.393	116579.5	74.9%	8.976	115007.9	76.9%
$\text{SQBA}_{\text{ResNet50}}$ (Park et al., 2024)	3.563	46450.8	98.9%	4.058	59316.7	97.8%	4.332	67106.3	97.9%
Sign-OPT (Cheng et al., 2020)	4.754	101907.7	95.9%	5.108	120545.5	95.4%	5.111	124730.7	93.5%
SVM-OPT (Cheng et al., 2020)	4.842	105778.8	95.8%	5.255	126799.4	95.0%	5.125	127568.9	93.7%
Prior-Sign-$\text{OPT}_{\text{ResNet50}}$	3.019	79126.4	99.4%	3.518	100999.4	98.9%	4.223	114089.3	96.7%
Prior-Sign-$\text{OPT}_{\theta_0^{\text{PGD}}+\text{ResNet50}}$	**2.045**	27148.4	99.7%	**2.450**	35290.7	99.4%	**2.958**	48708.7	98.3%
Prior-$\text{OPT}_{\text{ResNet50}}$	2.158	37218.3	**100.0%**	2.692	53085.7	**99.7%**	3.394	68609.1	**98.9%**
Prior-$\text{OPT}_{\theta_0^{\text{PGD}}+\text{ResNet50}}$	2.107	**25627.6**	99.5%	2.486	**33291.5**	**99.7%**	3.215	**48447.6**	98.6%

Tables 27, 28, and 29 show the experimental results of untargeted attacks against ViTs and CNNs on the ImageNet dataset, where "AUC" indicates area under the curve of the mean ℓ_2 distortions versus the number of queries, "Mean ℓ_2" denotes the average ℓ_2 norm distortion of the final adversarial examples, and "ASR" indicates the attack success rate of the final adversarial examples. Here, the final adversarial examples are generated by using the query budget of $10{,}000$. The ASR is defined as the the percentage of samples with distortions below a threshold ϵ, which is set to $\epsilon = \sqrt{0.001 \times d}$ in the ImageNet dataset and $\epsilon = 1.0$ in the CIFAR-10 dataset, where d is the image dimension. Tables 27, 28, and 29 show that the Prior-OPT with two surrogate models performs the best in most cases, and the PGD initialization of θ (e.g., Prior-$\text{OPT}_{\theta_0^{\text{PGD}}+\text{ResNet50}}$) can effectively decrease the AUC.

Table 29: Untargeted attack results of Inception networks on the ImageNet dataset, where "Mean ℓ_2" denotes the average ℓ_2 norm distortion of the final adversarial examples, "AUC" denotes the area under the curve of mean ℓ_2 distortions versus the number of queries (lower is better), and "ASR" denotes the attack success rate of the final adversarial examples.

Method	Inception-V3			Inception-V4		
	Mean ℓ_2	AUC	ASR	Mean ℓ_2	AUC	ASR
HSJA (Chen et al., 2020)	12.014	211938.7	81.1%	11.645	227700.5	82.1%
TA (Ma et al., 2021b)	12.378	208706.8	79.8%	11.694	219707.3	82.0%
G-TA (Ma et al., 2021b)	12.076	205670.7	81.5%	11.448	216797.7	83.3%
GeoDA (Rahmati et al., 2020)	9.437	124150.7	87.8%	9.688	128665.4	87.7%
Evolutionary (Dong et al., 2019)	9.809	192654.1	86.4%	10.839	215405.4	81.6%
SurFree (Maho et al., 2021)	11.648	186094.3	79.1%	13.818	221197.5	69.7%
Triangle Attack (Wang et al., 2022)	20.878	205534.2	46.5%	22.132	214723.3	42.5%
$\text{BBA}_{\text{IncResV2}}$ (Brunner et al., 2019)	13.952	169881.3	69.0%	14.191	182033.7	68.8%
$\text{BBA}_{\text{Xception}}$ (Brunner et al., 2019)	14.657	185798.3	67.2%	15.282	199287.2	63.6%
$\text{SQBA}_{\text{IncResV2}}$ (Park et al., 2024)	7.020	98767.0	94.3%	7.417	110451.8	93.0%
$\text{SQBA}_{\text{Xception}}$ (Park et al., 2024)	6.933	97022.6	94.7%	7.115	102939.0	92.2%
Sign-OPT (Cheng et al., 2020)	8.134	195118.7	91.9%	8.786	217576.3	89.8%
SVM-OPT (Cheng et al., 2020)	7.995	193289.7	92.3%	8.839	219673.6	89.0%
$\text{Prior-Sign-OPT}_{\text{IncResV2}}$	5.314	156261.6	97.8%	5.842	174243.9	96.3%
$\text{Prior-Sign-OPT}_{\text{Xception}}$	5.831	163715.5	96.8%	5.958	176950.5	95.7%
$\text{Prior-Sign-OPT}_{\text{IncResV2\&Xception}}$	4.225	130427.5	98.6%	4.199	142032.3	99.0%
$\text{Prior-Sign-OPT}_{\theta_0^{\text{PGD}}+\text{IncResV2}}$	4.713	75088.7	97.1%	4.863	83066.8	96.9%
$\text{Prior-OPT}_{\text{IncResV2}}$	4.067	79685.9	99.3%	4.027	85290.8	99.1%
$\text{Prior-OPT}_{\text{Xception}}$	4.539	88915.0	99.3%	4.261	90492.0	99.3%
$\text{Prior-OPT}_{\text{IncResV2\&Xception}}$	**3.387**	**64461.8**	**99.7%**	**3.167**	**66110.1**	**99.8%**
$\text{Prior-OPT}_{\theta_0^{\text{PGD}}+\text{IncResV2}}$	4.496	65031.0	98.4%	4.548	70165.3	98.1%

Table 30 shows the experimental results of ℓ_∞ norm attacks on the ImageNet dataset. The results show that Prior-OPT and Prior-Sign-OPT also perform well on ℓ_∞ norm attacks, which outperform Sign-OPT in terms of average ℓ_∞ norm distortions. These results highlight the effectiveness of our approach across various adversarial attack types.

Fig. 7 shows the experimental results of ℓ_2 norm untargeted attacks on the ImageNet dataset. The results demonstrate that Prior-OPT significantly outperform all compared methods, including SQBA and BBA that also use surrogate models. The results also show that use of multiple surrogate models can further boost the performance. In addition, the PGD initialization ensures the algorithm's initial attack direction θ_0 is already good, which enables it to achieve a better untargeted attack performance even with a small number of queries (e.g., the query budget of 1,000). Fig. 8 shows the experimental results of ℓ_2 norm targeted attacks on the ImageNet dataset. The results of Fig. 8 show that Prior-Sign-OPT outperforms Prior-OPT under targeted attacks on CNNs models, and Prior-Sign-OPT with multiple surrogate models outperforms that with a single surrogate model.

Figs. 9 and 10 show the attack success rates of untargeted and targeted attacks on the ImageNet dataset. In untargeted ℓ_2 norm attacks (Fig. 9), Prior-OPT with two surrogate models achieves the highest success rate, and both Prior-OPT and Prior-Sign-OPT outperform the baseline Sign-OPT. For targeted attacks (Fig. 10), Prior-Sign-OPT exhibits superior performance compared to Prior-OPT. One plausible explanation is that Prior-Sign-OPT employs a more query-efficient strategy by leveraging the sign of directional derivatives, which requires only a single query per direction. When α_i is small, Prior-OPT, which relies on binary search to fully exploit prior information, becomes less efficient due to its high query cost. Consequently, Prior-Sign-OPT holds a relative advantage in such scenarios.

Figs. 11 and 12 present the experimental results on the CIFAR-10 dataset. The results demonstrate that SQBA and Prior-Sign-OPT achieve the highest performance among all evaluated methods. In future work, we aim to further improve the performance of our approach on the CIFAR-10 dataset.

Figs. 13a, 13b, and 13c present the ablation studies of $\mathbb{E}[\gamma^2]$ based on our theoretical results, with Eq. (10) for Sign-OPT, Eq. (12) for Prior-Sign-OPT, and Eq. (17) for Prior-OPT. Fig. 13d demonstrates the performance of Prior-Sign-OPT in ℓ_2 norm untargeted attacks against the Swin Transformer on the ImageNet dataset, evaluated with different values of q.

Table 30: Mean ℓ_∞ distortions of untargeted attacks across various query budgets on ImageNet.

Target Model	Method	Mean ℓ_∞ distortions				
		@1K	@2K	@5K	@8K	@10K
Inception-v3	TA (Ma et al., 2021b)	**0.397**	0.379	0.359	0.348	0.342
	Sign-OPT (Cheng et al., 2020)	0.726	0.403	0.156	0.100	0.084
	SVM-OPT (Cheng et al., 2020)	0.723	0.389	0.155	0.102	0.088
	Prior-Sign-OPT$_{\text{IncResV2}}$	0.678	0.365	0.117	0.086	**0.080**
	Prior-Sign-OPT$_{\text{IncResV2\&Xception}}$	0.640	0.318	**0.102**	**0.083**	**0.080**
	Prior-OPT$_{\text{IncResV2}}$	0.581	0.267	0.138	0.115	0.109
	Prior-OPT$_{\text{IncResV2\&Xception}}$	0.502	**0.208**	0.119	0.111	0.109
Inception-v4	TA (Ma et al., 2021b)	**0.420**	0.402	0.381	0.370	0.365
	Sign-OPT (Cheng et al., 2020)	0.794	0.450	0.175	0.111	0.093
	SVM-OPT (Cheng et al., 2020)	0.811	0.446	0.178	0.113	0.096
	Prior-Sign-OPT$_{\text{IncResV2}}$	0.756	0.408	0.136	0.097	0.089
	Prior-Sign-OPT$_{\text{IncResV2\&Xception}}$	0.700	0.348	**0.107**	**0.086**	**0.082**
	Prior-OPT$_{\text{IncResV2}}$	0.645	0.302	0.157	0.131	0.123
	Prior-OPT$_{\text{IncResV2\&Xception}}$	0.558	**0.218**	0.117	0.108	0.106
ResNet-101	TA (Ma et al., 2021b)	0.301	0.285	0.267	0.258	0.253
	Sign-OPT (Cheng et al., 2020)	0.437	0.247	0.101	0.066	0.057
	SVM-OPT (Cheng et al., 2020)	0.461	0.254	0.110	0.075	0.066
	Prior-Sign-OPT$_{\text{ResNet50}}$	0.404	0.218	**0.074**	**0.053**	**0.049**
	Prior-OPT$_{\text{ResNet50}}$	**0.289**	**0.138**	0.075	0.064	0.060
ResNeXt-101 (64×4d)	TA (Ma et al., 2021b)	**0.362**	0.344	0.323	0.313	0.307
	Sign-OPT (Cheng et al., 2020)	0.611	0.326	0.131	0.090	0.078
	SVM-OPT (Cheng et al., 2020)	0.667	0.336	0.131	0.089	0.078
	Prior-Sign-OPT$_{\text{ResNet50}}$	0.574	0.303	0.104	**0.075**	**0.069**
	Prior-OPT$_{\text{ResNet50}}$	0.428	**0.196**	**0.097**	0.080	0.075
SENet-154	TA (Ma et al., 2021b)	**0.355**	0.336	0.316	0.306	0.300
	Sign-OPT (Cheng et al., 2020)	0.563	0.326	0.132	0.082	0.067
	SVM-OPT (Cheng et al., 2020)	0.570	0.325	0.132	0.082	0.068
	Prior-Sign-OPT$_{\text{ResNet50}}$	0.536	0.314	**0.113**	**0.074**	**0.065**
	Prior-OPT$_{\text{ResNet50}}$	0.448	**0.246**	0.129	0.102	0.094
ViT	TA (Ma et al., 2021b)	**0.399**	0.379	0.358	0.348	0.342
	Sign-OPT (Cheng et al., 2020)	0.602	0.302	0.105	0.072	**0.064**
	SVM-OPT (Cheng et al., 2020)	0.651	0.310	0.107	0.075	0.068
	Prior-Sign-OPT$_{\text{ResNet50}}$	0.597	0.334	0.118	0.084	0.077
	Prior-Sign-OPT$_{\text{ResNet50\&ConViT}}$	0.539	0.273	**0.090**	**0.069**	0.065
	Prior-OPT$_{\text{ResNet50}}$	0.591	0.352	0.178	0.136	0.123
	Prior-OPT$_{\text{ResNet50\&ConViT}}$	0.429	**0.217**	0.124	0.110	0.106
GC ViT	TA (Ma et al., 2021b)	**0.380**	0.365	0.348	0.339	0.335
	Sign-OPT (Cheng et al., 2020)	0.680	0.434	0.186	0.119	0.098
	SVM-OPT (Cheng et al., 2020)	0.678	0.427	0.183	0.116	0.097
	Prior-Sign-OPT$_{\text{ResNet50}}$	0.670	0.445	0.183	0.116	0.097
	Prior-Sign-OPT$_{\text{ResNet50\&ConViT}}$	0.642	0.389	**0.141**	**0.092**	**0.079**
	Prior-OPT$_{\text{ResNet50}}$	0.652	0.455	0.248	0.185	0.163
	Prior-OPT$_{\text{ResNet50\&ConViT}}$	0.538	**0.305**	0.160	0.131	0.122
Swin Transformer	TA (Ma et al., 2021b)	**0.536**	0.515	0.491	0.479	0.472
	Sign-OPT (Cheng et al., 2020)	1.009	0.625	0.258	0.159	0.128
	SVM-OPT (Cheng et al., 2020)	1.036	0.622	0.251	0.157	0.131
	Prior-Sign-OPT$_{\text{ResNet50}}$	1.000	0.647	0.262	0.162	0.133
	Prior-Sign-OPT$_{\text{ResNet50\&ConViT}}$	0.909	0.513	0.169	**0.105**	**0.088**
	Prior-OPT$_{\text{ResNet50}}$	0.942	0.619	0.309	0.226	0.198
	Prior-OPT$_{\text{ResNet50\&ConViT}}$	0.662	**0.321**	**0.159**	0.129	0.120

Figs. 14, 16, and 18 show examples of adversarial images generated using different query numbers in targeted attacks with Sign-OPT, Prior-Sign-OPT, and Prior-OPT methods. Figs. 15, 17, and 19 show the corresponding adversarial perturbations for the Sign-OPT, Prior-Sign-OPT, and Prior-OPT methods. Initially, all methods start with an image from the target class and iteratively minimize the ℓ_2 norm distance (or ℓ_2 distortion) to the original image, while maintaining the predicted label as the target class. Prior-Sign-OPT and Prior-OPT achieve a faster reduction in perturbation magnitude compared to Sign-OPT, as shown in Figs. 15, 17, and 19.

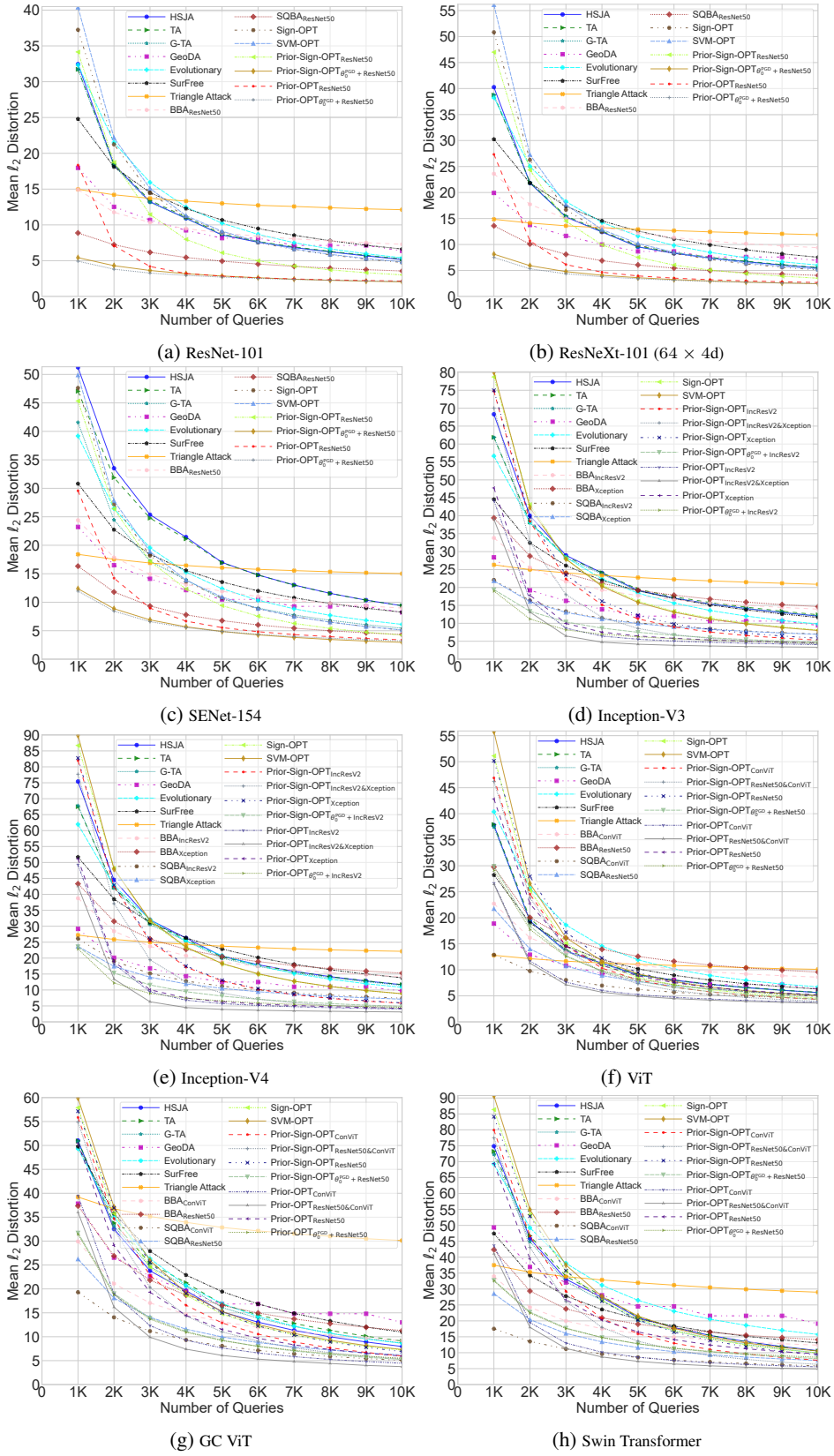

(a) ResNet-101

(b) ResNeXt-101 (64 × 4d)

(c) SENet-154

(d) Inception-V3

(e) Inception-V4

(f) ViT

(g) GC ViT

(h) Swin Transformer

Figure 7: Mean distortions of ℓ_2 norm untargeted attack under different query budgets on the ImageNet dataset.

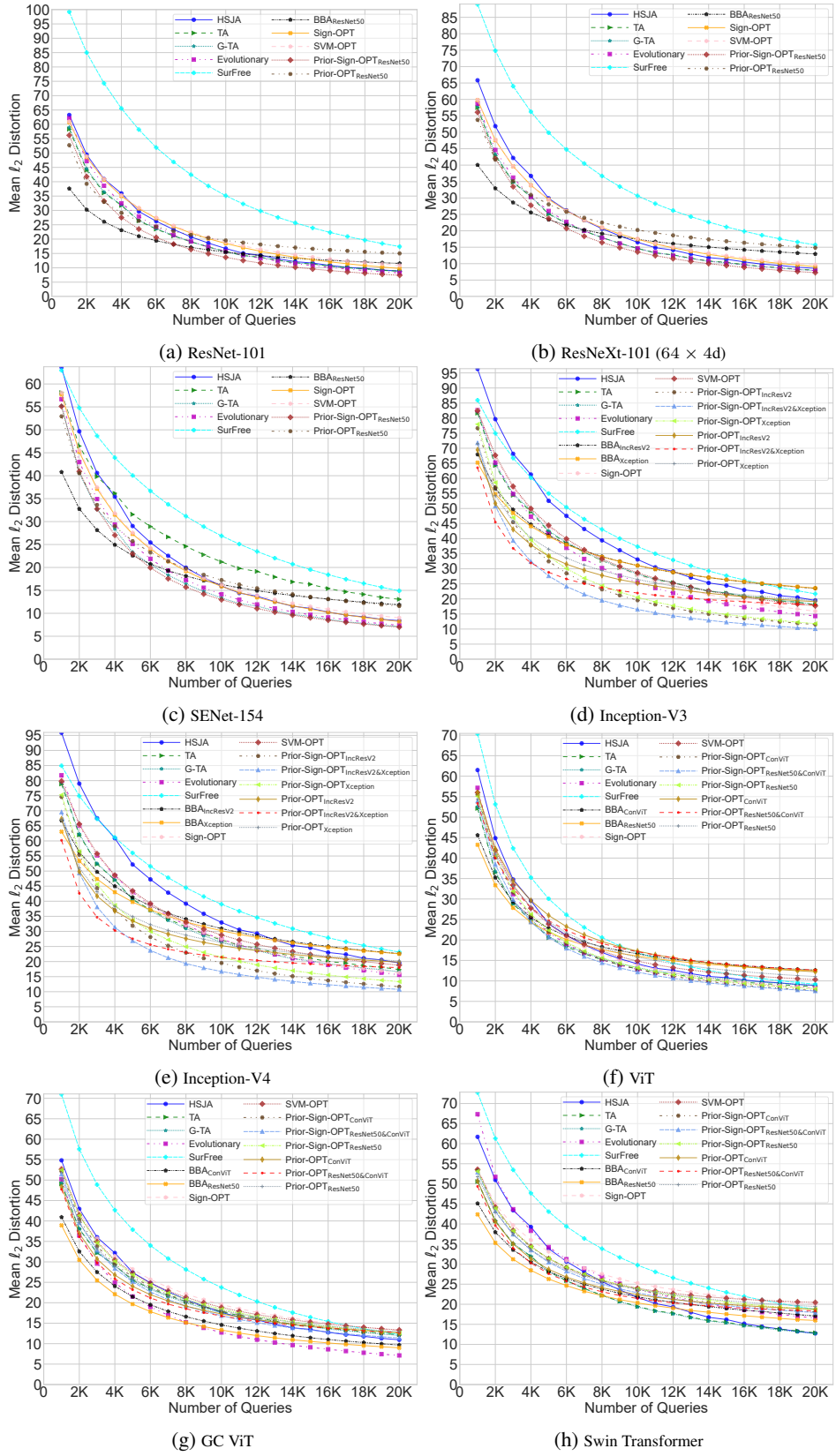

(a) ResNet-101 (b) ResNeXt-101 (64 × 4d) (c) SENet-154 (d) Inception-V3 (e) Inception-V4 (f) ViT (g) GC ViT (h) Swin Transformer

Figure 8: Mean distortions of ℓ_2 norm targeted attacks under different query budgets on the ImageNet dataset.

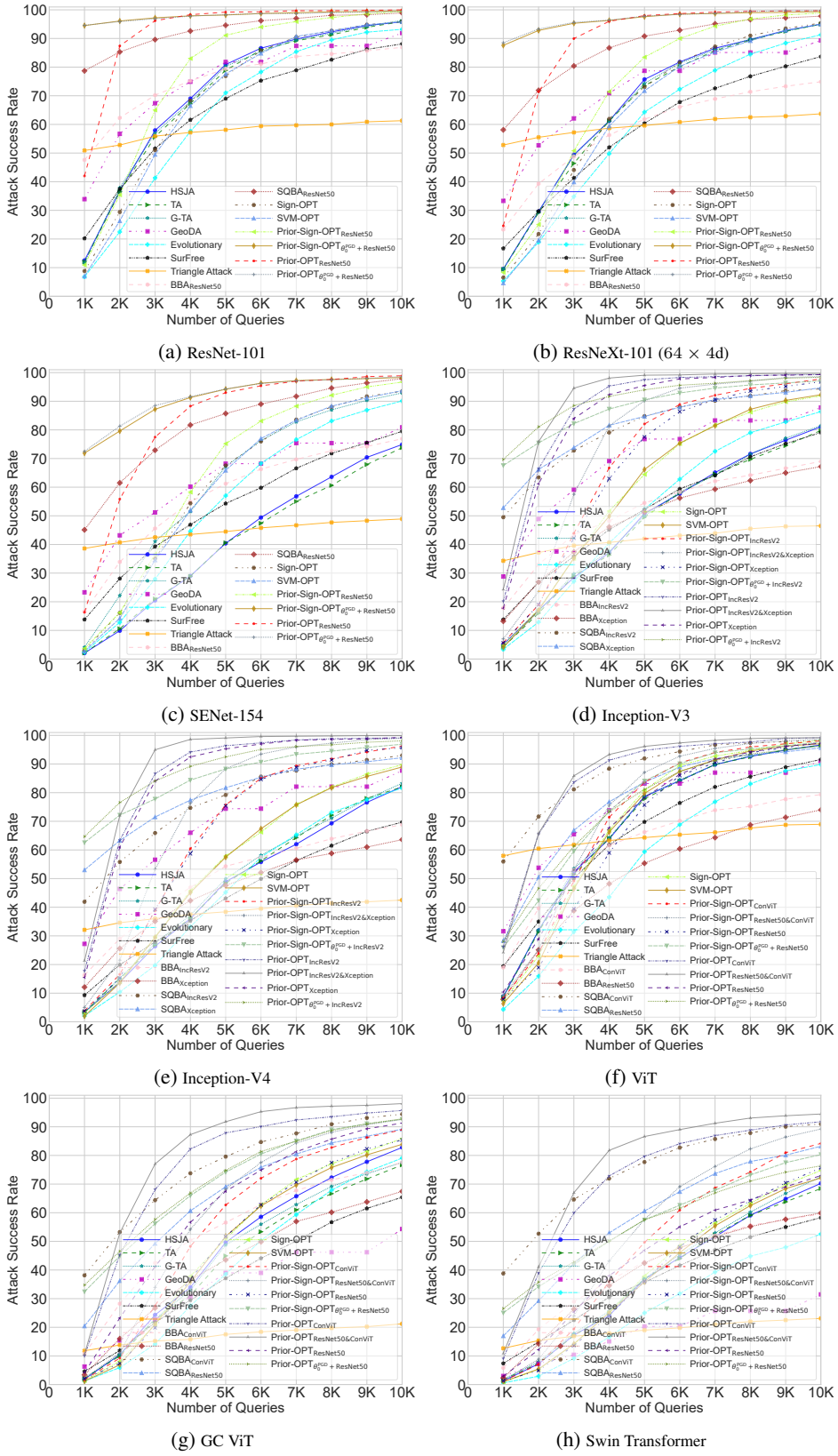

(a) ResNet-101 (b) ResNeXt-101 (64 × 4d)

(c) SENet-154 (d) Inception-V3

(e) Inception-V4 (f) ViT

(g) GC ViT (h) Swin Transformer

Figure 9: Attack success rates of ℓ_2 norm untargeted attacks under different query budgets on the ImageNet dataset.

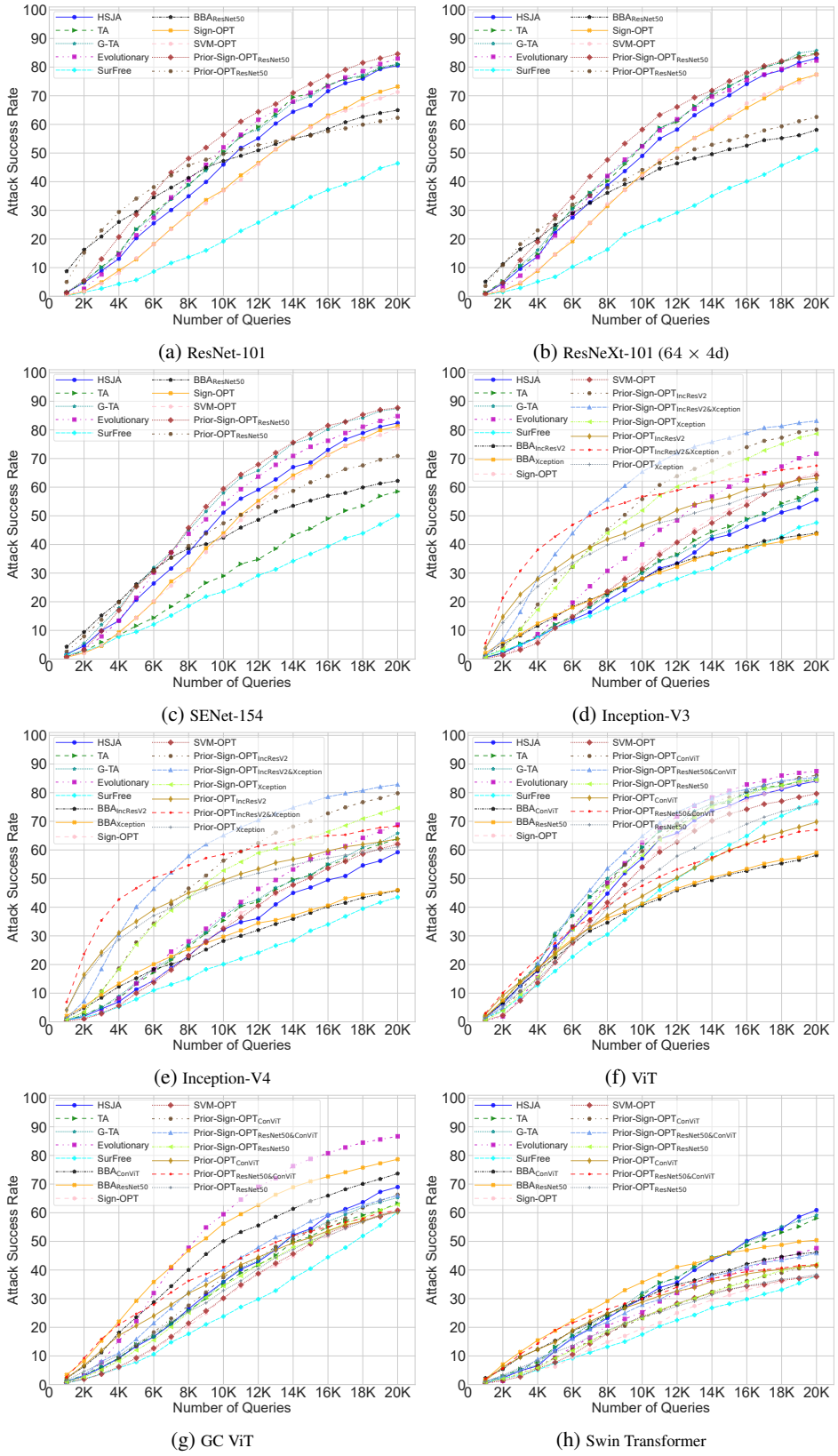

(a) ResNet-101 (b) ResNeXt-101 (64 × 4d)

(c) SENet-154 (d) Inception-V3

(e) Inception-V4 (f) ViT

(g) GC ViT (h) Swin Transformer

Figure 10: Attack success rates of ℓ_2 norm targeted attacks under different query budgets on the ImageNet dataset.

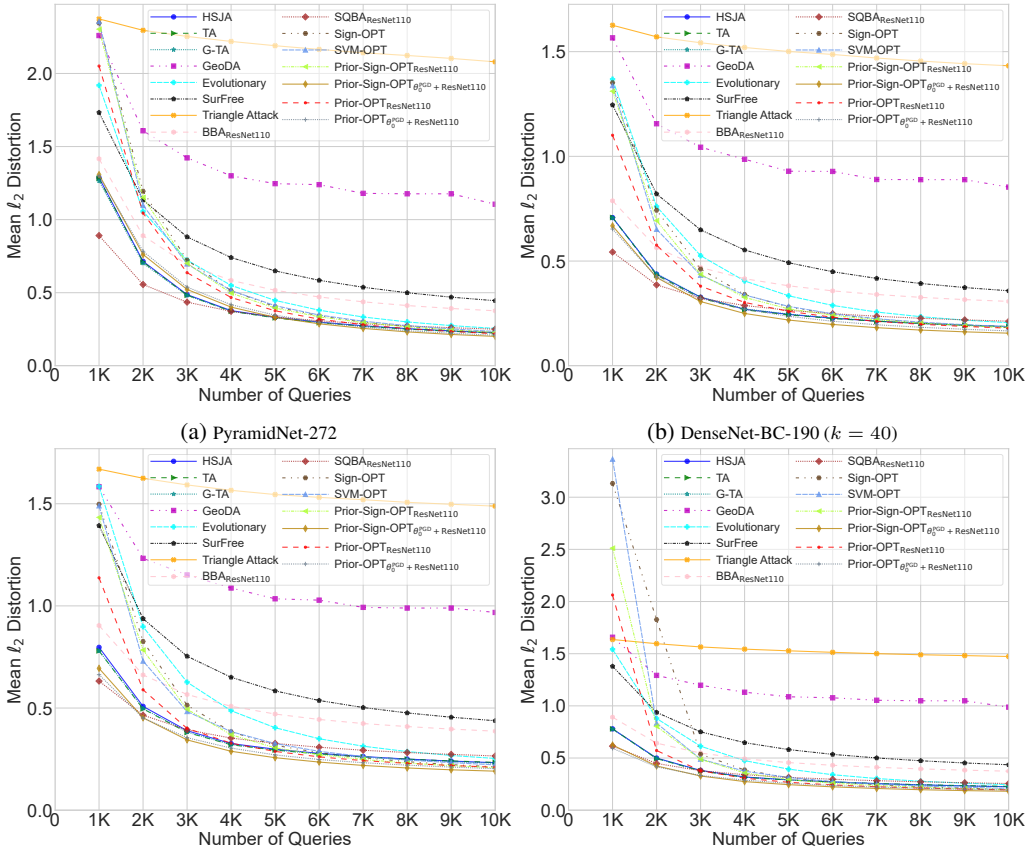

(a) PyramidNet-272

(b) DenseNet-BC-190 ($k = 40$)

(c) WRN-28

(d) WRN-40

Figure 11: Mean distortions of ℓ_2 norm untargeted attack under different query budgets on the CIFAR-10 dataset.

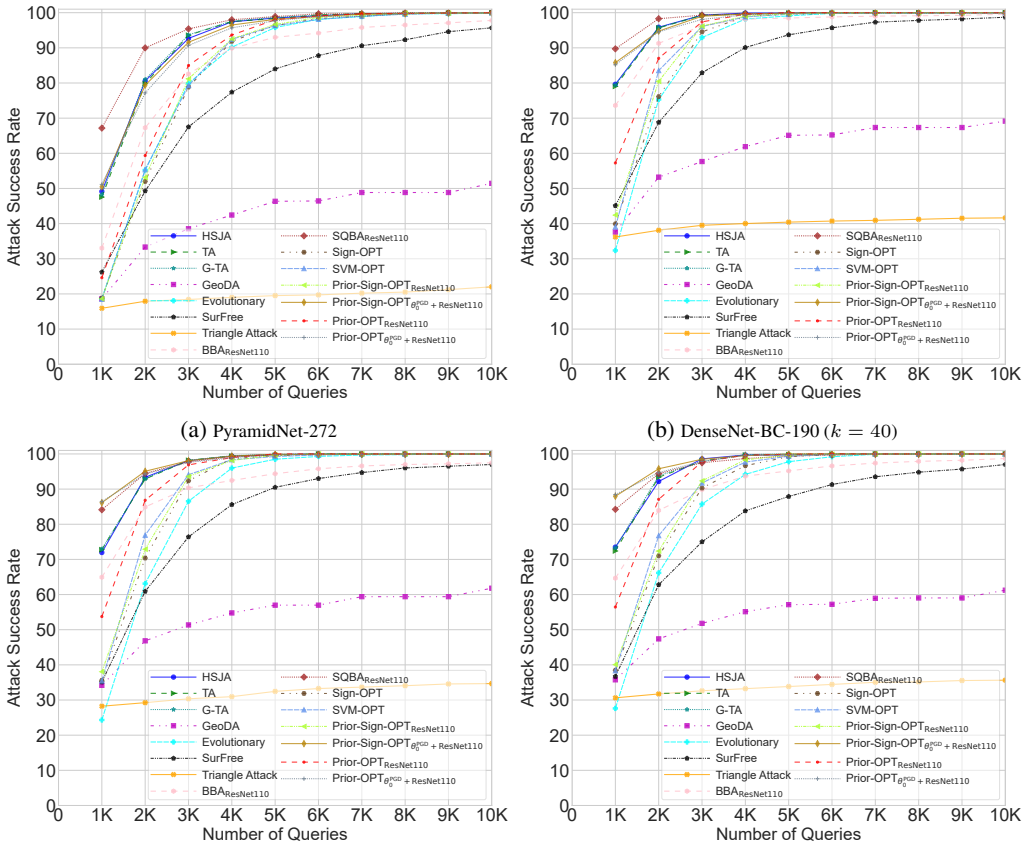

(a) PyramidNet-272 (b) DenseNet-BC-190 ($k = 40$)

(c) WRN-28 (d) WRN-40

Figure 12: Attack success rates of ℓ_2 norm untargeted attacks under different query budgets on the CIFAR-10 dataset.

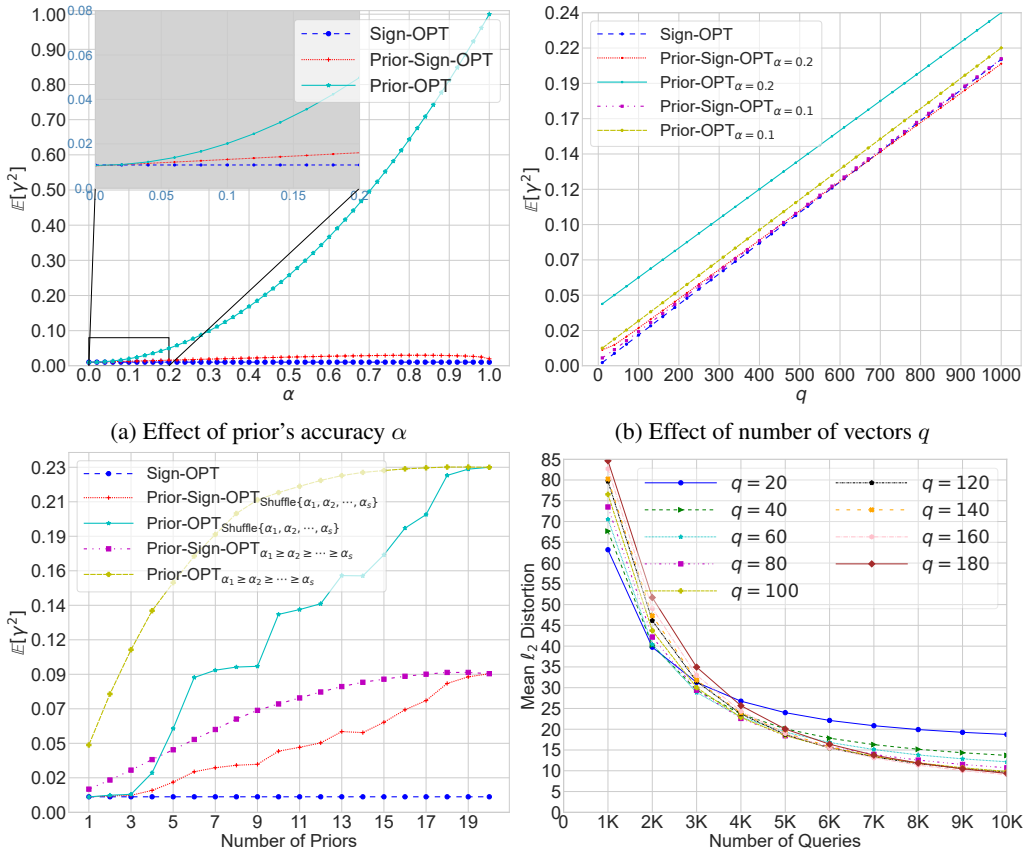

(a) Effect of prior's accuracy α

(b) Effect of number of vectors q

(c) Effect of number of priors

(d) Prior-Sign-OPT with different q

Figure 13: Experimental results of ablation studies of $\mathbb{E}[\gamma^2]$. Figs. 13a, 13b, and 13c are based on theoretical results (Eqs. (10), (12) and (17)) with $d = 3072$. Fig. 13d demonstrates the results of attacking against Swin Transformer on the ImageNet dataset using Prior-Sign-OPT with different q.

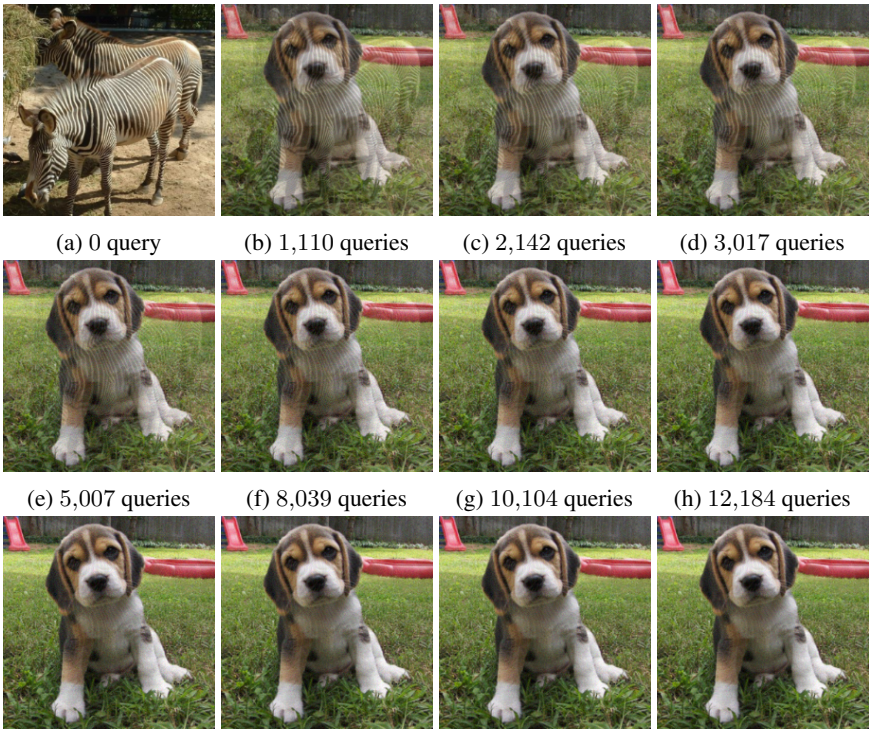

(a) 0 query (b) 1,110 queries (c) 2,142 queries (d) 3,017 queries

(e) 5,007 queries (f) 8,039 queries (g) 10,104 queries (h) 12,184 queries

(i) 15,176 queries (j) 18,477 queries (k) 19,032 queries (l) 20,470 queries

Figure 14: Adversarial images generated with different queries in Sign-OPT targeted attacks against ResNet-101.

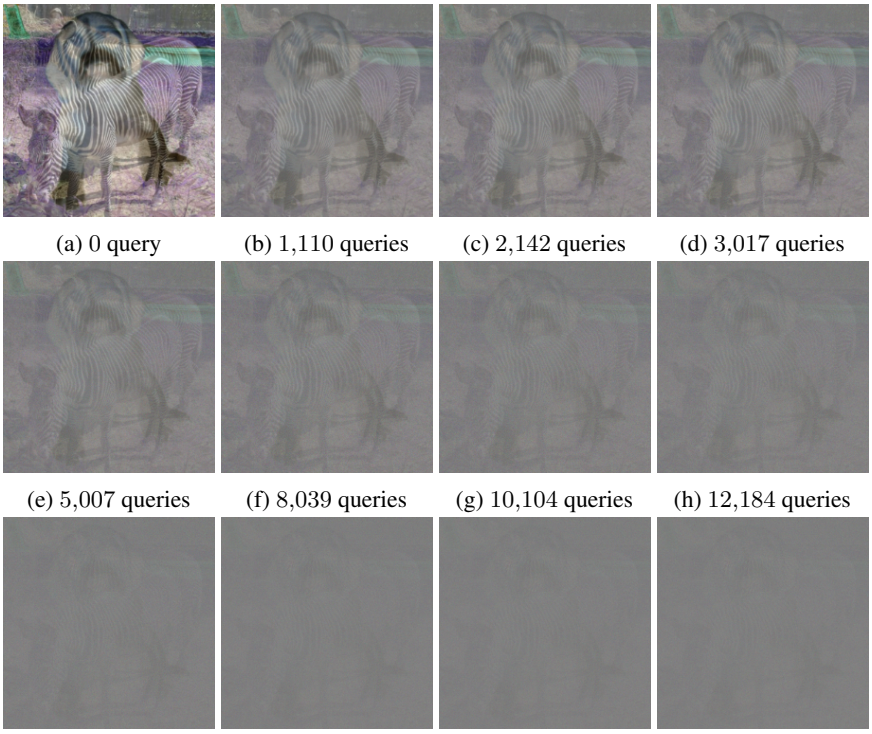

(a) 0 query (b) 1,110 queries (c) 2,142 queries (d) 3,017 queries

(e) 5,007 queries (f) 8,039 queries (g) 10,104 queries (h) 12,184 queries

(i) 15,176 queries (j) 18,477 queries (k) 19,032 queries (l) 20,470 queries

Figure 15: The corresponding adversarial perturbations generated with different queries in Sign-OPT targeted attacks against ResNet-101.

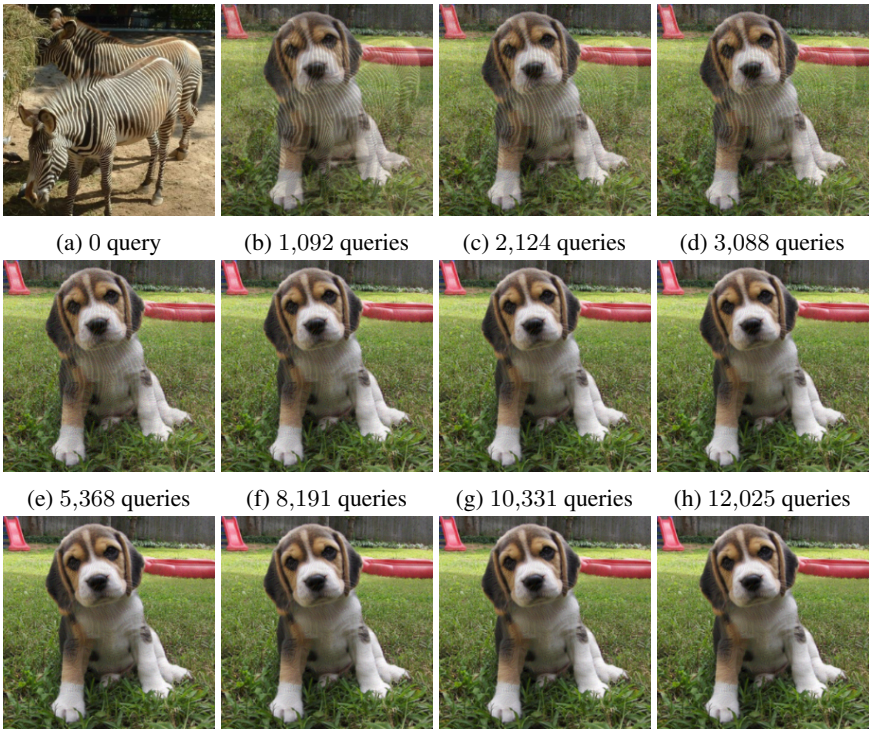

(a) 0 query (b) 1,092 queries (c) 2,124 queries (d) 3,088 queries

(e) 5,368 queries (f) 8,191 queries (g) 10,331 queries (h) 12,025 queries

(i) 15,192 queries (j) 18,149 queries (k) 19,138 queries (l) 20,114 queries

Figure 16: Adversarial images generated with different queries in Prior-Sign-OPT targeted attacks against ResNet-101.

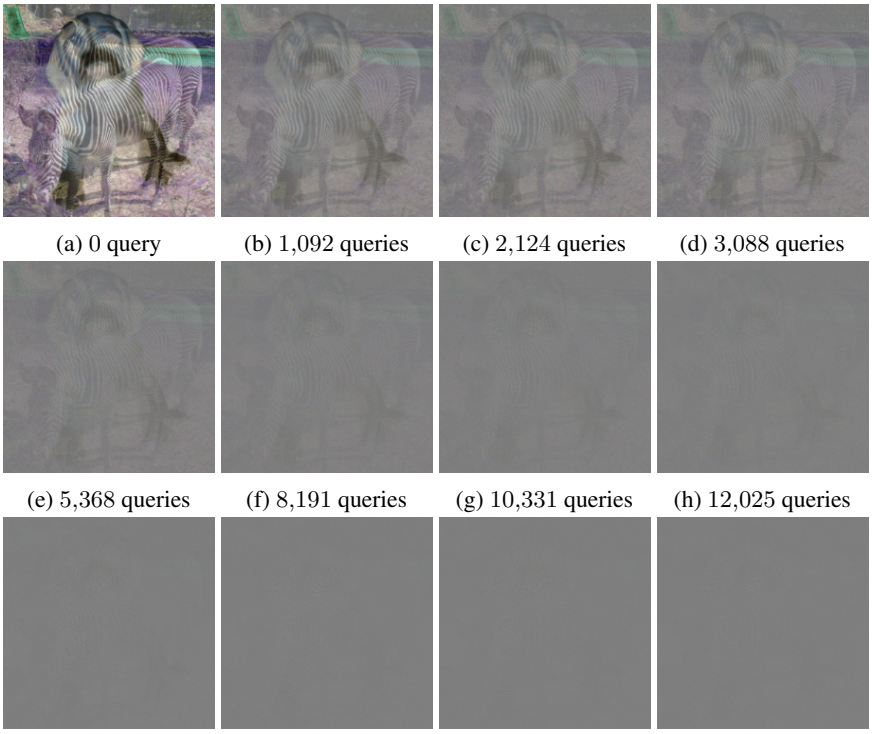

(a) 0 query (b) 1,092 queries (c) 2,124 queries (d) 3,088 queries

(e) 5,368 queries (f) 8,191 queries (g) 10,331 queries (h) 12,025 queries

(i) 15,192 queries (j) 18,149 queries (k) 19,138 queries (l) 20,114 queries

Figure 17: The corresponding adversarial perturbations generated with different queries in Prior-Sign-OPT targeted attacks against ResNet-101.

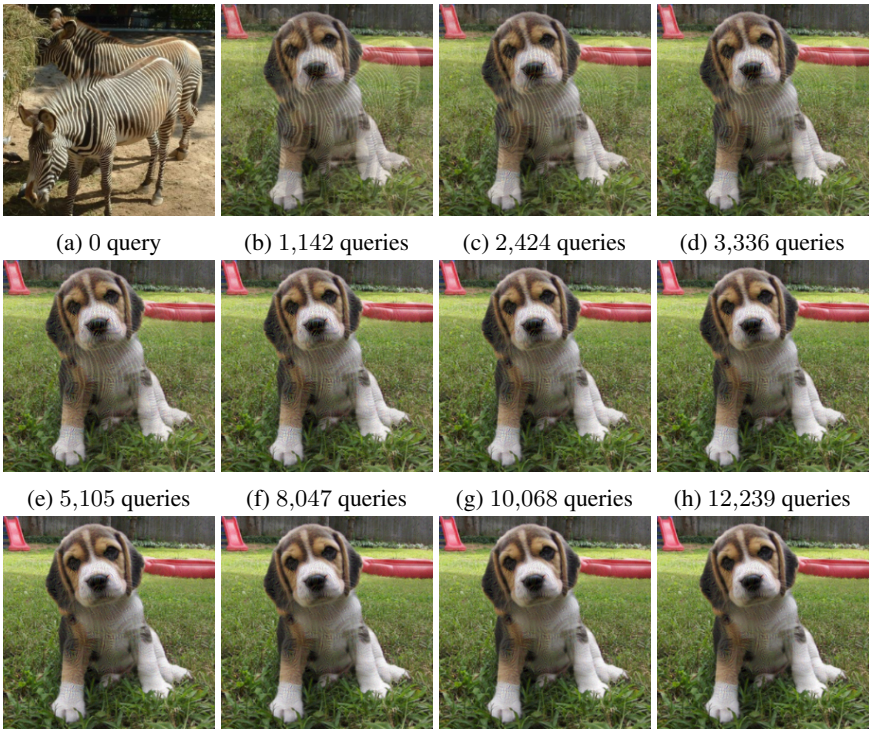

(a) 0 query (b) 1,142 queries (c) 2,424 queries (d) 3,336 queries

(e) 5,105 queries (f) 8,047 queries (g) 10,068 queries (h) 12,239 queries

(i) 15,646 queries (j) 18,179 queries (k) 19,189 queries (l) 20,233 queries

Figure 18: Adversarial images generated with different queries in Prior-OPT targeted attacks against ResNet-101.

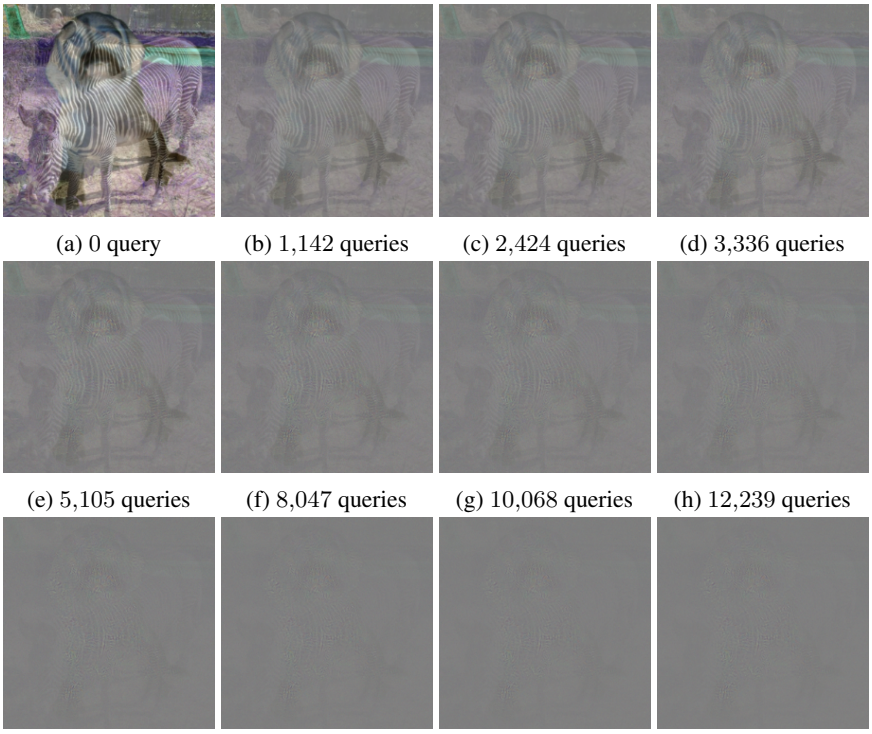

(a) 0 query (b) 1,142 queries (c) 2,424 queries (d) 3,336 queries

(e) 5,105 queries (f) 8,047 queries (g) 10,068 queries (h) 12,239 queries

(i) 15,646 queries (j) 18,179 queries (k) 19,189 queries (l) 20,233 queries

Figure 19: The corresponding adversarial perturbations generated with different queries in Prior-OPT targeted attacks against ResNet-101.